



REPUBLIC OF IRAQ
MINISTRY OF HIGHER EDUCATION AND SCIENTIFIC
RESEARCH
AL-FURAT AL-AWSAT TECHNICAL UNIVERSITY
ENGINEERING TECHNICAL COLLEGE-NAJAF

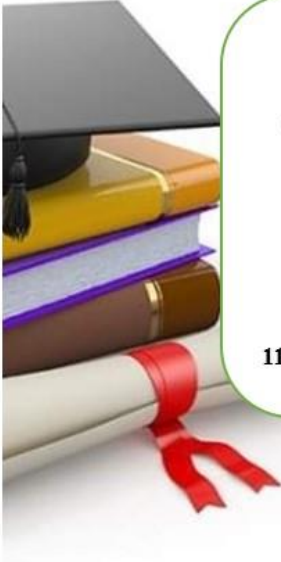
FLAME FRONT PROPAGATION IN A
HORIZONTAL TUBE WITH VARIABLE LENGTH

A Thesis
Submitted to the Department of Mechanical Engineering
Techniques of Power
In Partial Fulfillment of The Requirements for The Master in
Thermal Technologies Degree in Mechanical Engineering
Techniques of Power (M.Tech.)

BY:
HUSSEIN MOHSEN ABDUL HUSSEIN. AL-MAYALI
B.Sc. Automotive. Eng. 2007

SUPERVISED BY:
ASST. PROF. DR. ZAID MAAN HASAN AL-DULAIMI

2024



بِسْمِ اللَّهِ الرَّحْمَنِ الرَّحِيمِ

يَرْفَعُ اللَّهُ الَّذِينَ ءَامَنُوا مِنْكُمْ وَالَّذِينَ أُوتُوا
الْعِلْمَ دَرَجَاتٍ

سورة المجادلة الآية 11

ACKNOWLEDGMENTS

In the name of Allah, the first who deserves all thanks and gratitude for blessing all creatures and for providing the strength and willingness to establish this research,

I would like to express my sincere thanks to my supervisor (Asst. Prof. Dr. Zaid Maan Hasan Al-Dulaimi) for his advice, support, and ideas that were useful in completing this work.

I would like to express my sincere thanks to Dr. Mohammed A. Al-Fahham for his advice and ideas that were useful in this work

Also, my sincere thanks to Asst. Prof. Dr. Adel A. Eidan, Head of Mechanical Engineering Technical, Power Dept., and all the staff of the department for their help, as well as all my colleagues.

Friends and people who have provided assistance and information are too numerous to list. Here, I take the opportunity to express my sincere thanks, love, and great appreciation for their efforts, opinions, and observations. Here I wish to thank them, especially my close friends (Dr. Saif W. Mohammed Ali) from the Mechanical Engineering Department at the University of Kufa (Mohammed Abd Al-Khaliq), (Hamza Maksd) from Karbala University, and (Zahraa Hamzah Hasan) from the Aeronautical Department, for their large favor in this work.

Special thanks to my university, Al-Furat Al-Awsat Technical University Engineering Technical College of Najaf, for supporting me during my studies.

Finally, I would like to thank my family—my wife, my daughter, and my sons—for their unconditional tolerance and support. During the years of this study, many friends and loved ones played an important role in encouraging me to continue and complete the work, and I would like to express to all of them my sincere thanks and pride from the bottom of my heart.

DEDICATION

To the symbol of human justice "Imam Ali bin Abi Talib"

*To the cradle of science and civilization, "The Wounded
Iraq"*

To my beloved late mother and late father

To my life companion my beloved wife

To my beloved daughter and dear son Childhood years

accompanied my long studies

*And to my dear brother and sisters I am glad that you accept
my humble efforts*

HUSSEIN

2024

DECLARATION

I hereby declare that the work in this thesis is my own and has not been submitted to other organizations or for acquiring any other degree.

Signature:

Name: Hussein Mohsen Abdul Hussein. Al-Mayali

Date: / /2024

SUPERVISOR CERTIFICATION

We certify that this thesis entitled “**Flame Front Propagation in A Horizontal Tube with Variable Length**” which is being submitted by **Hussein Mohsen Abdul Hussein Al-Mayali** was prepared under our supervision at the Department of Mechanical Engineering Techniques of Power, College of Technical Engineering-Najaf, AL-Furat Al-Awsat Technical University, as partial fulfillment of the requirements for the degree of Master of Techniques in Thermal Engineering.

Signature:

Name: Zaid Maan Hasan Al-Dulaimi

Date: / /2024

In view of the available recommendation, we forward this thesis for debate by the examining committee.

Signature:

Name: Asst. Prof. Dr. Adel A. Eidan

Head of Mechanical Eng. Tech. of Power Dept.

Date: / /2024

COMMITTEE REPORT

We certify that we have read this thesis titled “**Flame Front Propagation in A Horizontal Tube with Variable Length**” which is being submitted by **Hussein Mohsen Abdul Hussein Al-Mayali** and as Examining Committee, examined the student in its contents. In our opinion, the thesis is adequate for the award of the degree of Master of Techniques in Thermal Engineering.

Signature:

Name:

Date:

Signature:

Name:

Date:

Signature:

Name:

Date:

Signature:

Name:

Date:

Signature:

Name:

Date:

Signature:

Name:

Date:

Approval of the Engineering Technical College-Najaf

Signature:

Name:

Dean of Engineering Technical

College-Najaf

Date: / /2024

LANGUAGE EXPERT CERTIFICATION

This is to certify that this thesis entitled “**Flame Front Propagation in A Horizontal Tube with Variable Length**” was reviewed linguistically. Its language was amended to meet the style of the English language.

Signature:

Name:

Date: / /2024

ABSTRACT

Premixed flame dynamics are particularly complex in confined geometries and play a crucial role in optimizing combustion applications and safety systems. The study has two main objectives. The first objective is to simulate the two-dimensional (2D) chemically reacting flow model implemented in the XiFoam solver, part of the OpenFOAM CFD toolbox with a length of 1.5 m and a diameter of 0.72 m. The second objective is to Same scenario examine the effects of tube length and equivalence ratio on the speed and shape of premixed LPG-air flames in horizontal tubes closed at one end of the ignition and open at the other end using high-speed photography. A notable finding is that the flame front, which forms when the equivalence ratio is between 0.8-1.4 and the tube length is 1.3 m, 1.5 m, and 2 m, undergoes significant distortions. The mixture composition affects the formation and dynamics of the tulip flame, which can collapse differently at low and high equivalence ratios. The shape of the flame, especially the tulip flame, is affected by the length of the tube and the equivalence ratio over time. For a length of 1.5 m and an equivalence ratio of 1, the tulip flame appears at 0.365 m and 0.0162 ms and collapses at 0.7 m and 0.0226 ms. For an equivalence ratio of 1.2, the tulip flame forms at 0.372 m and 0.0165 ms and fades at 0.709 m and 0.0233 ms. For an equivalence ratio of 0.8, the tulip flame changes at 0.315 m and 0.0200 ms and collapses at 0.665 m and 0.0286 ms. For a higher equivalence ratio of 1.4, the flame becomes spiral at 0.318 m and 0.0221 ms and collapses at 0.615 m and 0.0305 ms. Both the experiments and the 2D simulations show interactions and the deceleration in the flame front, reverse flow, and vortices in the burned gas altering the flame shape and making the

flame front develop a tulip shape. Results of these parameters show that with more fuel concentration, by increasing the equivalence ratio and going from a fuel-lean to a fuel-rich condition, the flame front goes faster with higher velocity and pressure.

TABLE OF CONTENTS

ACKNOWLEDGMENTS	I
DEDICATION	II
DECLARATION	III
SUPERVISOR CERTIFICATION	IV
COMMITTEE REPORT	V
LANGUAGE EXPERT CERTIFICATION	VI
ABSTRACT	VII
CHAPTER ONE: INTRODUCTION	1
1.1 Introduction	1
1.2 Flame Propagation in A Cylinder	1
1.3 Premixed flames Dynamics in Tubes.....	2
1.4 Burning Velocity and Flame Speed	5
1.5 Flame Speed Measurement Techniques.....	6
1.6 Flame propagation applications	6
1.7 Problem Statement	8
1.8 Objectives for the Present Work	8
1.9 Scope of Study	9
CHAPTER TWO: LITERATURE REVIEW	10
2.1 Introduction	10
2.2 Flame Propagation.....	10
2.3 Flame Propagation Stages	12
2.3.1 Spherical flame.....	20
2.3.2 Finger flame	21
2.3.3 Planar flame.....	22
2.3.4 Tulip flame	23
2.4 Factors Affecting Flame Propagation	26

2.4.1 Fuel-air mixture and equivalence ratio	28
2.4.2. Fuel type	30
2.4.3 Tube length.....	33
2.5 Summary	34
CHAPTER THREE: NUMERICAL STUDY	39
3.1 Introduction	39
3.2 Numerical Modeling and Methodology	39
3.2.1 OpenFOAM methodology	40
3.2.2 Cases assumptions.....	40
3.2.3 CFD models.....	41
3.3 Model Governing Equations	42
3.3.1 Mass conservation equation (continuity equation)	43
3.3.2 Momentum equation	43
3.3.3 Energy transport equation	44
3.3.4 Species transport equation.....	46
3.3.5 Turbulence modeling using the standard $k - \epsilon$ model.....	48
3.3.6 Combustion model	51
3.3.7 Radiation model	53
3.4 Methods for Predicting Required Values.....	55
3.4.1 Flame front propagation prediction.....	55
3.4.2 Prediction of species mole fractions	56
3.5 Mesh Generation and Mesh Convergence Study.....	56
3.6 Boundary Conditions and Initial conditions	58
CHAPTER FOUR: EXPERIMENTAL SETUP.....	62
4.1 Introduction	62
4.2 The Experimental Apparatus's General Description.....	62
4.3 Combustion Chamber Unit	64
4.3.1 The glass cylinder.....	64

4.3.2 The Teflon flange	64
4.3.3 Brass swing check valve	65
4.4 Ignition Circuit and Control Unit.....	65
4.5 Fuel Supply Control Unit.....	67
4.5.1 Gas injection unit	67
4.6 Mixture Preparing Unit	71
4.6.1 Mixing tank	71
4.6.2 LPG fuel cylinder	72
4.6.3 Pressure gauges	72
4.6.4 Reverse flame check valve.....	73
4.6.5 Solenoid valve	73
4.7 Flame Imaging Unit	74
4.7.1 The high-speed camera	74
4.7.2 Light source.....	75
4.8 Test Procedure.....	75
4.9 Image Processing.....	77
4.10 Flame Speed Calculation.....	78
4.11 Inaccuracy Sources.....	78
CHAPTER FIVE: RESULTS AND DISCUSSION.....	80
5.1 Introduction	80
5.2 Present Work Verification.....	81
5.2.1 Model validation	81
5.2.2 Contours and visualization validation.....	83
5.2.3 Behavior validations.....	87
5.3 Factors Effect on Flame Properties	90
5.3.1 The effect of equivalent ratio on flame front position and	90
velocity for 1.5 m length.....	90
5.3.2 The effect of equivalent ratio on flame front position and	94

velocity for L2 <i>m</i> length	94
5.3.3 The comparison of various lengths for different.....	97
equivalent ratio	97
5.4 Tulip Formation Behavior.....	103
5.4.1 Tulip flame formation of 1.5 <i>m</i> for various <i>Phi</i>	103
5.4.2 Tulip formation behavior of 2 <i>m</i> for various <i>Phi</i>	113
5.4.3 Tulip formation behavior of 1.3 <i>m</i> for various <i>Phi</i>	117
5.5 Tulip Formation Contours of Various Lengths for	120
Equivalence Ratio 1.4 (Extra Results)	120
5.6 Experimental Work Visualization.....	122
5.6.1 The effect of equivalent ratio on flame propagation.....	123
5.6.2 The dynamic visualization of flame propagation.....	126
5.6.3 Tulip formation of experimental visualization	127
CHAPTER SIX: CONCLUSIONS AND RECOMMENDATIONS	129
6.1 Conclusions	129
6.2 Recommendations	130
REFERENCES.....	132
APPENDICES	143
Appendix A	143
Appendix B.....	153
Appendix C	157
Publications.....	157

LIST OF FIGURES

Figure 1.1: Schematic showing possible propagation regimes of premixed flame in a tube	4
Figure 1.2: Laminar Premixed Flame and Combustion wave	5
Figure 2.1: Pressure at the closed end of a shock tube while stoichiometric propane-air flames are present	14
Figure 2.2: The four stages of flame propagation (a) hemispherical shape. (b) finger shape, (c) tulip flame. (d) flame surface inversion from	15
Figure 2.3: Geometry of aflame acceleration due to the initial condition form	16
Figure 2.4: Tulip flame initiation and proliferation reproduced with permission from	17
Figure 2.5: The formation of a deformed tulip flame (a) and a traditional tulip flame (b). the original flame shape is indicated by solid lines, while the succeeding flame shape is indicated by dashed lines. The characteristic flow velocity field is indicated by arrows. Reproduced with permission from	17
Figure 2.6: A progression of numerical schlieren pictures from a regular flame to a warped tulip flame, reproduction of	18
Figure 2.7: Plots of the streamlines in the channel at different times throughout the combustion process. (a) ignition stage; (b) finger flame stage; (c) planar flame stage; (d) propagating tulip flame stage. The nodes (N), saddles (S), half-nodes (N'), and half-saddles (S') are depicted in each illustration. At $X = 2$, the Euler characteristic is constant throughout the whole combustion process (Hariharan & Wichman, 2014)	21
Figure 2.8: Normalized plot displays the position and velocity of the flame front and stagnation point, as well as the pressure $p(t)$, pressure change rate (dp/dt), stagnation front speed, and flame front speed vs channel time t . Position and velocity of the flame are normalized to their greatest values ..	25

Figure 3.1: Combustor mesh generation	57
Figure 3.2: Temperature distributions along center line at different mesh sizes	58
Figure 3.3: The physical domain and its Boundary conditions: A) types of Boundary conditions, B) regions of the domain	59
Figure 4.1: Photograph of the experimental apparatus used in the study	63
Figure 4.2: Schematic sketch of the experimental rig.....	63
Figure 4.3: Photograph of the combustion chamber unit.....	64
Figure 4.4: The Teflon flange	65
Figure 4.5: Brass swing check valve.....	65
Figure 4.6: Schematic diagram of an electronic circuit for the ignition unit.....	66
Figure 4.7: The gas manifolds.....	68
Figure 4.8: Pressure regulator of the mixture	69
Figure 4.9: Air compressor.....	69
Figure 4.10: Electrical control board unit	71
Figure 4.11: Schematic diagram of mixing tank.....	72
Figure 4.12: Pressure Gauges, a) Total pressure gage, b) vacuum pressure gage.....	72
Figure 4.13: Schematic of reverse flame check valve	73
Figure 4.14: The solenoid valve.....	74
Figure 4.15: High-speed camera: Huawei-P 40 with 7860 FPS	75
Figure 5.1: Flame speed distribution along the pipe axis of various models and compared with experiential results	82
Figure 5.2: Flame pressure distribution along the pipe axis of various models and compared with experiential results	83
Figure 5.3: The validation between experimental work and numerical simulation of present and previous investigations	84
Figure 5.4: The validation between numerical present work and numerical	

simulation of Ashwin Hariharan	85
Figure 5.5: Flame shape and progress.....	86
Figure 5.6: Flame front distance from spark for different time comparison .	88
Figure 5.7: Flame front distance from spark of numerical and experimental work and compare with previous investigation	89
Figure 5.8: Flame tip distance with time for different equivalence ratio at L1.5 m	92
Figure 5.9: Flame tip velocity with time for different equivalence ratio at L1.5 m	94
Figure 5.10: Flame tip distance with time for different equivalence ratio at L2 m	96
Figure 5.11: Flame tip velocity with time for different equivalence ratio at L2 m.....	97
Figure 5.12: Flame tip distance with time at different length comparison for $\Phi = 1$	99
Figure 5.13: Flame tip distance with time at deferent length comparison for $\Phi = 1.2$	101
Figure 5.14: Flame tip distance with time at deferent length comparison for $\Phi = 0.8$	103
Figure 5.15: Correlation of flame tip distance and velocity over time in a 1.5 m CC with a stoichiometric mixture ($\Phi = 1$).....	106
Figure 5.16: Sequential visualization of flame propagation in a 1.5 m combustion chamber at stoichiometric conditions ($\Phi = 1$).....	106
Figure 5.17: Dynamics of flame tip velocity and distance in a 1.5 m combustion chamber with fuel-rich mixture ($\Phi = 1.2$).....	109
Figure 5.18: Temporal evolution of flame shapes in a 1.5 m combustion chamber at fuel-rich conditions ($\Phi = 1.2$)	109
Figure 5.19: Flame tip distance and velocity trends in a lean combustion	

environment ($\Phi = 0.8$) in a 1.5 m chamber	112
Figure 5.20: Chronological flame shape evolution at lean conditions ($\Phi = 0.8$) in a 1.5 m chamber	112
Figure 5.21: Flame tip distance and velocity fluctuations in a stoichiometric mixture in a 2 m chamber, $\phi = 1$	115
Figure 5.22: Visual chronology of flame front evolution in a stoichiometric mixture in a 2 m chamber, $\phi = 1$	115
Figure 5.23: Flame tip distance and velocity in a fuel-rich mixture in a 2 m chamber, $\phi = 1.2$	116
Figure 5.24: Flame shape progression in a fuel-rich mixture in a 2 m chamber, $\phi = 1.2$	116
Figure 5.25: Flame tip kinetics in a lean mixture in a 2 m chamber, $\phi = 0.8$	117
Figure 5.26: Temporal evolution of flame forms in a lean mixture in a 2 m chamber, $\phi = 0.8$	117
Figure 5.27: Flame front progression in a stoichiometric mixture ($\Phi = 1$) in a 1.3 m combustion chamber	119
Figure 5.28: Flame development in a fuel-rich mixture ($\Phi = 1.2$) in a 1.3 m chamber	119
Figure 5.29: Lean combustion flame behavior ($\Phi = 0.8$) in a 1.3 m chamber	120
Figure 5.30: Flame propagation in a highly fuel-rich environment ($\Phi = 1.4$) in a 1.5 m combustion chamber	121
Figure 5.31: Flame dynamics at excessively rich conditions ($\Phi = 1.4$) in a 2 m chamber	122
Figure 5.32: Combustion phenomena with excessive fuel ($\Phi = 1.4$) in a 1.3 m chamber	122
Figure 5.33: Comparative analysis of early flame propagation in a	

stoichiometric mixture ($\Phi = 1$)	125
Figure 5.34: Numerical and experimental visualization correlation for fuel-rich flame propagation ($\Phi = 1.2$)	125
Figure 5.35: Lean combustion flame dynamics ($\Phi = 0.8$) between simulations and experiments	125
Figure 5.36: High-speed camera images in the present study for flame propagation.....	127
Figure 5.37: Changes of absolute flame speed along the tube center-line versus flame front distance from spark	128

LIST OF TABLES

Table 1.1: The difference between burning velocity and flame speed	5
Table 1.2: Flame propagation applications	7
Table 2.1: Summary of the researches close to my work	35
Table 3.1: Meshing details	57
Table 3.2: Boundary conditions specifications for main properties under each category of the gov. Eq.	59
Table 3.3: Initial conditions	60

NOMENCLATURE

Symbols	Definition	Unit
A	Area	m^2
b	Regress Variable	
c	Progress Variable	
C_p	Specific heat at constant pressure	$kJ/kg \cdot ^\circ C$
d	CO_2 dilution ratio	%
h	Specific enthalpy	kJ/kg
k	Hydrogen blending ratio	%
n	Number of moles	Mole
P	Pressure	Pa
Pr	Prandtl number	
Q	Volume Flow rate	lpm
Re	Reynolds number	
Sc	Schmidt number	
T	Temperature	K or $^\circ C$
u	Velocity	m/s
V	Volume	Lt
Greek symbols		
ρ	Density	Kg/m^3
ϕ	Equivalence Ratio	
λ	Thermal conductivity	$W/m.K$
μ	Dynamic Viscosity	$kg/m.s$
Subscripts		
ad	Ambient	
Air	Air flow	
m	Average number of hydrogen atoms in LPG	
n	Average number of carbon atoms in LPG	
s	Specie	
St.	Stoichiometric	
act.	Actual	
AR	Aspect Ratio	
Abbreviations		
CFD	Computational Fluid Dynamics	
CC	Combustion Chamber	
FOAM	Field Operation and Manipulation	
LPG	Liquified Petroleum Gas	
2D	Two Dimensional	

CHAPTER ONE
INTRODUCTION

CHAPTER ONE

INTRODUCTION

1.1 Introduction

The primary objective of combustion studies is to acquire a comprehensive understanding of ignition mechanisms, species distribution, flame propagation, and energy release from combustion mixtures. Clearly, the practical consequences of such knowledge are the control of the combustion process from a safety standpoint and its use as a source of energy. The burning process is defined by (Rajput, 2008) as the rapid oxidation that produces heat, or "both light and heat," or the sluggish oxidation accompanied by a relatively small amount of heat and no light. Flame may or may not be associated with combustion processes.

The study of the combustion process necessitates the use of measuring instruments with a quick response time and a high spatial resolution in order to provide a precise description of the structure of the flame. The temperature of the fluid, reaction rates, "fluid flow and composition profiles", and transport coefficients of the numerous species are presented in the flame. In addition to laminar flame speed (Chigier, 1991).

1.2 Flame Propagation in A Cylinder

Flame propagation in a cylinder involves several parameters that affect the combustion process and performance. Here are some key parameters of flame propagation in a cylinder (Zhou et al., 2022):

- 1) Spark Timing: Spark timing refers to the precise moment when the spark plug ignites the air-fuel mixture in the cylinder. It influences the initiation of flame propagation and affects the combustion phasing,

efficiency, and power output.

- 2) **Flame Speed:** Flame speed, represents the rate at which the flame front propagates through the unburned mixture. In a cylinder, the flame speed is influenced by factors like fuel composition, air-fuel ratio, and turbulence intensity. Understanding and controlling the flame speed are important for achieving desired combustion characteristics.
- 3) **Turbulent Flame Interaction:** Turbulent flow affects flame propagation by enhancing mixing and increasing the flame surface area. The interaction between the turbulent flow and the flame front significantly influences the combustion process, including flame speed, heat release, and flame stability.
- 4) **Residual Gas Effects:** In the cylinder, a certain amount of exhaust gases from the previous combustion cycle remains, known as residual gases. Residual gas effects, including temperature, composition, and dilution, influence the combustion process and flame propagation.

These parameters interact with each other and need to be carefully controlled and optimized for efficient combustion. cylinder design, fuel injection strategies, spark plug configuration, and combustion chamber geometry are among the factors that can be tailored to improve flame propagation and overall performance (Beretta et al., 1983; Tewarson & Khan, 1988).

1.3 Premixed flames Dynamics in Tubes

Depending on the characteristics of fuel and oxidant mixing, there are three types of combustion: premixed, partially premixed, and diffusion or non-premixed. This investigation examines the laminar flame speed in diffusion, partially premixed, and premixed modes of liquified petroleum

(Huth & Heilos, 2013). Premixed flame is the mode of combustion that occurs when fuel and oxidizer are combined before combustion. Numerous practical combustion devices feature premixed flames (Insidoro, 1992).

In the premixed phase, the fuel and oxidizer are molecularly mixed outside the combustion chamber before combustion. In this mode, a flame front swiftly moves into the unburned mixture with a finite reaction rate and a characteristic velocity. Based on the rate of flame propagation, premixed combustion is classified as either deflagration or detonation. Expansion combustion occurs when the speed of the flame front is less than the local speed of sound, whereas compression combustion occurs when the flame propagates quicker than the local speed of sound (Hariharan, 2016).

When a combustible mixture is ignited by a weak ignition, the flame may undergo various propagation and combustion regimes as shown in Figure 1.1. These regimes include (1) weak ignition, (2) laminar flame, (3) wrinkled laminar flame, (4) turbulent flame, and (5) quasi-detonation/detonation. The flame first develops a smooth laminar flame, which is controlled by laminar burning velocity and expansion ratio (McAllister et al., 2011), (Strasser & Chamoun, 2014).

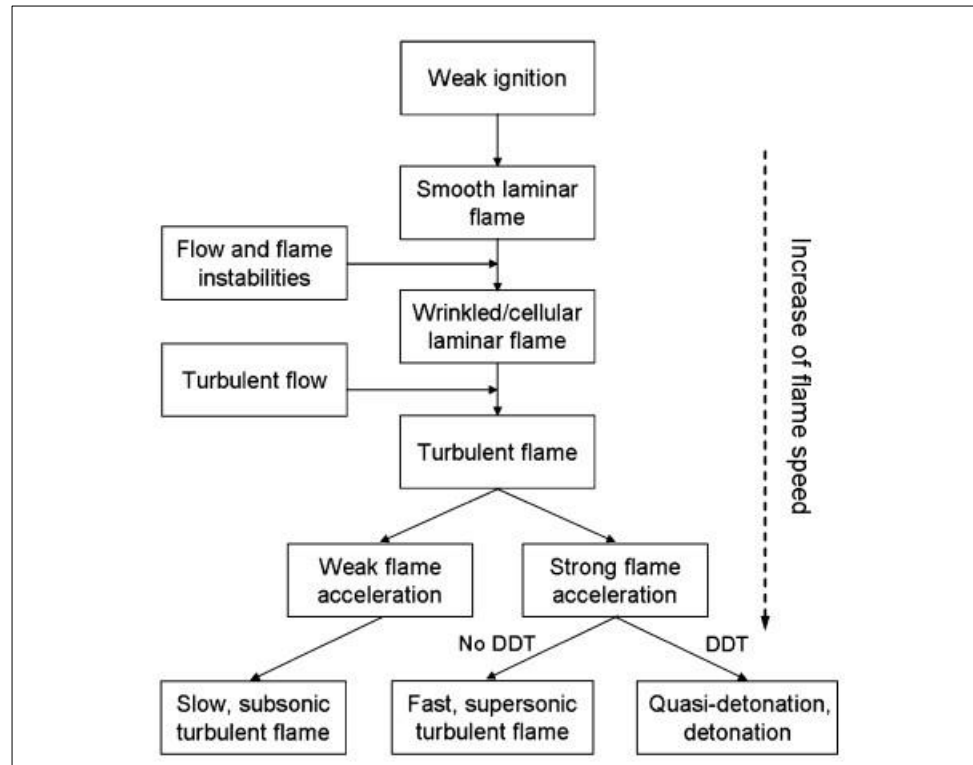


Figure 1.1: Schematic showing possible propagation regimes of premixed flame in a tube (Arpaia, 2019)

However, the flame can develop wrinkled and cellular structures due to flame instabilities, which can lead to an increase in flame surface area and acceleration of the flaming. Figure 1.1 schematic showing possible propagation regimes of premixed flame in a tube can also be generated by the interactions between the flame and acoustic waves. Turbulence can also promote flame acceleration by increasing the flame surface area and heat and mass transfer rates. However, flame deceleration may occur when the flame reaches tube walls due to the quenching effects of the wall. The flame may also experience deflagration mode, leading to DDT. Laminar flame is an essential topic in combustion and explosion science..(Al-Malki, 2013; Rashwan et al., 2017).

1.4 Burning Velocity and Flame Speed

The laminar burning velocity is the velocity of a one-dimensional flame in which an unburned mélange moves perpendicular to a wave surface through the combustion wave as shown in Figure 1.2. This parameter is regarded as one of the fundamental parameters of the combustion process because it contains information about the mixture's physicochemical properties (Williams, 2018). The velocity at which the flame propagates into a quiescent premixed, unburned mixture in front of the flame (Balusamy et al., 2009; Rahim et al., 2008). For the sake of brevity, a short list of the differences between burning velocity and flame speed is given in Table 1.2. Parameters are classified by definition, combustion type, influencing factors, measurement unit, and Context.

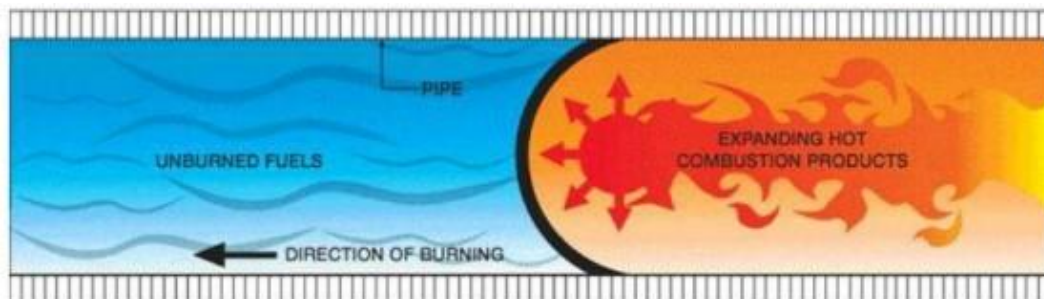


Figure 1.2: Laminar Premixed Flame and Combustion wave (Seidel, 2019)

Table 1.1: The difference between burning velocity and flame speed (Cloney et al., 2018)

Parameter	Burning Velocity	Flame Speed
Definition	Rate of flame propagation through a combustible mixture under quiescent conditions.	General term for the speed of a flame front propagation. Can refer to both premixed and diffusion flames.
Influencing Factors	Fuel composition, temperature, pressure, concentration gradients.	Fuel composition, mixture stoichiometry, flame thickness, heat release rate (in premixed flames). Fuel and oxidizer concentrations, fuel droplet size, turbulence intensity, mixing characteristics (in diffusion

Parameter	Burning Velocity	Flame Speed
		flames).
Context	Specifically refers to the speed of combustion in quiescent conditions.	A broad term encompassing various types of flame propagation. Can be used interchangeably with burning velocity in certain cases.

1.5 Flame Speed Measurement Techniques

The measurement of the laminar flame velocity of a premixed flame is a longstanding issue in the field of combustion. This issue extends beyond the realm of academia and is not confined just to laminar flames. The velocity of the premixed flame is a crucial element in the majority of supercharged combustion systems. Determining or computing laminar velocities continues to be a difficult task. The measurement of laminar flame velocities may be conducted using several techniques, including the tube-scattering flame, stagnation point flame, unstable spherical flame, convective flow method, and orifice burner.

Both experiments and simulations may be used for all procedures. The first approach seems straightforward: by measuring the displacement of the lamellar flame over time inside a tube, one may determine the velocity of the flame (Londoño et al., 2013).

1.6 Flame propagation applications

Flame propagation is defined as the progress (spread) of the flame inside the engine cylinder or any (combustible environment) outward from the point at which the combustion started. It has various applications in different fields. Here's a Table 1.2 summarizing some common applications of flame propagation:

Table 1.2: Flame propagation applications (Ballester & García-Armingol, 2010)

Application	Description	Pictures
<p>Combustion Systems</p>	<p>Designing and optimizing combustion systems such as gas turbines, engines, boilers, and furnaces for efficient and safe operation.</p>	
<p>Automotive Engines</p>	<p>Studying flame propagation in internal combustion engines to improve performance, fuel efficiency, and emissions control.</p>	
<p>Aerospace Applications</p>	<p>Analyzing and controlling flame propagation in aerospace systems, such as rocket engines and combustion chambers, for reliable and efficient operation.</p>	

1.7 Problem Statement

This study addresses the Problem Statement with the following:

- 1) The increasing energy demand makes fossil-fuel combustion attract great attention due to the rise in fuel consumption and greenhouse gas emissions. The combustion results in the emission of harmful greenhouse gases GHG including CO₂, CO, NO_x, SO_x, etc.
- 2) The pipeline length exerts a great influence on flame propagation characteristics, which are affected by the fuel type. The fuel type also affects the formation of the pollutant.
- 3) The formation of tulip flame is particularly significant since the flame should not strike the combustion chamber walls for safety and system integrity considerations.
- 4) The research of describing and showcasing distinct forms of flame has become more vital than ever to boost combustion efficiency and minimize particulate emissions.

1.8 Objectives for the Present Work

This study aims to address the following:

- 1) studying the effect of different lengths of pipes in a horizontal manner and with different equivalence ratios on flame front propagation for Iraqi liquid petroleum gas and propane.
- 2) developing an experimental device and a numerical model using the OpenFOM program, where the experimental and numerical data focused light on these systems to enhance our knowledge and ability to regulate and improve combustion processes.
- 3) Determine the physical mechanisms behind the development of the tulip flame by studying flame front propagation in a horizontal tube.

1.9 Scope of Study

As discussed in the impact of LPG premixing on flame propagation for various hydrocarbons. where the flame speed of LPG was investigated solely using a horizontal combustion chamber with varying diameters and lengths, the primary focus of this present work is to conduct both experimental and numerical investigations on the flame propagation of Iraqi Liquefied Petroleum Gas (ILPG)/air-premixed mixtures. The experimental setup involves using a horizontal cylindrical combustion chamber made of Pyrex glass, with inner and outer diameters of 71mm and 76 mm, respectively, and a wall thickness of 5 mm. The length of the combustion chamber is set at 1500 mm. The experimental phase includes premixing the ILPG with air and injecting it into the combustion chamber. To analyze the shape and structure of the flame, a specially designed experimental apparatus has been constructed, incorporating a high-speed camera.

In addition to the experimental study, the scope of this work also entails a numerical investigation. A 2-D simulation for the combustion model will be implemented using the OpenFOAM CFD code and XiFOAM solvers shown in Figure 1.3. The numerical study aims to provide complementary insights into the flame propagation of ILPG/air-premixed mixtures. By combining experimental and numerical approaches, this study aims to comprehensively understand the flame behavior and characteristics of ILPG/air-premixed mixtures in a horizontal cylindrical combustion chamber. The findings from this research are expected to contribute valuable knowledge to the field of combustion science and potentially offer insights into optimizing LPG combustion systems for practical applications.

CHAPTER TWO
LITERATURE REVIEW

CHAPTER TWO

LITERATURE REVIEW

2.1 Introduction

In this section, embark on a comprehensive journey through the historical evolution of flame front propagation in horizontal tubes, aiming to shed light on the intricacies that govern this fascinating phenomenon. By examining the stages involved in flame propagation, from ignition to extinction, we gain crucial insights into the factors influencing the velocity, shape, and stability of flames. In addition to addressing the existing body of knowledge, this section also serves to identify a significant research gap in the field of flame front propagation. While various experimental and numerical investigations have provided valuable insights into the behavior of flames in horizontal tubes, there remains an underexplored area in the study of "tulip flames." Although the transition from outwardly pointed flames to inwardly pointing cusps has been documented, a comprehensive understanding of the underlying mechanisms governing this particular flame shape is yet to be fully elucidated.

2.2 Flame Propagation

Considerable and extensive research efforts have been devoted to the study of contained premixed flames, with roots tracing back to Ellis's pioneering investigations (Ellis, 1928). Ellis's seminal work involved meticulous documentation and visual capture of the transition in flame shape, revealing the evolution from an outwardly pointed or concave front to an inwardly pointing or convex cusp, particularly evident for aspect ratio (AR) values exceeding two. This distinctive flame shape later became known as the "tulip flame," as referred to by (Salamandra et al., 1958).

Subsequent to Ellis's contributions, comprehensive experimental studies on semi-open tubes were conducted by (Clanet & Searby, 1996; Mallard & Le Chatelier, 1883), while examinations on closed tubes were performed by (Dunn-Rankin & Sawyer, 1998; Guénoche, 1964; Starke & Roth, 1989). In pursuit of understanding the underlying mechanisms behind this flame structure transition, various hypotheses have emerged from the research community. Researchers (Dold & Joulin, 1995; Gonzalez et al., 1992; Marra & Continillo, 1996; Matalon & Metzener, 1997; N'konga et al., 1993) explored the impact of the Darrieus-Landau and Taylor instability on flame dynamics. Guenoche (Guénoche, 1964) delved into the interaction between the flame front and its self-generated pressure wave, revealing crucial insights into this intricate process. Researchers (Ellis, 1928; Marra & Continillo, 1996; Starke & Roth, 1989) directed their investigations towards comprehending the interplay of viscous flow with the flame front. Additionally, the interplay between vortical fluid flow and the flame front was thoroughly examined by (Hanford et al., 1994; Kaltayev et al., 2000; Matalon & Metzener, 1997; Metzener & Matalon, 2001).

Among the notable studies (Clanet & Searby, 1996), conducted an exhaustive experimental examination of confined flame propagation, providing a physically based analysis. They successfully identified distinctive time scales and processes associated with each of the four characteristic phases: ignition, skirt flame, tulip flame, and extinction. These investigations were conducted using half-open circular tubes with an aspect ratio (AR) of 6:60.

Despite the vast strides made in numerical analysis concerning tulip flames, validation through comparable experimental tests has been relatively limited, with (Kumar, 2011; Pizza et al., 2010), being prominent

contributors in this aspect of research.

The collective body of research on flame propagation, particularly the fascinating phenomena of tulip flames, has significantly enriched our understanding of combustion processes. The insights gained from these studies hold great potential for optimizing combustion efficiency and enhancing safety measures in diverse industrial applications. Nevertheless, further integration of numerical simulations with rigorous experimental validation will likely pave the way for a more comprehensive and accurate comprehension of the complexities governing flame front propagation in horizontal tubes.

2.3 Flame Propagation Stages

In the early stages of flame propagation, following ignition, the primary effect of flame acceleration is the increase in flame surface area, as demonstrated by (S Kerampran et al., 2001).

As the flame interacts with the back and side walls of the confinement pipe, it undergoes four distinct stages, as defined by (Clanet & Searby, 1996). Initially, the pipe walls have little effect on the propagation of the flame front, resulting in a hemispherical shape. In the second stage, the pipe walls begin to influence the flame propagation, leading to a radial flame propagation velocity towards the walls that approaches the laminar flame velocity. Simultaneously, the flame surface area expands, transforming into a finger-shaped flame, resulting in a considerable increase in axial velocity (Guénoche, 1964). Clanet and Searby established empirical relationships for the time when the flame reaches the pipe wall (t_{wall}) and the time when the flame front changes from spherical to finger-shaped (t_{sphere}) as shown in Equations 2.1 and 2.2 (Clanet & Searby, 1996):

$$t_{wall} = 0.2(r S_l) \pm 0.02(r S_l) \quad (2.1)$$

$$t_{sphere} = 0.1(r S_l) \pm 0.02(r S_l) \quad (2.2)$$

Where r is the radius of the pipe and S_l is the laminar burning velocity.

Furthermore, an analytical relationship between t_{wall} and t_{sphere} can be derived by considering the temporal variation of the volume of the burned gases and equating it to the mass consumption rate of fresh gas (Clanet & Searby, 1996):

$$t_{sphere} = t_{wall} - \frac{r}{S_l} \frac{1}{2\alpha} \ln\left(\frac{Z_{wall}}{r}\right) \quad (2.3)$$

Where α is the expansion ratio and Z_{wall} is the axial location of the flame front when it first comes into contact with the pipe side wall. Clanet and Searby also found that the time the flame reaches the pipe wall is nearly similar to the time when experiments demonstrate the first rise in pressure, Figure 2.1.

The subsequent stage in flame propagation occurs when the inversion to a tulip flame shape begins. The term "tulip flame" was initially used by (Salamandra et al., 1958) to describe the rapid change of flame shape from a forward finger to a backward cusp (Bussing & Pappas, 1994). The increase in pressure before the flame front generates flow in the opposite direction of flame front propagation, Figure 2.1.

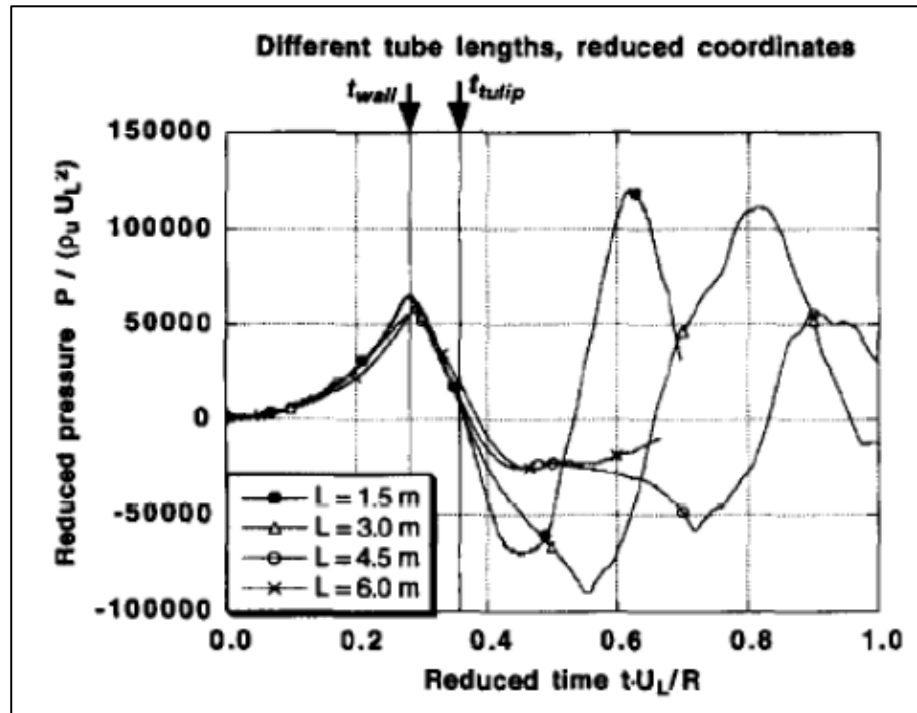


Figure 2.1: Pressure at the closed end of a shock tube while stoichiometric propane-air flames are present (Salamandra et al., 1958)

Clanet and Searby empirically established a linear function of the ratio of radius to laminar burning velocity to compute the time when the tulip flame occurs as shown in Equation 2.4 (Clanet & Searby, 1996):

$$t_{tulip} = 0.33 \left(\frac{r}{S_L} \right) \pm 0.02 \left(\frac{r}{S_L} \right) \quad (2.4)$$

From their investigations, Clanet and Searby concluded that the Rayleigh-Taylor instability is the primary source of the tulip inversion. This instability is caused by the pressure and density gradients at the interface between the burned light fluid and unburned denser mixture in the presence of acceleration or deceleration. The final stage involves flame propagation following tulip inversion. The flame surface inversion causes a decrease in surface area, leading to a slowing of the flame. In the absence of acoustic waves and with sufficient pipe length, this deceleration is followed by an acceleration caused by the increase in flame surface area when the flame

turns concave again toward the unburned mixture. Due to this new acceleration, the same instability mechanism can cause a new tulip inversion (Al-Dulaimi, 2017), leading to deceleration of the flame propagation once more as shown in Figure 2.2.

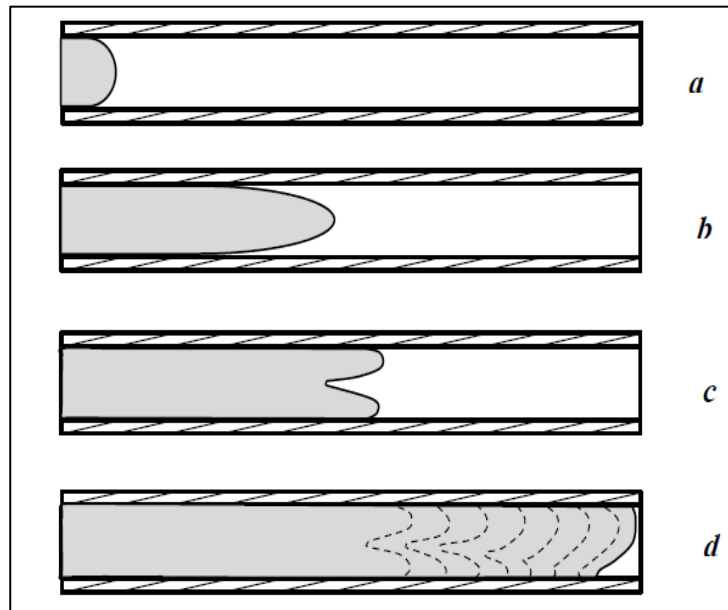


Figure 2.2: The four stages of flame propagation (a) hemispherical shape. (b) finger shape, (c) tulip flame. (d) flame surface inversion from (Al-Dulaimi, 2017)

Xiao (Xiao et al., 2015) presented a five-stage formation of a premixed flame in tubes: a spherical flame, a finger shaped flame, a flame with skirts touching the sides, a tulip flame, and finally a deformed tulip flame.

Markstein (Markstein, 2014), proposed that closed-tube propagation begins with an oscillating flame (related to the structural inversion from a finger flame to a tulip flame), followed by a pulsing flame (referring to the evolution from a tulip flame to a distorted tulip flame, without significant structural inversion). There are similarities in flame structures when compared to open-tube flame propagation, but the sequencing of the structures is different. The boundary conditions of the tube differentiate

open-ended and closed-tube flame propagation. Pressure waves are reflected off both ends of closed tubes, but refracted in open-ended tubes. The pressure readings in both configurations reflect this difference, with closed tubes steadily growing with slight oscillations, whereas open-ended tubes fluctuate along the x -axis with increasing amplitude and eventually decreasing. The disappearance of the cusp in open-ended tubes after the distorted tulip flame could be attributed to pressure wave refraction at the tube end, resulting in a succession of rarefaction and compression waves.

Vitaly Bychkov (Bychkov et al., 2007) demonstrated the propagation of a flame in a cylindrical tube of radius R with adiabatic walls, where the flame is started at the symmetry axis at the tube's closed end, resulting in an initial hemispherical shape that evolves into a finger-shaped flame as shown in Figure 2.3.

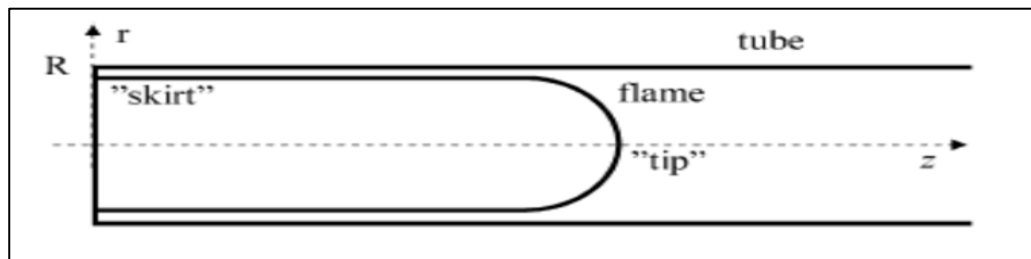


Figure 2.3: Geometry of a flame acceleration due to the initial condition form (Bychkov et al., 2007)

Nazrein Adrian (bin Amaludin et al., 2022), studied premixed flame propagation in open-ended horizontal tubes and observed that the flame profile becomes convex towards the unburned gas and spreads gradually down the tube faster than the laminar combustion velocity. The flame enters a self-induced longitudinal acoustic field about halfway down the tube, with the frequency of oscillations determined by the diameter of the tube.

Tulip flame initiation and proliferation were investigated by (Taniyama & Fujita, 2014), linking it to the variable pressure in flame

confinement, Figure 2.4.

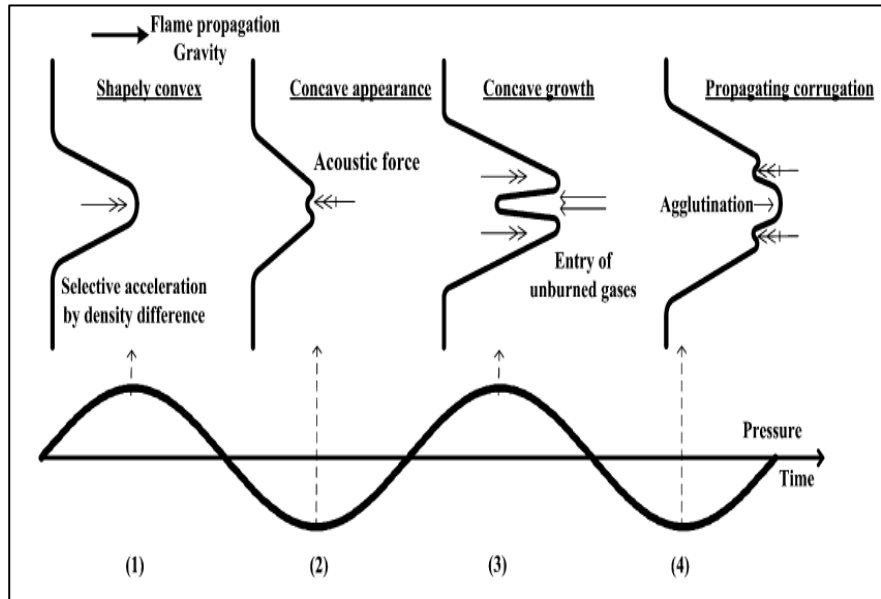


Figure 2.4: Tulip flame initiation and proliferation reproduced with permission from (Taniyama & Fujita, 2014)

Xiao conducted substantial computational and experimental research on the production of a tulip flame and postulated the formation of a deformed tulip flame due to vortex generation at the back of the tulip flame lips, as shown in Figure 2.5. However, the formation of a deformed tulip flame is not observed in every propagating flame (Xiao et al., 2013).

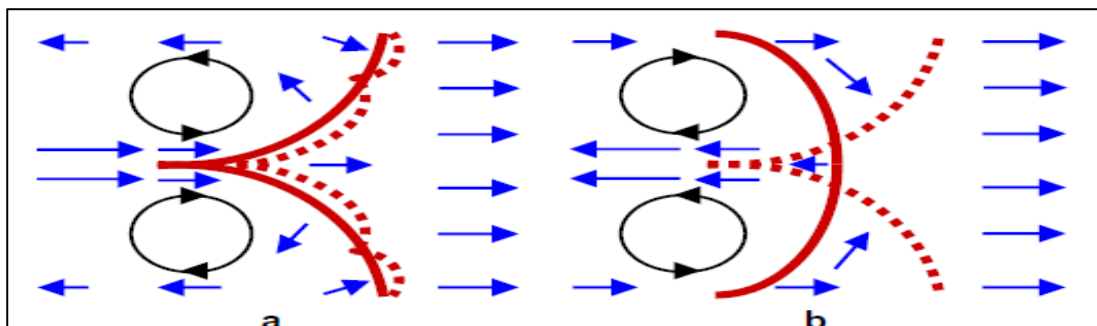


Figure 2.5: The formation of a deformed tulip flame (a) and a traditional tulip flame (b). the original flame shape is indicated by solid lines, while the succeeding flame shape is indicated by dashed lines. The characteristic flow velocity field is indicated by arrows. Reproduced with permission from (Xiao et al., 2013)

From a different perspective, both experimental and numerical investigations suggest that tulip flame formation is a fluid dynamic process rather than solely an instability (Hariharan & Wichman, 2014; Xiao et al., 2013). Xiao's research proposed a five-stage transition from a curved flame to a distorted tulip flame:

- 1) A hemispherical flame expanding outward, unaffected by sidewalls;
- 2) An axially elongated finger-shaped flame due to confinement and rapid increase of flame surface area;
- 3) An elongated flame in contact with the sides, causing surface area reduction;
- 4) Tulip flame formation after flame inversion with a cusp; and
- 5) The eventual formation of a deformed tulip flame, but not in every propagating flame (Xiao et al., 2015), as shown in Figure 2.6.

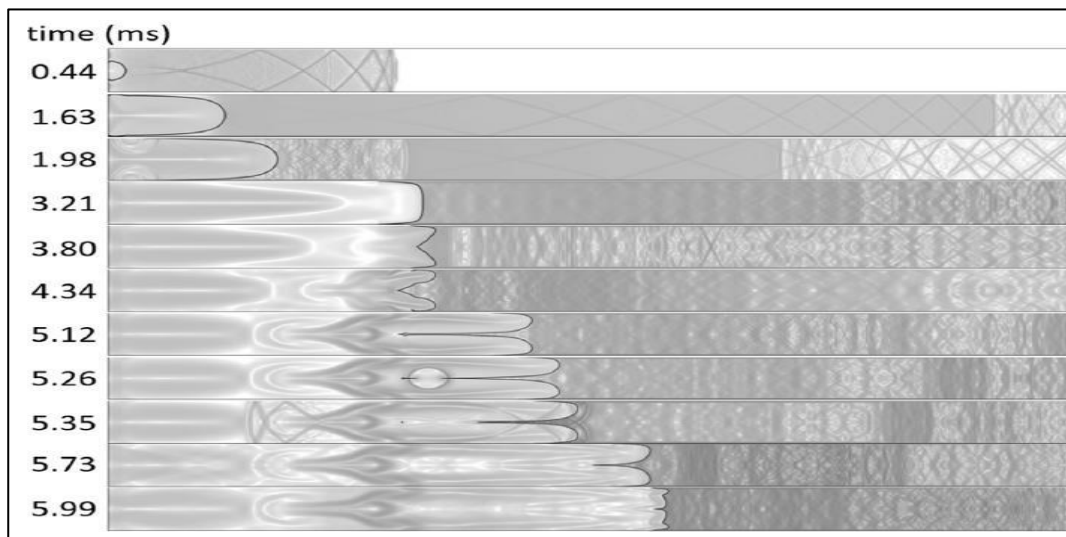


Figure 2.6: A progression of numerical schlieren pictures from a regular flame to a warped tulip flame, reproduction of (Xiao et al., 2015)

The velocity field and flow field structure were analyzed to understand their impact on the flame. Perry and Chong (Perry & Chong, 1987) developed a classification system for fluid topology based on the

surface's Euler characteristic ' X ,' which can be used to characterize complex fluid systems using critical point concepts.

The Euler characteristic for a surface in the flow field can be expressed as Equation 2.5:

$$\begin{aligned} X_{surface} &= X_{sphere} - 2 \sum handles - \sum holes \\ &= \sum nodes - \sum saddles \end{aligned} \quad (2.5)$$

The Euler characteristic equation can be expressed in an easily to use format as an alternative method proposed:

$$X_{surface} = \left(2 \sum N + \sum N' \right) - \left(2 \sum S + \sum S' \right) \quad (2.6)$$

In Equation 2.6, half-nodes (N') and half-saddles (S') appear on the perimeter (boundary) of a considered 2D surface, whereas the nodes (N) and saddles (S) appear within a control volume. Half-saddles and half-nodes characterize single points at the walls during flame propagation in a closed end system. The saddle formed after ignition, an internal singularity, does not travel toward the flame until the flame skirts are extinguished by the side walls. The proliferation of this saddle point and the formation of further nodes, half-nodes, saddles, and half-saddles have been thoroughly investigated (Foss, 2004).

In summary, extensive research has been dedicated to understanding flame propagation in confined horizontal tubes. The four distinct stages of flame propagation involve the initial hemispherical shape, followed by the finger-shaped flame, the tulip flame, and finally, flame surface inversion. The formation of tulip flames has been linked to the Rayleigh-Taylor

instability caused by pressure and density gradients at the flame interface. Various research studies have shed light on the complexity of tulip flame formation, with investigations of fluid dynamics, flame structure transitions, and boundary conditions. Further research in this field promises to deepen our understanding of combustion processes and improve safety measures in industrial applications.

2.3.1 Spherical flame

Upon ignition, a hemispherical flame front emerges, with its radius growing in conjunction with the fluid flow velocity within the control volume. The flow streamlines are illustrated on the response contour in Figure 2.7a. As the spherical flame expands, a stagnation point generated at the moment of ignition undergoes minimal displacement to the right along the centerline. Utilizing the streamline as a reference, several topological properties are identified, as shown in Figure 2.7a. The graph consists of two nodes, three half-nodes, three half saddles, and one saddle. Applying Equation 2.6, the Euler characteristic number for the control volume is found to be $X = 2$. The boundary layer attenuates the recirculation vortex formed near the wall in the unburned mixture after ignition (Hariharan & Wichman, 2014).

This initial stage of flame propagation, characterized by the captivating spherical flame, sets the foundation for the subsequent phases in the journey of combustion within the confined horizontal tube. As the flame continues its progression, transitioning through different shapes and stages, it unravels the complexities and intricacies of combustion processes, providing invaluable insights for various engineering and safety applications.

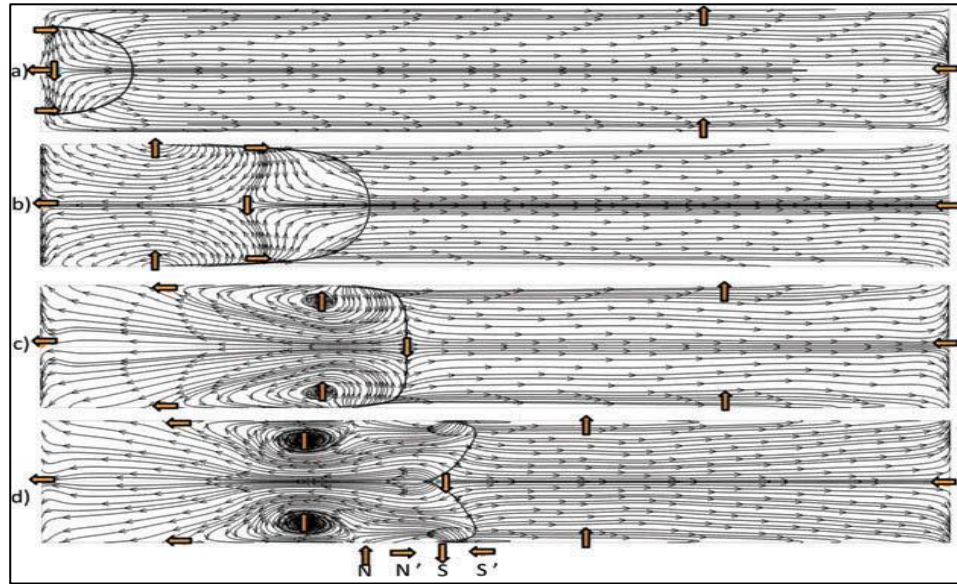


Figure 2.7: Plots of the streamlines in the channel at different times throughout the combustion process. (a) ignition stage; (b) finger flame stage; (c) planar flame stage; (d) propagating tulip flame stage. The nodes (N), saddles (S), half-nodes (N'), and half-saddles (S') are depicted in each illustration. At $X = 2$, the Euler characteristic is constant throughout the whole combustion process (Hariharan & Wichman, 2014)

2.3.2 Finger flame

As the flame propagation progresses from the initial spherical flame, a fascinating transformation takes place, giving rise to the distinctive "finger flame." The spherical flame expands more rapidly down the length of the combustion chamber than along its sides, leading to a lengthening of the front of the flame that resembles the shape of a finger. This elongated structure of the flame front marks a significant milestone in the combustion process within the confined horizontal tube. The evolution of the finger flame's topology is marked by the presence of two unique points at the ends of the side skirt, where the premixed flame is extinguished. These points are identified as half-nodes (N'), and they play a crucial role in driving the formation of the saddle point along the axis of the channel's centerline. The flow dynamics during this stage of flame propagation exhibit a compelling

arrangement of nodes, half-nodes, half saddles, and a saddle point (Hariharan & Wichman, 2014), as depicted in Figure 2.7b.

Figure 2.7b shows the intricate flow streamlines and the topological features of the finger flame. The presence of two nodes, two half-nodes, two half-saddles, and one saddle point characterizes the fascinating topology of the finger flame's flow field. The formation of these distinct points and their interactions contribute to shaping the elongated structure of the finger flame as it gracefully traverses the confined horizontal tube.

The Euler characteristic, a valuable mathematical measure capturing the inherent topology of the fluid system, is calculated for the flow field of the finger flame. Applying Equation 2.6, the Euler characteristic number is determined to be $X = 2$, providing a fundamental understanding of the complex flow patterns and structures present within the finger flame (Foss, 2004).

The emergence of the finger flame signifies a critical stage in flame propagation within the confined tube. The elongated shape of the flame front and the presence of distinct topological features offer valuable insights into the intricate interplay between fluid dynamics and combustion kinetics.

2.3.3 Planar flame

The flame front undergoes a transformation as it progresses further in its journey of propagation within the confined horizontal tube, eventually transitioning into the distinctive "planar flame." The unique point, represented by the saddle, approaches the flame front, resulting in a flatter configuration. As this singular point coincides with the reaction front, the flame achieves a completely planar shape (Foss, 2004).

The quenching of the side skirts by the cold side walls initiates a

recirculation pattern, both in the unburned and burned mixtures. This recirculation pattern gives rise to specific changes in the flow dynamics, particularly in the region of the burned gas. The half-nodes present in the burned gas region transform into a pair of nodes and half saddles (S') that now exist independently. The formation of these new topological features adds complexity to the flame structure during this stage of propagation.

Figure 2.7c presents a visual representation of the flow streamlines and the topological properties of the planar flame. The planar flame's flow field is characterized by the presence of four nodes, four half-saddles, and one saddle within the control volume. These topological features intricately define the shape and behavior of the planar flame as it progresses through the confined horizontal tube (Hariharan & Wichman, 2014).

The Euler characteristic number, a significant mathematical measure reflecting the underlying topology of the fluid system, is computed for the flow field of the planar flame. Applying Equation 2.6, the Euler characteristic number is revealed to be $X = 2$, underscoring the fascinating complexity of the flow patterns and structures present within the planar flame.

The emergence of the planar flame marks a critical stage in flame propagation within the confined tube. The transition to a flatter configuration and the intricate changes in topological features provide valuable insights into the underlying fluid dynamics and combustion phenomena at play during this phase of flame propagation.

2.3.4 Tulip flame

As the flame propagation reaches the far end of the channel, a mesmerizing phenomenon occurs, giving rise to the distinctive "tulip flame"

(S Kerampran et al., 2001). During this stage, the stagnation point gracefully traverses through the flame front while maintaining a constant distance from the tulip cusp, which lies at the channel's midline. This intriguing motion of the stagnation point induces an increase in the velocity of the unburned mixture flowing toward the flame's centerline, acting as a source of flame stretch. The tulip cusp, being a pivotal point of the flame's geometry, plays a crucial role in shaping the flame front during this phase of propagation.

Notably, until the last stage of the combustion process in the channel, which is either extinction or quenching, the flame area continues to expand to its full extent. During this expansion, the propagation speed of the flame front remains virtually constant, and the entire structure moves coherently as a unit. The tulip flame exhibits a unique flow field configuration within the control volume, characterized by the presence of four nodes, four half saddles, and one saddle (Xiao et al., 2015), as shown in Figure 2.6.

Figure 2.6 visually illustrates the behavior of the tulip flame, emphasizing the constant spacing between the flame front and the saddle point as the saddle moves through the flame. Regardless of the specific geometry of the flame front, it is intriguing to note that the Euler characteristic of the fluid flow within the combustion chamber remains constant throughout the flame propagation process (Hariharan & Wichman, 2014). This valuable insight suggests that while the quantity and type of singular points may vary during different stages of flame propagation, the overall flow topology, as measured by the Euler characteristic, remains unaltered.

The emergence of the tulip flame signifies a critical stage in flame propagation within the confined horizontal tube. The distinctive geometry

and flow characteristics of the tulip flame highlight the intricate interplay between fluid dynamics, flame stretch, and combustion kinetics (Perry & Chong, 1987), as shown in Figure 2.8.

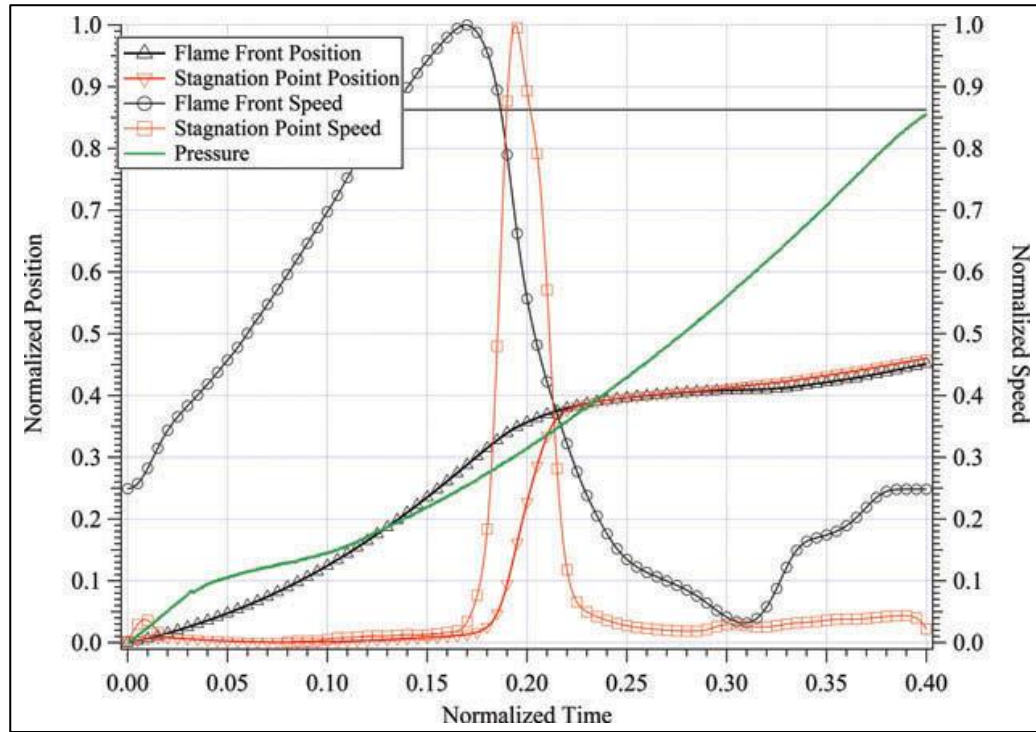


Figure 2.8: Normalized plot displays the position and velocity of the flame front and stagnation point, as well as the pressure $p(t)$, pressure change rate (dp/dt), stagnation front speed, and flame front speed vs channel time t . Position and velocity of the flame are normalized to their greatest values (Hariharan & Wichman, 2014)

Zakaria Movahedi (Movahedi, 2017) investigated the propagation of premixed propane-air flames within ducts under two distinct conditions: fully opened and fully closed end outlets. The study meticulously examines the dynamics of flame behavior and its propagation stages while placing a particular emphasis on the interchange effect between the flame and the feeding flow. Advanced numerical simulations are conducted to elucidate the physical mechanisms responsible for the formation of the tulip flame shape and its subsequent inversions. Furthermore, comparisons are drawn to

highlight both the similarities and differences of these observed phenomena. Numerical analyses are executed using two computational fluid dynamics (CFD) software packages, namely Star CCM+ and OpenFOAM, leveraging a range of combustion models the findings offer valuable insights into the intricate interplay between flame propagation and duct flow dynamics, the formation of the tulip flame, and its subsequent inversions, extending the frontiers of combustion research within confined geometries.

Siba and Ratan (Siba & Ratan, 2018) conducted an experimental study on the propagation of premixed LPG-air flames in a rectangular channel. Two types of combustion chambers, a half-open and a closed duct, were investigated. In the half-open duct, a regular curved flame was observed, while in the closed duct, a distinct "tulip flame" was observed. Peculiar detonation structures were also observed near the closed side of the duct. The velocity of flame propagation decreased after the formation of the tulip flame. The paper explores factors such as pressure fluctuation, wall roughness, and hydrodynamic effects that contribute to the formation of the tulip flame. The experimental setup included an uncooled rectangular duct with acrylic glass sides, and high-speed camera imaging was used for flame visualization. The findings provide insights into premixed LPG-air flame behavior and contribute to the understanding of flame front characteristics and the formation of tulip flames in closed and opened ducts.

2.4 Factors Affecting Flame Propagation

Flame propagation is influenced by a multitude of factors that play significant roles in shaping the behavior and characteristics of the combustion process. Understanding these factors is crucial for optimizing

flame propagation in various applications and ensuring safety in industrial and engineering processes. The following are the key factors that have been extensively studied for their impact on flame propagation and they were dealt with in this research (Chen et al., 2023):

- **Fuel-Air Mixture and Equivalence Ratio:** The composition and ratio of the fuel-air mixture have a direct influence on the flame's ignition, stability, and propagation speed. An optimal mixture is necessary to achieve efficient and controlled combustion. Also, the ratio of actual fuel-air mixture to the stoichiometric mixture affects flame stability and the formation of soot and pollutants.
- **Fuel Type:** The type of fuel used significantly influences flame propagation, affecting factors such as combustion rate, flame temperature, stability, and overall characteristics of the flame. Different fuels exhibit varying combustion behaviors, which impact the speed and intensity of flame propagation in a combustion chamber or tube.
- **Tube Length:** Tube length directly impacts flame propagation by influencing the distance the flame must travel before encountering boundaries. Longer tubes provide more space for the flame to develop and can result in different flame behaviors compared to shorter tubes. Tube length affects flame residence time, propagation speed, and overall stability.

Temperature, pressure, heat loss and cooling, turbulence, flame stretch, chemical kinetics, heat release rate, and turbulent flame speed are all critical factors influencing flame propagation in a combustion chamber or tube. The initial temperature of reactants plays a significant role in determining the rate of chemical reactions and ignition delay time,

ultimately affecting the speed and intensity of flame propagation. Researchers and engineers continuously strive to gain deeper insights into these factors to optimize combustion processes and promote energy efficiency while mitigating environmental impacts (Ballester & García-Armingol, 2010). Some literatures about the most effective factors are listed here.

2.4.1 Fuel-air mixture and equivalence ratio

The equivalence ratio represents the ratio of fuel to oxidizer in a mixture relative to the stoichiometric condition. Mathematically, it is expressed as Equation 2.7, where CF denotes the mole concentration of fuel, CA denotes the mole concentration of air, and the subscript st denotes the mole concentration at stoichiometry:

$$\phi = \frac{CF/CA}{(CF/CA)_{st}} \quad (2.7)$$

Richardson and Chen (Richardson & Chen, 2017) conducted direct numerical simulations to investigate the influence of equivalent ratio stratification on turbulent flame propagation. The study employed accurate multi-step kinetic modeling for methane-air combustion, simulating turbulent slot-Bunsen flame configurations in three dimensions. Comparisons were made between one perfectly premixed and three equivalent ratio-stratified cases, where the mean gradient was aligned, tangential to, or opposite to the mean flame brush. Flame surface area and burning intensity were analyzed based on these simulations. Additionally, displacement speed statistics conditioned on the flame-normal equivalent ratio gradient were examined to assess the local effects of stratification. The

study revealed that equivalent ratio stratification impacts the flame surface area due to changes in the surface-averaged consumption rate and differential propagation effects resulting from flame speed oscillations.

Cho and Tim (Cho & Lieuwen, 2005) analyzed the flame response to equivalence ratio perturbations, observing three disturbances that govern heat release: reaction heat, flame speed, and flame area. Equivalence ratio oscillations induce the first two disturbances, while flame speed variations cause the third. The transfer function of flame response was studied at various Strouhal numbers (frequency of flame length). At low Strouhal numbers, the flame response is dominated by the reaction disturbance heat (axial flow velocity). As Strouhal number approaches 1, all three disturbances become equally significant. At low Strouhal numbers, the flame response is found to increase with decreasing mean equivalence ratio ($\phi = 1$), supporting previous heuristic arguments. Additionally, the study investigated the sensitivity of this transfer function to uncertainties in mean flame position.

Ax and Meier (Ax & Meier, 2016) conducted an extensive experimental examination of laminar premixed methane-air flames under different equivalent ratio oscillations. Methane was periodically added to the stationary fuel/airflow of a lean premixed flame, and parametric studies explored flame reaction as a function of modulation amplitude and frequency. Low pressure was utilized to improve spatial resolution across and within the flame front, approximating the flame's temporal and length scales, while causing equivalent ratio oscillations of 10 Hz. The results demonstrated various interacting effects depending on the oscillation frequency. At low frequency, a "macroscopic" flame reaction occurred due to changes in laminar flame speed, flow velocity, and position. At high

frequencies, the flame tip maintained its position, but species profiles across the flame front showed significant phase shifts relative to each other, rendering the flame behavior uncharacterizable by steady states during the oscillation period.

2.4.2. Fuel type

Liquefied Petroleum Gas (LPG) has been extensively studied for its advantages, including its high heating value of approximately 46.1 MJ/kg , surpassing fuel oil (42.5 MJ/kg) and gasoline (43.5 MJ/kg), (Park et al., 2011; Wierzba & Wang, 2006). Other benefits of LPG include its near absence of sulfur, resulting in cleaner combustion with minimal ash content. Additionally, LPG burns in the engine in a gaseous state, leading to less corrosion and engine wear compared to gasoline. Its high-octane level enables LPG to mix more effectively with air, promoting complete combustion and producing fewer carbon emissions than gasoline. This results in extended spark plug life and reduces the frequency of necessary oil changes. Moreover, LPG offers flame stability and minimal processing costs (Ax & Meier, 2016; Cho & Lieuwen, 2005; Park et al., 2011; Richardson & Chen, 2017; Said et al., 2019; Wierzba & Wang, 2006).

However, LPG also exhibits several disadvantages that need to be considered. Its boiling point below room temperature can cause issues with cold-weather starting, especially at low vapor pressure and temperatures. Additionally, LPG has a lower energy density per unit volume (26 MJ/L) compared to gasoline and fuel oil, with a relative density around $0.5\text{-}0.6 \text{ kg/L}$, while gasoline has a relative density of $0.71\text{-}0.75 \text{ kg/L}$. This lower energy density affects the driving range of vehicles using LPG as fuel. Another drawback is that LPG is generally more expensive than other fuel

options. Moreover, during burning, LPG emits a significant amount of carbon dioxide (CO_2) and unburned hydrocarbons (HC), contributing to environmental problems. Furthermore, the limited flammability range of LPG restricts its utilization in certain applications (Jang et al., 2019; Richardson & Chen, 2017).

Ibrahim (Ibrahim et al., 2015) conducted a study on the laminar flame speed of methane and LPG fuels. Their research found that the laminar flame speed (SL) of any mixture of these two fuels is greater than the SL of each fuel when used separately. Increasing the proportion of LPG in the mixture, particularly near the stoichiometric condition, substantially improves the flame speed. The specific reason for this phenomenon is not yet clear, but it may be related to the projected increase in flame temperature resulting from the addition of LPG to the mixture. This change in temperature might lead to alterations in the rate of synthesis and consumption of H, O, OH, and CH_3 radicals in the reaction zone.

In a separate study by **Wang, Qiu, and Jiang** (Wang et al., 2008), a numerical analysis of hydrogen-enhanced LPG + air flames were conducted. The researchers investigated the fluctuations of the adiabatic burning velocity under different combustion conditions (equivalence ratio = 0.7-1.4). The fuel's hydrogen percentage ranged from 0% to 45%, while its dilution factor ranged from 21% to 16%. Their study involved validating the chemical kinetic model against fundamental combustion data and performing separate simulations of opposed-jet, symmetric, and twin flame designs. The calculations indicated that hydrogen-enhanced LPG/air-premixed flames exhibited greater stability at high flame strain. Additionally, the addition of hydrogen extended the lean flammability limits. It is essential to consider these findings in the context of other types

of fuels as well. Each fuel type comes with its unique set of advantages and disadvantages, and the choice of fuel should take into account factors such as energy efficiency, environmental impact, availability, and cost. Other types of fuels that are commonly used or being researched for various applications include gasoline, diesel, natural gas (Compressed Natural Gas-CNG and Liquefied Natural Gas-LNG), and biofuels (Mjbel et al., 2021). A comprehensive evaluation of these fuels can aid in making informed decisions about the most suitable fuel for specific applications, with consideration for both performance and environmental considerations.

Hamza M. Mjbel (Mjbel et al., 2021), analyzed the laminar flame speed of a pre-mixed Iraqi LPG/air mixture in a horizontal cylindrical combustion chamber. Experimental measurements and numerical simulations are conducted to analyze the flame speed at various equivalent ratios. The experiments involve recording the flame propagation using a high-speed camera and analyzing the videos to determine the laminar flame speed. The numerical simulations utilize the Ansys Fluent program and the Chemkin USC Mech 2.0 model to predict flame speed. Both the experimental and numerical results demonstrate that the flame speed increases with the equivalence ratio, peaking at the stoichiometric ratio, and decreases as the mixture becomes richer. The study also examines the influence of the propane/butane ratio on the flame speed, revealing that a higher propane ratio enhances the flame speed. These findings enhance our understanding of laminar flame behavior in LPG-air mixtures and offer valuable insights for the optimization and design of combustion systems.

Omid Aghaabbasi (Aghaabbasi, 2021) focuses on the use of computational fluid dynamics (CFD) simulations to study the behavior of hydrogen-air explosions. employs the OpenFOAM CFD toolbox and the

XiFoam solver to simulate flame acceleration in explosions within a 2D channel. The parameters analyzed include flame front position, flame speed, equivalence ratio, and pressure. The results show that increasing fuel concentration and moving from fuel-lean to fuel-rich conditions lead to faster flame front propagation, higher velocity, and higher pressure. The behavior is observed in both homogeneous and inhomogeneous H_2 –air mixtures. However, the homogeneous mixture exhibits greater flame elongation and acceleration due to the presence of a larger flammable mixture.

2.4.3 Tube length

Kerampran (KERAMPRAN et al., 2000) conducted experimental studies using propane-air, ethylene-air, and acetylene-air mixtures in tubes of varying lengths. They observed oscillatory behavior in the flame trajectory, which correlated with pressure records. The findings highlight the dependence of flame acceleration on mixture composition and tube length. The paper fills a gap in existing knowledge by focusing on the self-acceleration of flames in tubes closed at the ignition end, a situation conducive to deflagration to detonation transition (DDT). He emphasizes the importance of correlating pressure evolution with the flame propagation regime to ensure safety. The study provides valuable insights and reproducible data that can contribute to the modeling of flame acceleration phenomena. Overall, this research paper offers a significant contribution to the field of combustion science and technology, improving our understanding of flame behavior in confined spaces.

Xue Li (Xue et al., 2000) explored the effects of pipe length on propane-air explosion flames using numerical simulations and experimental

verification. The paper highlights the agreement between the realizable $k-\varepsilon$ model and experimental results, demonstrating the model's effectiveness in capturing the flame structure and propagation speed. The formation of tulip flames and the presence of vortices are examined, shedding light on their impact on the flow field. Furthermore, the study compares the flame behavior in open-ended and closed-ended pipes, emphasizing the role of reflected waves, turbulence, and combustion reactions. The findings contribute to a better understanding of flame dynamics and provide insights for improving safety measures in industries dealing with combustible gases. Overall, this research paper presents a comprehensive analysis of flame propagation in different pipe lengths, making it a valuable contribution to the field of combustion science.

S. Kerampran (S. Kerampran et al., 2001) presented a comprehensive study on flame propagation in tubes and its dependence on tube length. The authors conducted experiments using propane-air mixtures in a specially designed experimental set-up, allowing for accurate observations of flame behavior. It discusses the phenomenon of oscillatory flame propagation and its relation to tube length, as well as the influence of acoustics on flame oscillations. The experimental results are presented clearly through flame trajectories and pressure records, supported by quantitative analysis. Overall, this paper provides valuable insights into the complex dynamics of flame propagation in tubes and contributes to our understanding of flame behavior and industrial safety.

2.5 Summary

Table 2.1 shows a summary of the research close to my work in terms of the study method and its results.

Table 2.1: Summary of the researches close to my work

Authors	Conditions	Observations
Kerampran (S Kerampran et al., 2001)	Studied oscillating flame propagation in tubes closed at the ignition end and open at the other for several different reactive mixtures	The experimental results clearly demonstrate the oscillating behavior of the flame front as it propagates. They demonstrate that oscillation frequency and amplitude depend on tube length, the speed of sound in the fresh mixture, and the initial velocity of the laminar flame. However, when the cross-section of the tube is altered, i.e. in the large tube, oscillating propagation modes are no longer detected under the same conditions as in the small tube. Conclusion: acoustics have a significant role in the flame acceleration mechanism
Cho and Tim (Cho & Lieuwen, 2005)	Analyzed the flame response to equivalence ratio perturbations and found that heat release is governed by the superposition of three disturbances: reaction heat, flame speed, and flame area.	The flame reaction to equivalence ratio oscillations increases as the mixture becomes leaner, supporting heuristic arguments from previous investigations.
Bychkov (Bychkov et al., 2007)	Studied the numerical and exponential acceleration of premixed laminar flames in the early stages of burning in tubes for the propane-air mixture with $\varphi = (0.7 - 1.4)$	The simulation results and theory are consistent with previous experiments, revealing the most intriguing stages of flame dynamics: hemispherical expansion, acceleration of the finger-shaped flame, rapid deceleration when the flame skirt sweeps along the tube side wall, and inversion of the flame shape, which can also be interpreted as a "tulip" flame
Taniyama and Osamu (Taniyama & Fujita, 2014)	Experiments were conducted on a 45-cm-long, 5-cm-inner-diameter combustion tube using C ₂ H ₄ /CO ₂ -O ₂ (Le < 1) flames. The flame fronts propagated downhill until	Results showed that the locally deformed flame changed into a corrugated structure at the front of the flame. This was followed by self-tribalization. The experiments used a CO ₂ laser irradiation method with a flame moving

Authors	Conditions	Observations
	they reached the closed bottom of a tube with an open end	downward in a tube. Careful observations showed that the concave structure appears just before the corrugated flame when the flame moves in a turbulent way
Hariharan and Indrek (Hariharan & Wichman, 2014)	Studied experimental and numerical research of premixed flame propagation in a combustion chamber consisting of a six-sided rectangular channel with a constant volume	The results of transient 2D numerical simulations are compared to the results of transient 3D experiments. Issues discussed are the appearance of oscillatory motions along the flame front and the influences of gravity on the flame structure. An explanation is provided for the formation of the "tulip" shape of the premixed flame front
Xiao (Xiao et al., 2015)	Studied numerical simulations of the formation and propagation of tulip and distorted tulip flames in a closed tube	The effect and facilitation of the creation of a deformed tulip flame (DTF) by triggering Rayleigh–Taylor instabilities. Hence, the creation of a DTF can be viewed as the consequence of Rayleigh–Taylor in stability driven by pressure waves.
Ibrahim (Ibrahim et al., 2015)	Studied the laminar flame speed of methane and LPG fuels	CH ₄ /LPG-air mixtures show that the SL of a mixture of these two fuels with any percentage is higher than the SL of both pure fuels when used separately.
Richardson and Chen (Richardson & Chen, 2017)	Used direct numerical simulation, the effect of equivalent ratio stratification on turbulent flame propagation was investigated. Accurate multi-step modeling of methane-air kinetics	The flame surface area is also affected by equivalent ratio stratification as a result of changes in the surface-averaged consumption rate and differential propagation effects resulting from oscillations in flame speed

Authors	Conditions	Observations
Zakaria Movahedi (Movahedi, 2017)	Investigated the propagation of premixed propane-air flames within ducts under two distinct conditions: fully opened and fully closed end outlets. The study meticulously examines the dynamics of flame behavior and its propagation stages while placing a particular emphasis on the interchange effect between the flame and the feeding flow	The findings offer valuable insights into the intricate interplay between flame propagation and duct flow dynamics, the formation of the tulip flame, and its subsequent inversions, extending the frontiers of combustion research within confined geometries
Siba and Ratan (Siba & Ratan, 2018)	Conducted an experimental study on the propagation of premixed LPG-air flames in a rectangular channel. Two types of combustion chambers, a half-open and a closed duct, were investigated. The experimental setup included an uncooled rectangular duct with acrylic glass sides, and high-speed camera imaging was used for flame visualization	The findings provide insights into premixed LPG-air flame behavior and contribute to the understanding of flame front characteristics and the formation of tulip flames in closed and opened ducts.
Nazrein Adrian (bin Amaludin et al., 2022)	Studied methane-air mixtures ($\phi = 1.2$) enriched with hydrogen ignited in an open-ended horizontal tube at 20 °C and an atmospheric pressure of 1.013 bar	The effects After ignition, the flame profile becomes convex toward the unburned gas and propagation gradually down the tube faster than the laminar combustion velocity. The flame enters a self-induced longitudinal acoustic field about halfway down the tube. The frequency of oscillations is determined by the diameter of the tube but is not exclusive
Hamza Mjbel (Mjbel et al., 2021)	Experimental and numerical the effect of the equivalence ratio (0.7-1.4) for the ILPG/AIR	The speed of the flame was calculated practically and numerically for the LPG fuel, as it was found that the combustion speed

Authors	Conditions	Observations
	<p>premixed on the laminar flame speed in horizontal cylindrical with length 1300mm and 180mm diameter.</p> <p>The condition 1atm and 300k</p>	<p>increased from the side of the weak mixture of the fuel (Equivalence ratio = 0.8) until it reached its maximum value at equivalence ratio = 1 and 1.1, then it began to decrease each increasing the amount of fuel in the mixture until it reached less Its value when the equivalence ratio = 1.2</p>
(Almyali, 2024)	<p>investigated the propagation of a mixed LPG-air flame inside a tube under two distinct conditions: fully open and fully closed end ports.</p> <p>The study carefully studies the dynamics of flame behavior and the stages of its propagation, with special emphasis on the effect of pipe lengths and equivalence ratio, taking into account the initial conditions, pressure 1 bar and temperature 300 K.</p>	<p>The results provide valuable insights into the complex interplay between flame propagation and tube flow dynamics, tulip flame formation and tulip flame recurrence, the effect of tube length and equivalence ratio on flame propagation phase formation, and its subsequent implications, expanding the boundaries of combustion research within confined geometries.</p>

CHAPTER THREE
NUMERICAL STUDY

CHAPTER THREE

NUMERICAL STUDY

3.1 Introduction

Computational fluid dynamics (CFD) techniques have revolutionized research methods, providing significant advantages over traditional laboratory experiments. Using CFD tools offers cost-effectiveness by eliminating the need for expensive physical test devices and equipment. These simulations require substantial processing capacity due to the intricacies of the mathematical models and the need for high-resolution grids. It is crucial to validate CFD results against experimental data to ensure accuracy. Despite these considerations, CFD tools provide researchers with a powerful and versatile approach to simulate and analyze fluid dynamics, heat transfer, and combustion processes, advancing scientific understanding and engineering applications.

In the present work, a CFD model has been developed and applied to investigate flame propagation and characteristics for various LPG/air mixtures with varying blending conditions. Chemical reactions and turbulent models would be utilized, necessitating significant computing resources. This chapter clarifies the numerical work of this investigation. Complex chemical reactions and turbulent models solved using OpenFOAM code have been used to simulate the combustion process of these mixtures.

3.2 Numerical Modeling and Methodology

Numerous commercial and non-commercial solvers, such as ANSYS CHEMKIN, CFX, FDS, and SMAFS, are used to solve numerical models in which chemical reactions and combustion are implemented. OpenFOAM

code (Field Operation and Manipulation) (Samantaray & Mohanta, 2015) has been chosen to solve the present numerical problems because it contains multiple solvers that investigate and cover various combustion scenarios, including the numerous effects nested in action with combustion details such as turbulence and radiation. Open GL (General License) code is yet another distinguishing feature of OpenFOAM.

3.2.1 OpenFOAM methodology

As mentioned previously, the OpenFOAM (Open Source of Field Operation and Manipulation) code is used to solve the computational domain for combustion in the current numerical simulation. The OpenFOAM code is written in C++. Concerning the combustion model, it can be solved with various solvers, including rho-Reacting-Foam, rho-Reacting-Buoyant-Foam, reactingFoam, FireFoam, and XiFoam (Paulasalo, 2019). In the current numerical simulation, the XiFoam solver is utilized to solve all applicable governing equations. XiFoam is a transient solver for compressible combustion with turbulence modeling in premixed and partially premixed conditions. This solver discretizes the PDE (partial differential equations) using the finite volume method (Kutkan & Guerrero, 2021; Povilaitis & Jaseliūnaitė, 2021).

3.2.2 Cases assumptions

The present study has been implemented using the XiFoam solver by considering the following assumptions for the current work:

- 1) The flow is unsteady, and the solver ceases at time when the residuals are converged.
- 2) (2-D) numerical simulation would be considered where the flow is considered in x and y coordinates while it would be neglected in z-

direction.

- 3) The flow is compressible.
- 4) The thermophysical properties for all the components are not constants.
- 5) All the reactants and the products of the combustion reactions are implemented in the multi-species solver.
- 6) The initial pressure and initial temperature is (1 bar and 300k)

3.2.3 CFD models

As previously indicated, the XiFoam solver is used in the current simulation to solve the current combustion model. In this solver, the PDE is discretized using the finite volume method. The XiFoam solver is an unsteady solver whose run duration and time step must be set so that Courant number. does not exceed the maximum value specified. A Courant number is a dimensionless value that represents the amount of time a particle spends in a single mesh cell (AD Number, 1980; Avhad, 2020). In this simulation, the maximal Courant number is set to 0.5, so:

$$Co.No. = \frac{u \Delta t}{\Delta x} \leq 0.5$$

However, in the current setup, the adjustable time step is turned on to avoid any divergence in the solution through the simulation. The PIMPLE algorithm is used to solve the pressure-velocity coupling, which represents a combination of the PISO (Pressure-Implicit-Split-Operator) algorithm and the SIMPLE (Semi-Implicit Method of Pressure-Linked-Equation) algorithm (Avhad, 2020).

Second-order scheme discretization LUST (linear-upwind stabilized transport) is used to discretize the momentum equation, while (Gauss

limited linear) is used for the other equations; the energy equation, the turbulence model equation (the standard k - ϵ model is utilized in the current work as would be discussed in the next sections), and species conservation equations. The combustion model is enabled in the case file, and the reactions were set properly, where there are different reactions according to different cases investigated in the present study, as shown in the next section.

3.3 Model Governing Equations

The combustion within a chamber would be modeled using OpenFOAM code in the current numerical investigation. XiFoam solver will be used to solve the pertinent governing equations utilizing FVM (Finite Volume Method) with various discretization methods. Due to the inclusion of Multiphysics issues in the simulation modeling, the combustion numerical model is extremely complex. In addition, modeling reactions involving multiple species increases the number of relevant equations that must be solved. In addition, the turbulence model increases the complexity of the modeled problem.

There are fundamental governing equations for fluid flow problems that must be implemented in the model first. To the main governing equations, such as the combustion and/or radiation sources, any additional model specifications can be added as a source or sink. Alternatively, scalar transport additives can be added as a distinct governing equation, such as the energy equation, multispecies equation, or turbulence model. All governing equations associated with numerical modeling are described in detail in the current section.

3.3.1 Mass conservation equation (continuity equation)

The equation for mass conservation, also known as the continuity equation, the mass conservation equation is derived from the fundamental, well-known form of the continuity equation, which is written as (la Cruz-Ávila et al., 2020; Li et al., 2017; Paulasalo, 2019):

$$\frac{\partial \bar{\rho}}{\partial t} + \frac{\partial(\bar{\rho}\tilde{u}_j)}{\partial x_j} = 0 \quad (3.1)$$

3.3.2 Momentum equation

The momentum equation, or what Navier-Stock named it, the definition of an equation is the equation that describes the flow characteristics (velocity and pressure) in all flow directions. Generally speaking, the final form of Navier-Stock's The x and y direction equation is:

$$\begin{aligned} \frac{\partial(\bar{\rho}\tilde{u}_i)}{\partial t} + \frac{\partial(\bar{\rho}\tilde{u}_i\tilde{u}_j)}{\partial x_j} \\ = \frac{\partial \bar{\rho}}{\partial x_j} + \frac{\partial}{\partial x_j} \left[\mu \left(\frac{\partial \tilde{u}_i}{\partial x_j} + \frac{\partial \tilde{u}_j}{\partial x_i} - \left(\frac{2}{3} \delta_{ij} \frac{\partial \tilde{u}_k}{\partial x_k} \right) \right) - \overline{p\tilde{u}_i\tilde{u}_j} \right] \end{aligned} \quad (3.2)$$

Where u_i and δ_{xi} represent the velocity component and spatial distance in the flow direction, u_j and δ_{xj} represent the velocity component and spatial distance in the other directions, p represents the pressure, and δ_{ij} is the Kronecher Delta, the mixture density that can be determined using the ideal gas law:

$$PV = mRT \rightarrow \rho_{mixture} = \frac{P}{RT} \quad (3.3)$$

$$R = \frac{R_0}{M_{ave}}$$

$$M_{ave} = \frac{1}{\sum Y_s M_s}$$

Where R_0 is the constant for all gases. M_{ave} is the average molar mass of the mixture (Paulasalo, 2019), where Y_s and M_s are the mass fraction and molar mass for each chemical species, respectively, where the subscript s refers to the chemical species, and T is the temperature of the gas.

Sutherland's law is used to calculate the gas dynamic viscosity as a function of temperature T in the present transport model (Greenshields, 2020):

$$\mu = A_s \frac{\sqrt{T}}{T + T_s}$$

Where A_s is the Sutherland coefficient and T_s is the Sutherland temperature; both are species constants.

3.3.3 Energy transport equation

The temperature is the most influential property in the combustion model's reactions. To calculate the temperature, the energy transport equation, also known as the energy conservation equation, must be implemented in the computational model. To include their effects in the final calculations, however, the combustion and radiation sources must be added to the energy transport equation. The energy conservation equation

that includes the effects of combustion and radiation is as follows (la Cruz-Ávila et al., 2020; Paulasalo, 2019):

$$\begin{aligned} \frac{\partial(\rho h)}{\partial t} + \frac{\partial(\rho h u_j)}{\partial x_j} \\ = \frac{\partial}{\partial x_j} \left\{ \frac{\mu}{Prh} \frac{\partial h}{\partial x_j} + \mu \left(\frac{1}{Scs} - \frac{1}{Prh} \right) \sum_s h_s \frac{\partial Y_s}{\partial x_j} \right\} + \frac{\partial P}{\partial t} + S_{rad.} \\ + S_{comb.} \end{aligned} \quad (3.4)$$

Prh and Scs represent the mixture Prandtl number and the species Schmidt number, respectively, and $S_{comb.}$ and $S_{rad.}$ are source variables added to the energy equation to account for combustion and radiation effects, where:

$$\begin{aligned} Pr_h &= \frac{\mu c \rho}{\lambda} \\ Sc_s &= \frac{\mu}{\rho D_s} \end{aligned}$$

Where λ and D_s represent the thermal conductivity of the mixture and the diffusion coefficient of the species, respectively.

The temperature of the field mixture is computed for each updated enthalpy value, as follows:

$$T = \frac{h - Y_{fuel} h_{fuel}}{c \bar{\rho}} \quad (3.5)$$

Y_{fuel} and h_{fuel} represent the fuel's mole fraction and enthalpy, respectively.

JANAF is the most popular thermophysical model for calculating the enthalpy of a mixture. JANAF calculates c_p as a function of temperature using coefficients extracted from JANAF thermodynamic tables. Two sets of coefficients are specified, the first for temperatures above T_c and the second for temperatures below T_c (Greenshields, 2021). The relationship between c_p and temperature is:

$$c_p = R \left(\left(\left((a_4 T + a_3) T + a_2 \right) T + a_1 \right) T + a_0 \right)$$

In addition, the high and low temperature constants of integration, a_5 and a_6 , are used to calculate h .

$$h = \sum_s Y_s h_s$$

$$h_s = h_s^0 + \int_{T_0}^T C_{p,s}(T) dT$$

Where $C_{p,s}$ is the species' specific heat at constant pressure and h_s is the species' enthalpy.

3.3.4 Species transport equation

In the present computational model, each chemical component in the flame combustion reaction is considered a single species, with each species' equation included as a scalar transport equation or a scalar conservation equation.

The species transport equations can be reduced to a single combustion progress variable equation (Kutkan & Guerrero, 2021) under the assumption of straightforward one-step chemistry.

$$\frac{\partial(\bar{\rho}\tilde{c})}{\partial t} + \frac{\partial(\bar{\rho}\tilde{u}_i\tilde{c})}{\partial x_i} = \frac{\partial}{\partial x_i} \left(\bar{\rho}\alpha + \frac{\mu_t}{\partial x_i} \frac{\partial \tilde{c}}{\partial x_i} \right) + \omega_c \quad (3.6)$$

Where t stands for tumultuous property and $\bar{\quad}$ and $\tilde{\quad}$ stand for Reynolds and Favre averaging, respectively. The transported quantity c represents the normalized mass proportion of the products, also known as the progress variable. The combustion progress variable defines the thermochemical state of the mixture (products and reactants) at any point in space and time. Any quantity, such as temperature or reactant mass fraction, can be used to establish a progress variable, so long as it is bounded by a single value in the reactants and another in the product (Ehsan, 2010).

$$c = \frac{T - T_r}{T_p - T_r}$$

Where r represents unburned reactant gas and p represents product gas.

A progress variable characterizes the combustion process ($c = 1$ in the burned product gas and $c = 0$ in the reactant gas). None of the existing combustion solvers in OpenFOAM are directly predicated on a progress variable (Povilaitis & Jaseliūnaitė, 2021). In OpenFOAM, flame front propagation is modeled by solving a transport equation for the regress variable b as opposed to the progress variable c , where $b = 0$ represents the products and $b = 1$ represents the reactants, and:

$$b = 1 - c \quad (3.7)$$

Consequently, Equation 3.6 can be expressed as follows in terms of

the regressive variable b :

$$\frac{\partial(\bar{\rho}\tilde{b})}{\partial t} + \frac{\partial(\bar{\rho}\tilde{u}_i\tilde{b})}{\partial x_i} = \frac{\partial}{\partial x_i} \left(\bar{\rho}\alpha + \frac{\mu_t}{sc_t} \frac{\partial\tilde{b}}{\partial x_i} \right) + \omega_c \quad (3.8)$$

Equation 3.8 is utilized by the OpenFOAM and XiFoam solvers in particular.

3.3.5 Turbulence modeling using the standard $k - \epsilon$ model

Most compressible fluid problems must be corrected by turbulence models in order to calculate fluid properties, particularly for combustion and chemical reaction models. RANS, or the Reynold-Averaged Navier Stock Equation, is the fundamental model. This model cannot account for the tiniest vortex ripples in the flow. In order to account for the intermediate vortex robbers in the flow, a new model known as LES (Large Eddy Simulation) was created. Nonetheless, LES filters cannot photograph the smallest robins. Thus, a newly developed model known as DNS (Direct Numerical Simulation) was constructed to capture the system's smallest vortex. DNS requires a large amount of computing resources in addition to the complexity of applying the DNS model to a complex domain.

In the present numerical work, the standard $k - \epsilon$ turbulence model was used to implement the RANS turbulence model. In this model, two essential parameters are taken into account for the calculations: k , or turbulent kinetic energy, which is the measure of turbulence production. The other crucial parameter in this model is the dissipation rate, denoted by the symbol ϵ . This parameter represents the energy loss due to turbulence.

This section describes the processes necessary to develop the standard $k - \epsilon$ turbulence model within the current computational model. The

initial step is determined by averaging each parameter in the Navier-Stock equation over time, with each parameter separated into two parts: the time-averaged term and the fluctuating term, as shown below (Chengeng & Mikhail, 2023):

$$u = \bar{u} + \acute{u}, \text{ where } \bar{u} = \lim_{T \rightarrow \infty} \frac{1}{T} \int_0^T u(x, t) dt$$

Where \bar{u} denotes the time-averaged term, whereas \acute{u} denotes the fluctuating term. However, because the fluid is compressible, density change must be taken into account by simplifying the transport equation as shown below:

$$u = \tilde{u} + \acute{u}, \text{ where } \tilde{u} = \frac{\overline{\rho u}}{\bar{\rho}}$$

Favre-Averaging employs this technique when the density change is taken into consideration. This method applies to the other flow, pressure, density, species, and temperature parameters. Now, by applying Favre-Averaging to the preceding governing equations, they would be reformulated as follows (Rusdin, 2017):

1) Equation for Averaged Continuity:

$$\frac{\partial \bar{\rho}}{\partial t} + \frac{\partial (\bar{\rho} \tilde{u}_j)}{\partial x_j} = 0 \quad (3.9)$$

2) Momentum Average Equation:

$$\begin{aligned} \frac{\partial(\bar{\rho}\tilde{u}_i)}{\partial t} + \frac{\partial(\bar{\rho}\tilde{u}_i\tilde{u}_j)}{\partial x_j} \\ = \frac{\partial\bar{P}}{\partial x_i} + \frac{\partial}{\partial x_j} \left[\mu \left(\frac{\partial\tilde{u}_i}{\partial x_j} + \frac{\partial\tilde{u}_j}{\partial x_i} - \left(\frac{2}{3} \delta_{ij} \frac{\partial\tilde{u}_k}{\partial x_k} \right) \right) - \overline{\rho\tilde{u}_i\tilde{u}_j} \right] \end{aligned} \quad (3.10)$$

Where $-\overline{\rho\tilde{u}_i\tilde{u}_j}$ Reynold stresses, which can be modeled using the so-called Boussinesq Eddy viscosity model, refer to a parameter.

$$-\overline{\rho\tilde{u}_i\tilde{u}_j} = \mu_t \left(\frac{\partial\tilde{u}_i}{\partial x_j} + \frac{\partial\tilde{u}_j}{\partial x_i} - \left(\frac{2}{3} \delta_{ij} \frac{\partial\tilde{u}_k}{\partial x_k} \right) \right) - \left(\frac{2}{3} \bar{\rho}\tilde{k}\delta_{ij} \right) \quad (3.11)$$

Where k represents the kinetic energy of turbulent motion and μ_t is the eddy viscosity. μ_t can be computed as follows:

$$\mu_t = \frac{C_\mu \bar{\rho} \tilde{k}^2}{\tilde{\epsilon}}$$

Where $\tilde{\epsilon}$ is the dissipation rate while C_μ is a constant. k and ϵ are scalars that can be evaluated using a particular scalar transport equation or a scalar conservation equation, as shown below:

The transport equation is derived for k as follows (Han & Reitz, 1995):

$$\frac{\partial(\bar{\rho}\tilde{k})}{\partial t} + \frac{\partial(\bar{\rho}\tilde{k}\tilde{u}_j)}{\partial x_j} = \frac{\partial}{\partial x_j} \left[\mu + \frac{\mu_t}{Pr_k^t} \left(\frac{\partial k}{\partial x_j} \right) \right] + P - \bar{\rho}\tilde{\epsilon} \quad (3.12)$$

While the derived transport equation for ϵ is:

$$\begin{aligned}
& \frac{\partial(\bar{\rho}\tilde{\epsilon})}{\partial t} + \frac{\partial(\bar{\rho}\tilde{\epsilon}\tilde{u}_j)}{\partial x_j} \\
& = \frac{\partial}{\partial x_j} \left[\mu + \frac{\mu_t}{Pr_\epsilon^t} \left(\frac{\partial \tilde{\epsilon}}{\partial x_j} \right) \right] + \frac{\tilde{\epsilon}}{k} (C_{\epsilon 1} G - C_{\epsilon 2} \bar{\rho} \tilde{\epsilon}) \\
& - \left(\frac{2}{3} C_{\epsilon 1} + C_{\epsilon 3} \right) \bar{\rho} \tilde{\epsilon} \frac{\partial \tilde{u}_k}{x_k}
\end{aligned} \tag{3.13}$$

P is the turbulent kinetic energy production rate, which can be calculated as follows (Krastev et al., 2017):

$$P = G - \frac{2}{3} \bar{\rho} \tilde{K} \frac{\partial \tilde{u}_k}{x_k} \tag{3.14}$$

$$G = 2\mu_t \left(S_{ij} S_{ij} - \frac{1}{3} \left[\frac{\partial \tilde{u}_k}{x_k} \right]^2 \right) \tag{3.15}$$

$$S_{ij} = \frac{1}{2} \left(\frac{\partial U_i}{\partial x_j} + \frac{\partial U_j}{\partial x_i} \right) \tag{3.16}$$

Pr_k^t and Pr_ϵ^t represent the turbulent Prandtl number for k and, while $C_{\epsilon 1}$, $C_{\epsilon 2}$, C_μ , and $C_{\epsilon 3}$ are the model constants. All of these constants have already been computed as shown below (Krastev et al., 2017):

$$\begin{array}{lll}
Pr_k^t = 1 & Pr_\epsilon^t = 1.3 & C_\mu = 0.09, \\
C_{\epsilon 1} = 1.44 & C_{\epsilon 2} = 1 & C_{\epsilon 3} = -0.33
\end{array}$$

3.3.6 Combustion model

In the majority of problems involving flame propagation, the reaction rate is governed by the turbulent time scale for each species rather than the reaction time scale. Eddy dissipation is the name for such a model that

regulates the combustion rate. Model (EDM). Spalding (Spalding, 1971) created the original model, from which the aforementioned model was derived. The "Eddy-Break-Up" (EBU) model, developed by Spalding (Spalding, 1971) and referred to as the "Eddy-Break-Up" (EBU) model, was initially used to calculate the reaction rate of the premixed turbulent flame and states:

$$\overline{\omega}_f = -C_{EBU} \frac{\sqrt{\overline{Y_f''^2}}}{\tau_f} \quad (3.17)$$

Where $\overline{\omega}_f$ is the reaction rate or combustion rate, C_{EBU} is the model coefficient, and $\overline{Y_f''^2}$ is the mixture fraction variance. τ_f represents the characteristic turbulent time, which is equal to:

$$\tau_f = \frac{\tilde{k}}{\tilde{\epsilon}}$$

Later, Magnussen and Hjertager (Magnussen & Hjertager, 1977) developed the Eddy Dissipation Model (EDM) by introducing a new model in which the variance of the mixture fraction ($\overline{Y_f''^2}$) is replaced by the mass fraction of the deficient species, which represents the fuel for the lean mixture and the oxidizer for the rich mixture.

Consequently, the eddy dissipation model can be modified as follows:

$$\overline{\omega}_f = -C_{EBU} \frac{\min \left\{ \tilde{Y}_f, \frac{\bar{Y}_0}{S}, \frac{\bar{Y}_\rho}{1+S} \right\}}{\tau_f} \quad (3.18)$$

\bar{Y}_f , \bar{Y}_0 , and \bar{Y}_p are fuel, oxidizer, and product, respectively. While s represents the stoichiometric mass ratio of oxidizer to fuel, (Favre-Averaged Mass Fractions) are the average mass fractions of Favre.

To calculate the reaction rate for any particular species, use the following equation:

$$\tilde{\omega}_s = -\frac{\gamma^2}{1-\gamma^2} \frac{\rho(\tilde{Y}_s - \tilde{Y}_s^*)}{\tau^*} \quad (3.19)$$

Where \tilde{Y}_s and \tilde{Y}_s^* represent the species mass fraction computed from the species transport equation and the species fraction calculated chemically, respectively. The overbar $\bar{\quad}$ and tilde $\tilde{\quad}$ refer to the Reynolds and Favre averaging's, respectively.

$$\tau^* = 0.4083 \sqrt{\frac{\nu}{\tilde{\epsilon}}}$$

Where ν is the kinematic viscosity.

$$\gamma = 2.1377 \left(\frac{\nu \tilde{\epsilon}}{k^2} \right)^{\frac{1}{2}}$$

3.3.7 Radiation model

The energy transport equation (Equation 3.4) contains two source terms: combustion and radiation (S_{rad}). The radiation term is derived from the calculation of the net radiation heat flux ($\nabla \cdot \bar{q}_R$), where:

$$\nabla \cdot \bar{q}_R = \int_{4\pi}^1 \nabla \cdot (\hat{s}I) d\Omega \quad (3.20)$$

\hat{S} is the propagation direction of the radiation beams, while I and Ω are the spectral intensity and the spherical solid angle, respectively. One of the assumptions of the present computational model is that the medium is gray, so that $\nabla \cdot (\hat{S}I)$ can be integrated along the radiation wavelength λ as below (Viskanta & Mengüç, 1987):

$$\int_{\lambda} \nabla \cdot (\hat{S}I) d\lambda = k_p \int_{\lambda} (I_{p\lambda} - I_{\lambda}) d\lambda = \nabla \cdot (\hat{S}I) = k_p(I_p - I) \quad (3.21)$$

By substituting Equation 3.21 in Equation 3.20, it is found that:

$$\nabla \cdot \bar{q}R = \int_{4\pi} \nabla \cdot (\hat{S}I) d\Omega = k_p 4\pi I_p - k_p \int_{4\pi} I d\Omega = k_p(4\sigma T^4 - G) \quad (3.22)$$

The spectral absorption coefficient is denoted by k_p . The terms $(4\sigma T^4)$ and G represent the rate of energy resealing per unit area and the total irradiance received from domain directions, respectively. σ is the Stefan-Boltzmann constant, which equals $5.67 \times 10^{-8} \text{ W/m}^2\text{K}$. Equations 3.21 and 3.22 represent the Radiative Transfer Equation (RTE), which determines the rate of spectral radiation in a particular medium.

There are two methods for solving the above-derived RTE: first, the PI-approximation method, in which the incident irradiance is calculated using spherical harmonics. As a solution to the radiative transfer equation (RTE), the Finite Volume Discrete Ordinates Method (fvDOM) is implemented in the current computational model. This method divides the irradiation field into a predetermined number of solid angles. The intensity of irradiation (I_i) would then be calculated for each solid angle (Ω_i) in each direction. Finally, the net radiation G can be calculated by numerically integrating the predicted irradiance intensities along the

solid angle, as shown below (Ilbas, 2005):

$$G = \int_{4\pi} (I) d\Omega \approx \sum I_i i. \Delta\Omega$$

K_p can be determined by weighting the individual K_p values for each species i at each partial pressure, as shown below (Gamil et al., 2020):

$$k_p = \sum_{i=1} k_{p,i} \cdot p_i, p_i = \frac{M\tilde{Y}}{M} \bar{p}$$

3.4 Methods for Predicting Required Values

In this section, the procedure for the prediction and determination of flame front propagation as well as the mole fraction for the reactant and products are illustrated. After completing the required simulation process for a particular fuel/air mixture under certain conditions, some computational and post-processing steps are performed as described below.

3.4.1 Flame front propagation prediction

As mentioned previously, the solver which is used is supplied with a model for predicting the energy as well as the temperature at each cell across the computational domain. After getting the temperature contour for a specific case, the temperature distribution is plotted over the computational domain's center line. Mjbel and Liberman (Liberman et al., 2009; Mjbel et al., 2021), reported that the flame front propagation was located at the point of peak temperature on the center line. This methodology has shown good results and a high matching with the experimental results of the current study, as will be presented in chapter five later.

3.4.2 Prediction of species mole fractions

As stated earlier, the XiFoam solver has its model for predicting the transportation of species at each cell across the computational domain. The mole fraction for the species is calculated through a post-calculation for the regress variable b and progress variable c according to the chemical reaction balance. The regress variable b has been used to trace the reactants while the progress variable c has been used to trace the products.

3.5 Mesh Generation and Mesh Convergence Study

OpenFOAM code has its tool for mesh generation called “blockMesh” where all the vertices that govern the domain are constructed to create the domain mesh blocks and boundaries. All these details are written as code in a journal file called “blockMeshDict”. However, in the current study, the whole geometrical domain of the studied control volume was constructed from structured mesh with hexa-blocks using the abovementioned tool. Thus, a uniform structured mesh was generated using different blocks as shown in Figure 3.1. there are different mesh sizes tested to investigate the sensitivity of the calculated variables to the change in mesh sizes. different mesh sizes were investigated so the value would not be changed, or if the change is not significant when the mesh size increases. Five mesh sizes are set in the simulations to perform the mesh convergence study and approach the mesh independence, namely, 20000 cells (coarse mesh), 25000 cells (medium mesh), 30000 cells (fine mesh), 36000 cells (finer mesh size) and 64000 (more fine mesh size) are tested the list of meshes is shown in Table 3.1. it can be said that the numerical domain starts to be mesh-independent at the fine mesh size (64000 cells). Thus, all numeric data and cases done in the presented study were investigated under

fine mesh size cases.

Table 3.1: Meshing details

Mesh number	Mesh size	Number of nodes	Number of elements	Type of mesh
1	500×40×1	42168	20000	Structure grid
2	500×50×1	52208	25000	Structure grid
3	600×50×1	62608	30000	Structure grid
4	600×60×1	74648	36000	Structure grid
5	800×80×1	131528	64000	Structure grid

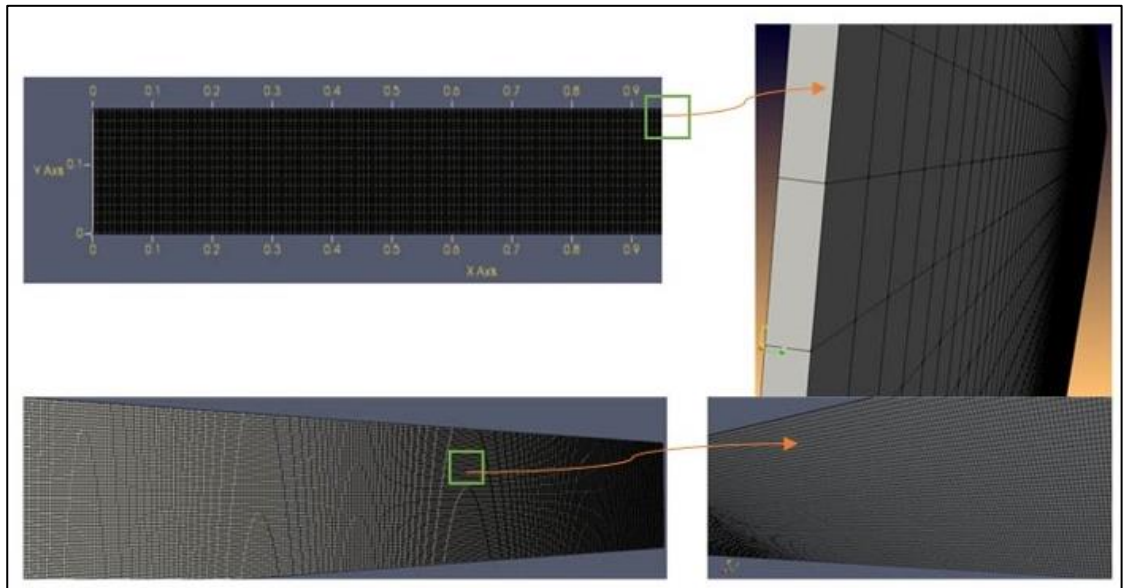


Figure 3.1: Combustor mesh generation

Figure 3.2 demonstrates the temperature distribution along the center line above the flame tip position at the abovementioned five mesh sizes. All are for the stoichiometric LPG/air mixture combination. It's worth mentioning that the difference in temperature values between the different mesh sizes appears in the figure to be greater than it is in reality since the figure is zoomed to be able to notice the difference, otherwise, the difference in the values is slight, especially between the fine and the very-fine mesh. The figure also shows that the temperature distribution approaches its mesh independency at the very-fine mesh size where the

curve in the very-fine mesh size matches the curve in the fine mesh size concluding that any further increase in the mesh would not affect the results significantly. Accordingly, the fine mesh size has been chosen for all the simulations of the present work.

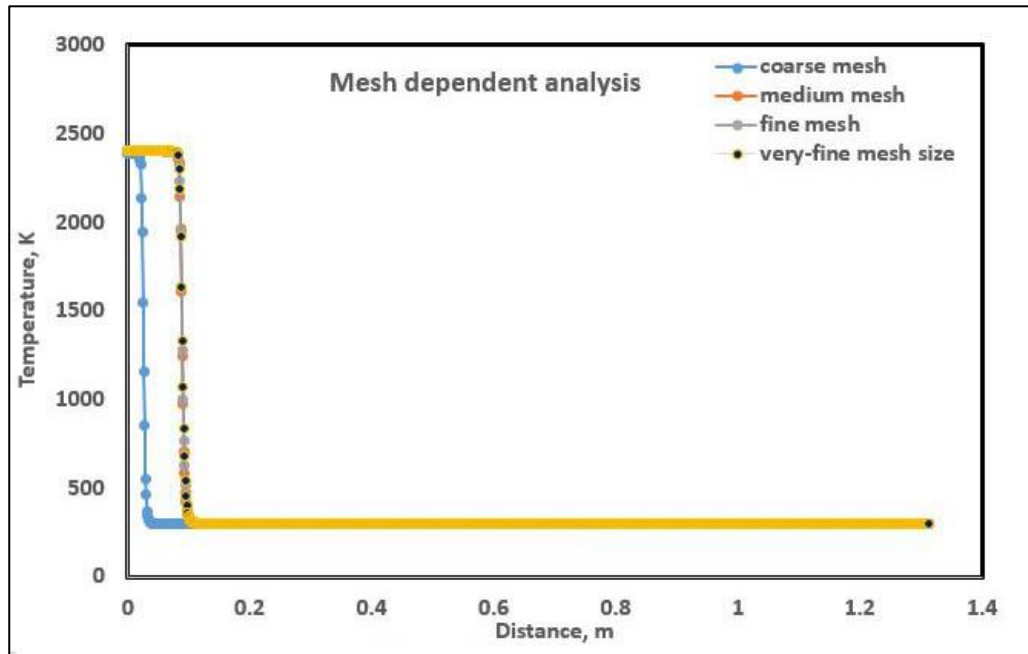


Figure 3.2: Temperature distributions along center line at different mesh sizes

3.6 Boundary Conditions and Initial conditions

There are different types of boundary conditions used in the current computational model. Generally, the boundary conditions in the current numerical simulation are divided into four categories; boundary conditions involved in the turbulence model parameters, boundary conditions involved in the species of the chemical reaction, boundary conditions related to the energy transport parameters, and finally, the conditions involve the momentum equation parameters. Figure 3.3 shows the physical domain, whereas Figure 3.3 A, illustrates the domain pointer to it and the boundary conditions corresponding to each region. These boundary conditions were used for the solution of the problem through the discretization of the partial

differential equations of the abovementioned model governing equations. Figure 3.3 B show the regions of the physical domain. Table 3.2 shows all these boundary conditions for each patch under each of the aforementioned categories.

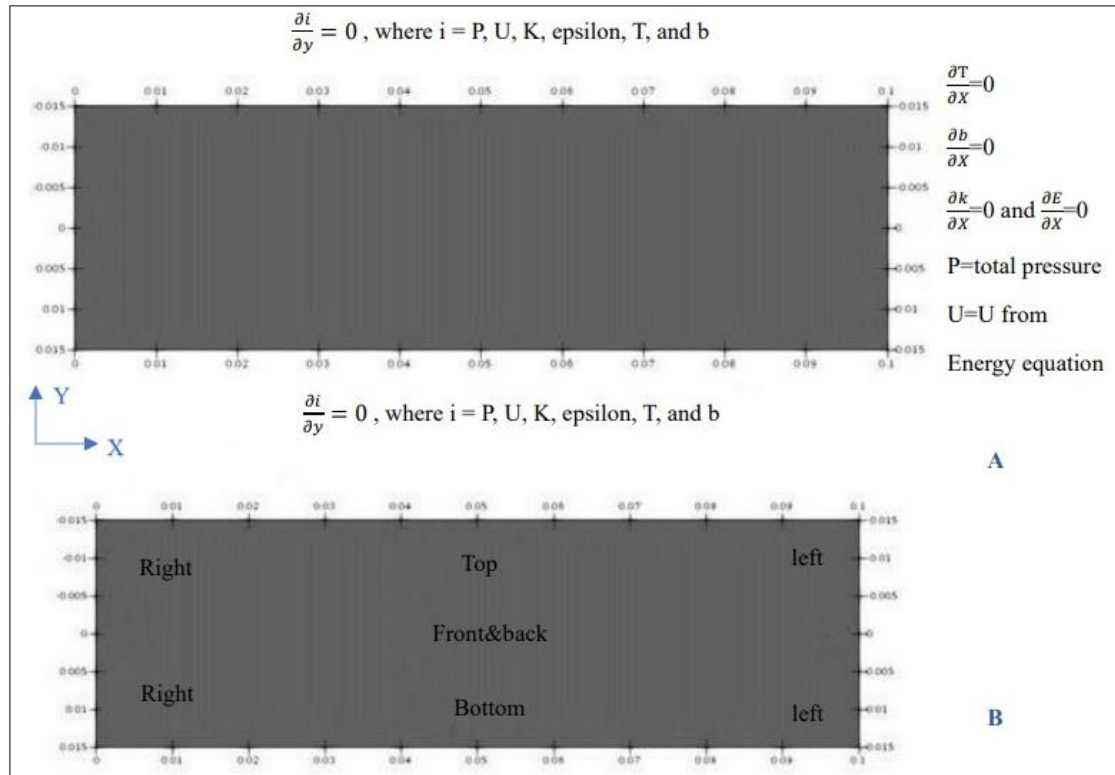


Figure 3.3: The physical domain and its Boundary conditions: A) types of Boundary conditions, B) regions of the domain

Table 3.2: Boundary conditions specifications for main properties under each category of the gov. Eq.

Turbulence Model Parameters					
	Front and back	Left	Right	Bottom	Top
ϵ	Empty	Symmetry Plane	Symmetry Plane	Symmetry plane	Symmetry plane

Turbulence Model Parameters					
k	Empty	Symmetry Plane	Symmetry Plane	Symmetry plane	Symmetry plane
nut	Empty	Symmetry Plane	Symmetry Plane	Symmetry plane	Symmetry plane
Momentum and Continuity Parameters					
u	Empty	Symmetry Plane	Symmetry Plane	Symmetry plane	Symmetry plane
p	Empty	Symmetry Plane	Symmetry Plane	Symmetry plane	Symmetry plane
Energy Equation Parameters					
Alphat	Empty	Symmetry Plane	Symmetry Plane	Symmetry plane	Symmetry plane
T	Empty	Symmetry Plane	Symmetry Plane	Symmetry plane	Symmetry plane
Energy Equation Parameters					
b	Empty	Symmetry Plane	Symmetry Plane	Symmetry plane	Symmetry plane

Where alphat is the turbulent thermal diffusivity and nut is the turbulent kinematic viscosity.

The initial conditions are found in /0 directory. Table 3.3 presents the initial conditions. Since there is no ignition at time = 0, we have $b=1$ and $X_i = 1$ in the whole domain.

Table 3.3: Initial conditions

Variable	Description	Initial condition
alphat	Turbulence thermal diffusivity [kg/m/s]	InternalField uniform 0
b	Regress variable (dimensionless)	InternalField uniform 1
epsilon	The turbulence kinetic energy dissipation rate [m ² /s ³]	InternalField uniform 375
k	The turbulence kinetic energy [m ² /s ²]	InternalField uniform 1.5
mut	The turbulence viscosity [kg/m/s]	InternalField uniform 0
p	Pressure [kg/m/s ²]	InternalField uniform 100000
S_u	Laminar flame speed [m/s]	InternalField uniform 0.43

Variable	Description	Initial condition
T	Temperature [K]	InternalField uniform 300
T_u	Unburnt temperature [K]	Internal Field uniform 300
U	Velocity field [m/s]	Internal Field uniform (0 0 0)
Xi	The flame wrinkling S_t/S_u (dimensionless)	Internal Field uniform 1

CHAPTER FOUR
EXPERIMENTAL SET UP

CHAPTER FOUR

EXPERIMENTAL SETUP

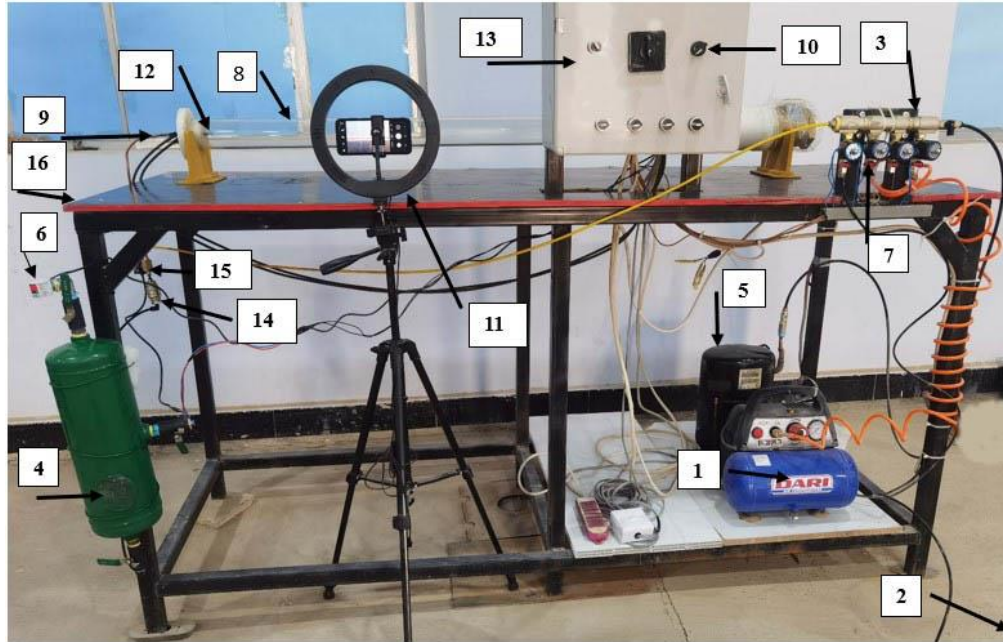
4.1 Introduction

This chapter describes an experimental setup developed to investigate flame structure and propagation speed at Al-Furat Al-Awsat Technical University, Technical Engineering College, Najaf. The setup includes a combustion chamber, ignition unit, fuel injection and control unit, mixture preparation unit, and flame imaging unit. The chapter explains each component in detail, along with the test technique, calibration techniques, and image processing approach used to determine flame velocity. The chapter also discusses the possible causes of error in the experimental configuration and emphasizes the significance of replicability in the experiments.

4.2 The Experimental Apparatus's General Description

The study of the flame structure and flame propagation speed needs to be accurate because of the short period available for measurement, which is not longer than a few milliseconds. A new experimental facility is designed and constructed in Al-Furat Al-Awsat Technical University, Technical Engineering College, Najaf. Mechanical engineering techniques of power to measure the flame speed and flame structure of a partially premixed complete setup of the rig consisting of the parts, as shown in Figures 4.1 and 4.2.

All parts will be classified into units; each unit, including its role in experimental tests, its devices, components, and their specifications, will be detailed in sequence in the following sections of this chapter.



1	Air Compressor	9	tube
2	LPG fuel cylinder	10	Ignitor Control Circuit
3	Mixture Preparation Control Unit	11	Stand for the camera
4	Mixer	12	two electrodes
5	Vacuum Pump	13	Electrical control board unit.
6	Digital Pressure.	14	reverse flame check valve.
7	pressure gage valve	15	the Solenoid Valve
8	Combustion chamber	16	vacuum pressure gage

Figure 4.1: Photograph of the experimental apparatus used in the study

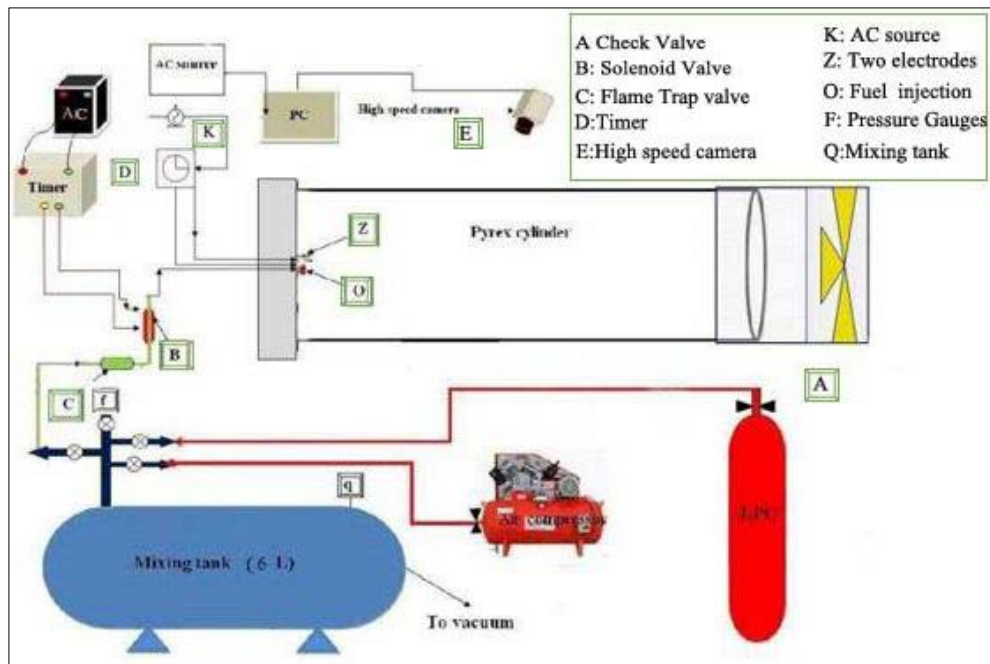


Figure 4.2: Schematic sketch of the experimental rig

4.3 Combustion Chamber Unit

The main unit of the experimental rig is the combustion chamber, shown in Figure 4.3. This unit comprises the glass cylinder, the fuel injection tube, the Teflon flange, the spark ignition combination, and the brass swing check valve. Other parts related to measurements and safe operation are linked to the combustion chamber and connected with it; these parts are discussed and illustrated later.

4.3.1 The glass cylinder

The present work used a cylindrical combustion chamber that is heat-resistant up to (1000 C), a Pyrex cylinder with a (71 mm) inner diameter, a (76 mm) outer diameter, a (5 mm) wall thickness, and a (1500 mm). The cylinder is installed horizontally and supported by two wood pieces fixed to a metal table, as shown in Figure 4.3.



Figure 4.3: Photograph of the combustion chamber unit

4.3.2 The Teflon flange

This flange is used to close one end of the Pyrex cylinder (combustion chamber) and to install all other accessories (see Figure 4.4) which are:

- 1) Fuel supply injection
- 2) Spark ignition (electrode tips)

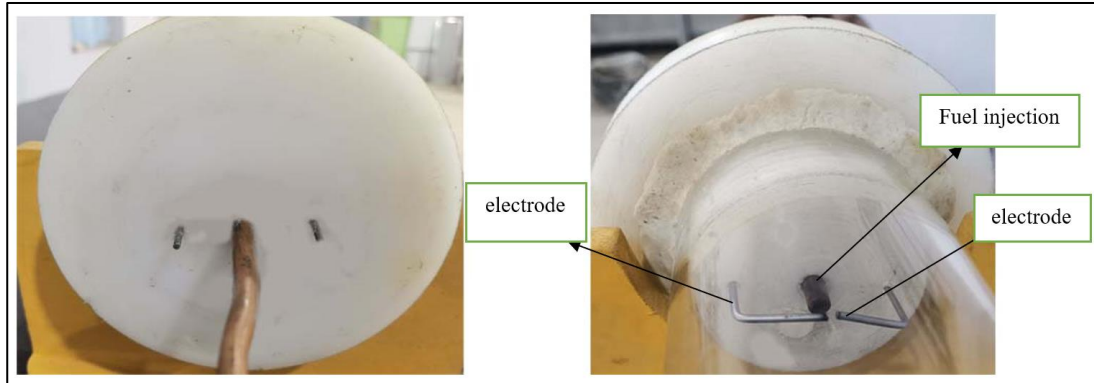


Figure 4.4: The Teflon flange

4.3.3 Brass swing check valve

It is a one-way valve that works to close the combustion chamber from the open side, as it helps to empty the contents of the combustion chamber between tests using a vacuum pump, as it opens at the start of the test, thus helping the flame to exit through it as shown in Figure 4.5.



Figure 4.5: Brass swing check valve

4.4 Ignition Circuit and Control Unit

An electrical circuit is built and used to provide the necessary power to the two electrodes, facilitating the generation of a powerful spark that is crucial for initiating the mixture. Furthermore, this circuit is accountable for controlling the time and magnitude of the supplied electricity. The ignition

system consists of a 220 V AC electrical circuit. Connect it to a dedicated timer to control the ignition timing source that supplies power to a rotary variable transformer, which generates the required voltage for ignition. The output is coupled to an ignition burner transformer, which has a maximum voltage of 15 kV. This transformer delivers high tension voltage to the two electrodes, resulting in the generation of a forceful spark as needed. Diminutive stainless-steel electrodes, with a diameter of 1.5 mm, were inserted into the chamber to limit their influence on the spread of the flame. A self-igniting coil was used to begin the discharge. A spark is generated inside the combustion chamber by using two electrodes that are positioned in direct opposition to each other and aligned in a linear configuration. To intensify the electric field at the gap, the spark gap is adjusted to a consistent distance of 1 mm and the tips of the electrodes are sharpened. Consult Figures 4.6.

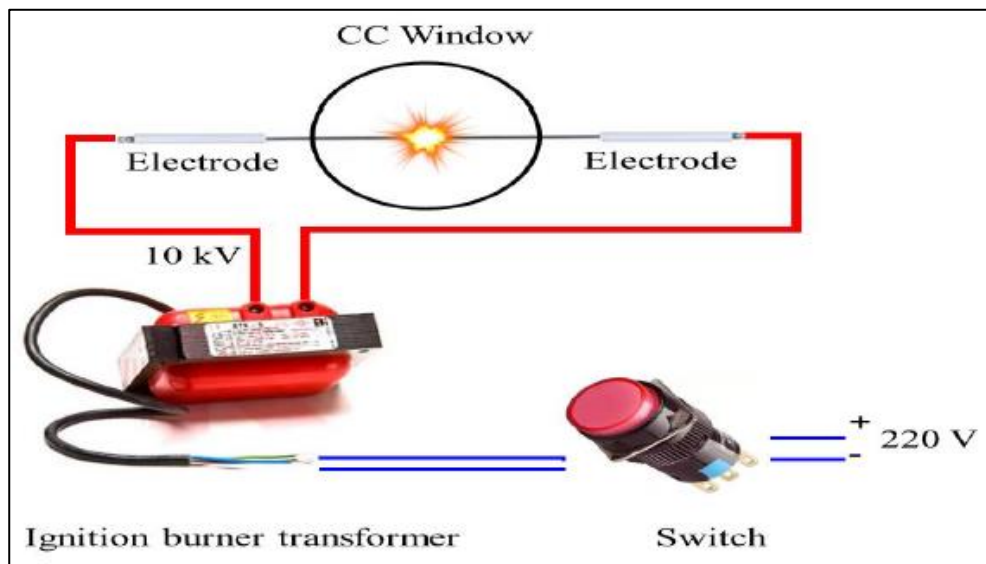


Figure 4.6: Schematic diagram of an electronic circuit for the ignition unit

4.5 Fuel Supply Control Unit

The Fuel Supply Control Unit (FSCU) is an essential component in the fuel delivery system of various types of experimental devices. Its primary function is to regulate and control the flow of fuel from the fuel source to the combustion chamber, ensuring optimal performance and efficiency. It consists of a gas injection unit and an electrical control unit.

4.5.1 Gas injection unit

A gas injection unit is a component used in a fuel supply control unit. It is designed to introduce gas, often in the form of bubbles or fine bubbles. Here's an explanation of how a typical gas injection unit works and its components:

4.5.1.1 The manifold

The experimental setup has a meticulously built manifold system in the combustion chamber, which facilitates the intake of fuel and oxidizer. This system is provided with a range of valves that enable accurate control and delivery of the substances. The configuration of the manifold is as follows:

- The Ball valve, with a diameter of 1/4 inch, is linked to a vacuum pump. Ball valves are renowned for their dependability and capacity to provide a tight seal. The 1/4-inch specification denotes the dimensions of the valve, signifying its capability to accommodate the necessary flow rates for the experiment.
- The needle valve control (1/4 inch) is directly connected to the combustion chamber and provides precise control over the intake of gases into the chamber. The design of the needle valve is specifically tailored for accurate control of fluid flow, a crucial need in

combustion research.

The system has four solenoid valves, each functioning on 24 V DC power derived from a 220 V AC source. Solenoid valves provide benefits in automated systems owing to their rapid and dependable functioning. One of these valves is linked to the air compressor, which provides air to the combustion chamber. The remaining three are connected to the ILPG (Liquefied Petroleum Gas) storage tanks, with one functioning as a backup. The valves provide accurate and electronic regulation of the injection of air and gaseous fuel into the system, which is crucial for attaining the intended experimental conditions, see Figure 4.7.



Figure 4.7: The gas manifolds

4.5.1.2 Pressure regulator

Furthermore, apart from the pressure regulators already in place on the LPG and AIR cylinders, an additional pressure regulator, seen in Figure 4.8, namely the Electric RA2000 model, has been put on the pipeline responsible for transporting the fuel/air mixture from the mixer to the burner tube. This regulator has a range of 0 to 10 bar. The purpose of this pressure regulator is to regulate the pressure of the mixture prior to its

passage through the rotameters. The pressure of the fuel/air combination flowing through the burner is maintained at a constant value of 1 bar throughout all experiments.



Figure 4.8: Pressure regulator of the mixture

4.5.1.3 Air compressor

A compressor (type DARI, 1.5 HP, 8 bar) supplies the air for the combustion chamber at the requisite pressure, as shown in Figure 4.9.



Figure 4.9: Air compressor

4.5.1.4 Vacuum system

The contents of the combustion chamber were removed during experiments using a vacuum pump at a constant rate of $0.3 \text{ m}^3/\text{h}$. Its purpose is to link the vacuum pump to the injection system of the combustion chamber, therefore minimizing the number of connections and potential regions of leakage. Following each test, the air compressor is used to cleanse the combustion chamber of its combustion byproducts.

4.5.1.5 Electrical control board unit

The electrical board measures $40 \times 30 \times 15 \text{ cm}$ and contains the components shown in Figure 4.10.

- The selector switch is responsible for providing electrical power to the board.
- The vacuum selection switch is a mechanism used to activate the vacuum compressor.
- The fuel selector switch consisted of two switches used to control the solenoid valves for gaseous fuels, with one switch serving as a backup.
- The fuel quantity regulation mechanism includes the management of a timer, which in turn directs the functioning of the One-Way electronic valve to regulate the flow of fuel into the combustion chamber.

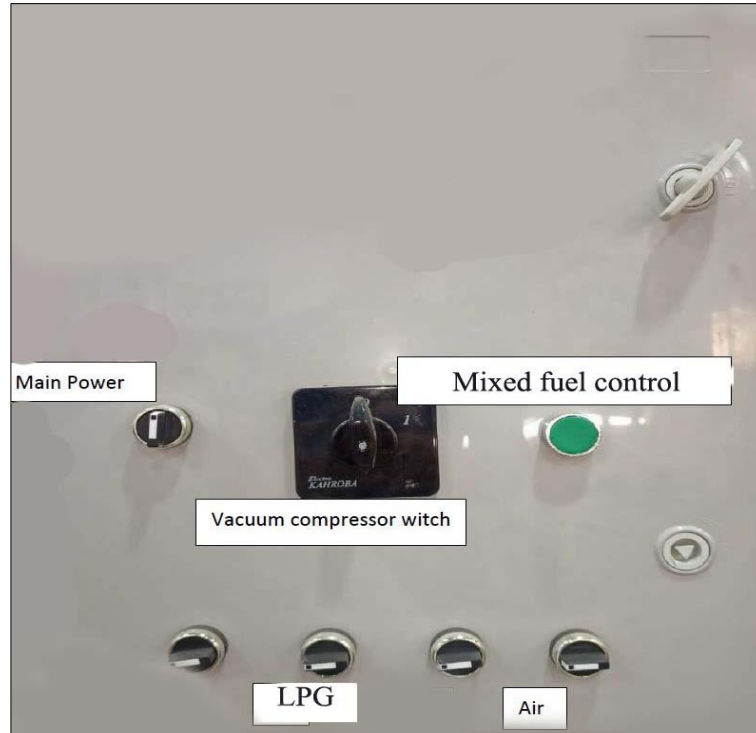


Figure 4.10: Electrical control board unit

4.6 Mixture Preparing Unit

The mixture (LPG-Air) preparation unit consists of the following component.

4.6.1 Mixing tank

The mixer is an aluminum tank with a cylindrical form. The mixer has dimensions of 550 *mm* in length, 120 *mm* in diameter, and 2 *mm* in thickness, resulting in a total capacity of 6 L. It has a pressure resistance above 12.5 bar. The mixing unit is equipped with three holes, each with a diameter of 19.05 *mm*, as seen in the schematic picture (4.11). One is used for creating a vacuum by applying pressure. The second aperture is used for delivering air and LPG to the blending apparatus. The same aperture allows the uniform amalgamation to enter the burner module. Every aperture is equipped with ball valves measuring 19.05 *mm* in diameter. The valves are undergoing a test where the internal pressure of the mixer is raised by about

8 bar to prevent any leakage. This is seen in Figure 4.11.

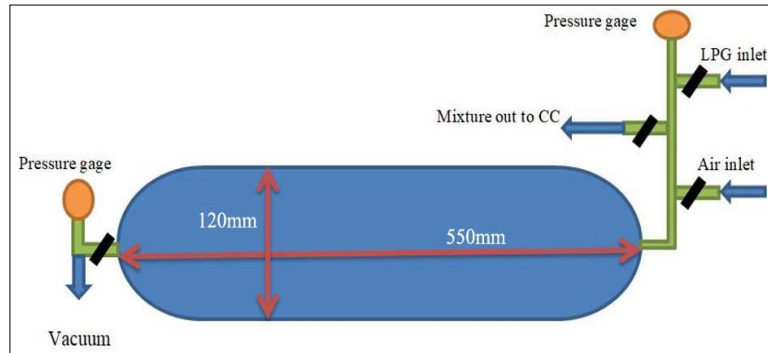


Figure 4.11: Schematic diagram of mixing tank

4.6.2 LPG fuel cylinder

The LPG fuel cylinder is a steel cylinder of weights 12.5 kg and capacity of 26.2 L provided with a regulator to control the quantity and pressure of the gas flow to the mixing tank

4.6.3 Pressure gauges

Two bourdon pressure gauges are used. The initial gauge is used to quantify the vacuum pressure inside the mixer, with a measurement range spanning from 0 to -1 bar. The second gauge is used to quantify the pressure of the concoction arranged within the mixer as shown in Appendix (B). The reading range extends from -1 to 4 bar, as seen in Figure 4.12 (a, b).

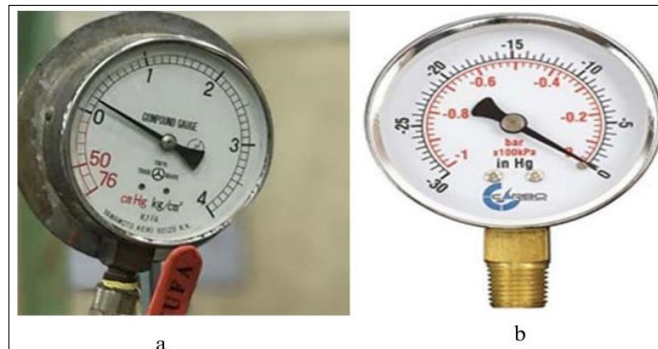


Figure 4.12: Pressure Gauges, a) Total pressure gage, b) vacuum pressure gage

4.6.4 Reverse flame check valve

The one-way Valve is a safety mechanism specifically intended to inhibit the flow of gas in the opposite direction, so effectively preventing the flame from reaching the fuel mixer. This mitigates the likelihood of an explosion or fire, hence enhancing the operational safety of the system. One-way valves are used in diverse systems. Ensuring their integrity is crucial for their continued optimal functioning. It is seen in Figure 4.13.

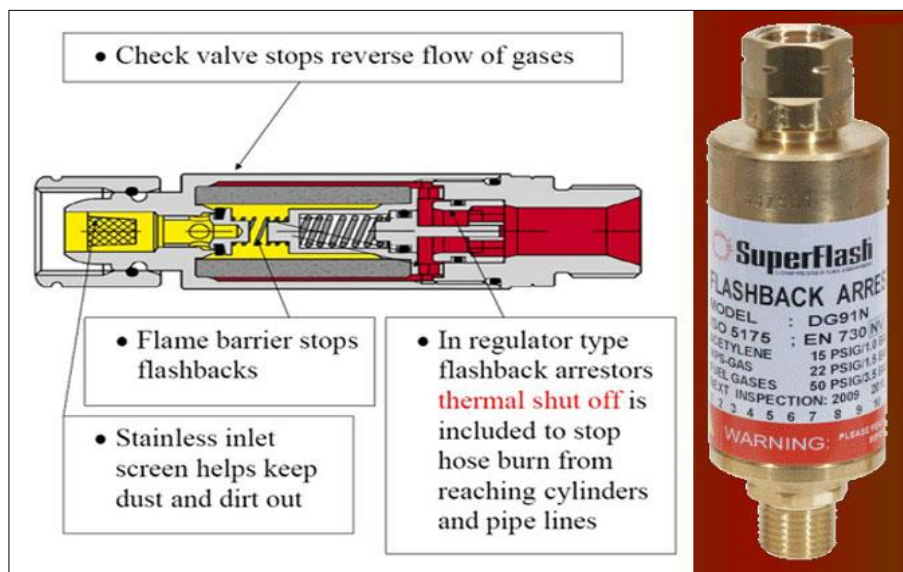


Figure 4.13: Schematic of reverse flame check valve

4.6.5 Solenoid valve

The solenoid valve is used to regulate the delivery of the LPG-air mixture to the combustion chamber. It is linked to the timer in order to regulate the supply of the mixture. The working pressure falls within the range of 0 to 25 bar. Furthermore, it functions as a unidirectional valve that obstructs the passage of gas in the opposite direction, thereby preventing the flame from reaching the fuel mixer as shown in Appendix (B). This serves to minimize the potential for explosion or fire. Figure 4.14 illustrate this.

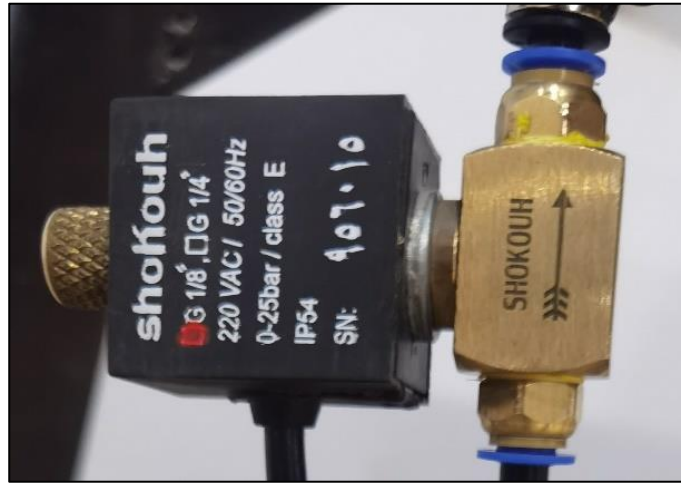


Figure 4.14: The solenoid valve

4.7 Flame Imaging Unit

An optical system is used to visualize and record the flame and flame propagation process with a high-speed camera. The flame imaging unit comprises a high-speed camera, a camera stand, and a light source.

4.7.1 The high-speed camera

The flame spread and its immediate beginning were captured and recorded using a high-resolution camera, namely the Huawei-P 40 pro, Figure 4.15, which has the capability of ultra-slow-motion. The gadget is equipped with a total of four cameras:

- The device is equipped with a 50-megapixel ultra-vision camera and a 40-megapixel ultra-wide cine-camera.
- The camera has a 12 MP optical super-sensing telephoto lens that supports focusing mode.
- A camera that uses Time of Flight (TOF) technology.

The picture resolution is capable of accommodating a maximum of 8192×6144 pixels. The video resolution is capable of supporting super slow-motion footage at 720 p with a frame rate of 7680 fps. It has the

capability to decelerate movement by a factor of 256. The camera has been mounted into a picture frame and is equipped with a Bluetooth remote control for initiating or terminating the process of shooting photos or videos.



Figure 4.15: High-speed camera: Huawei-P 40 with 7860 FPS

4.7.2 Light source

A 12V DC neon lamp is positioned within a sealed enclosure, with a single tiny aperture to concentrate the light onto the body of the combustion chamber. It is used to gather the light and then disperse it towards the camera. As a result, this light enhances the precision of flame photography. The lab is in complete darkness while recording since all lights are turned off.

4.8 Test Procedure

The mixing process relies on the Gibbs-Dalton Law, which calculates the partial pressure of each component in the mixture to get the precise equivalency ratio. The combination is prepared inside the dedicated mixing tank. The partial pressure of hydrocarbon fuels is often low. Therefore, using the mixer allows for the maximization of the partial pressure of the

fuel, therefore facilitating control over the admission process. The absolute pressure for each test is uniformly set at 5 bar, as per the specified technique as shown in Appendix (A).

A. Mixture preparation processes

- 1) Flushing Process of Mixer: This technique is accomplished by introducing air into the mixer for a duration of 3 to 5 minutes. The operation is iterated thrice to guarantee thorough purging of the mixer from any residual substances. The introduction of air is carried out under controlled pressure to prevent undesired increase in temperature.
- 2) Vacuum Process of Mixer: The vacuum procedure is initiated by shutting all valves except for the vacuum pump valve and the vacuum gauge valve. This allows the pump to effectively remove any residual contents from the mixer until its pressure reaches roughly (-0.92 bar).
- 3) Mixing Process
 - The LPG fuel is transferred from the LPG cylinder to the mixer. The partial pressure of the LPG fuel is directly proportional to its blend concentration. The LPG is introduced into the mixing tank first by opening the valve of the LPG cylinder and allowing the tank pressure to reach a certain amount.
 - Air is introduced into the system from the compressor until the pressure approaches atmospheric pressure. At this point, the valve on the vacuum gauge is closed, and the total pressure gauge is opened.
 - Additional air is introduced to achieve a total absolute pressure of 5 bar.
 - The mixture is allowed to stand for 10 minutes to achieve thorough homogenization.

B. Combustion chamber preparation and combustion processes.

- 1) After each reading, thoroughly clean the Pyrex cylinder (the combustion chamber) to remove any residue from the mixture. Allow the cylinder to cool down to room temperature, then introduce air into the cylinder and clean it using a cloth. Repeat this process multiple times to ensure that no traces of the mixture remain. The ignition time duration is set at 5 milliseconds.
- 2) The length of the fuel delivery is fixed at 10 seconds.
- 3) The uniform blend (LPG-air) is introduced into the combustion chamber at a low pressure.
- 4) Both the ignition and camera recording triggers are simultaneously activated.
- 5) Data is documented and images are captured.
- 6) Duplicated the same technique for subsequent readings.

4.9 Image Processing

The analysis of AVI files in this experiment is conducted by image processing utilizing the ProAnalyst program (Version 1.5.7.0). During the experiments, pictures are recorded at a high frame rate of 7680 frames per second, resulting in a time gap of 0.1 milliseconds each frame. The flame's position is established by analyzing the intensity of light, with the first white pixel indicating the site of ignition. The X-axis is positioned parallel to the tube's central axis, with the ignition electrode's tip serving as the reference point. The line tracking capability of the ProAnalyst software is used to accurately trace the motion of the illuminated leading edge of the flame. In grayscale photographs, each pixel is given a value ranging from 0 (representing a fully white cell) to 256 (representing a fully black cell). A pre-established threshold, such as 10, is used to classify the pixel values.

Pixels with values below this threshold are given a binary value of 0, while those with values above are allocated a binary value of 1, resulting in the creation of a binary matrix. The procedure entails quantifying the pixel count from the distal end of the tube to the leading edge of the flame. The computation of the distance between the ignition point and the flame front may be done by determining the total number of pixels that represent the full length of the tube. The conversion from pixels to millimeters is achieved by using a scale factor, calculated by dividing the true width of the tube by its corresponding pixel count.

Consequently, a table is produced containing two primary columns: one indicating the time that has passed since ignition, and the other indicating the location of the flame front relative to the spark ignition. This approach offers a comprehensive and accurate examination of the flame's advancement across time.

4.10 Flame Speed Calculation

An in-depth examination of the flame pictures is required to calculate the flame speed along the centerline of the tube. The data gathered in the preceding section 4.9 is crucial for this procedure. The Absolute Flame Speed (AFS) is determined using the following formula:

$$AFS_n = \frac{X_n - X_{n-1}}{t_n - t_{n-1}} \quad (4.1)$$

Where X_n and X_{n-1} are the flame front locations at times t_n and t_{n-1} respectively.

4.11 Inaccuracy Sources

Mjbel (Mjbel et al., 2021) has done his Master's thesis with the same experimental setup. He calculated all relevant uncertainty regarding this rig

in Appendix B of his thesis. The same setup has been used in this study. Therefore, Mjbel (Mjbel et al., 2021) uncertainty calculations can still be valid.

The main source of error is attached to the equivalence ratio determination and mixture preparation. Based on (Mjbel et al., 2021) work, the equivalence ratio uncertainty is about ± 0.06 . This can cause an issue in the differentiation of the results between equivalence ratios 1.0 and 1.1. The primary source of uncertainty in this study relates to the determination of the equivalence ratio and the preparation of the mixture. Additionally, the reproducibility of the results, particularly in the context of tulip flame formation, is somewhat uncertain. As a result, it becomes essential to repeat each experiment multiple times, ideally around 30 iterations, to achieve a reliable statistical analysis.

The issue of non-repeatability, which will be explored in greater detail in Chapter 5, is primarily attributed to the chaotic nature of the flow of the unburned mixture. This unpredictability is a key reason for the necessity of numerical modeling of this phenomenon. Furthermore, there are inherent uncertainties involved in processing the images recorded of the flame to determine the flame front speed. To identify the position of the flame front, a specific threshold of line intensity is used. This method typically results in locating the flame front within an accuracy range of one to two pixels, equivalent to about 3-6 *mm*.

CHAPTER FIVE
RESULTS AND DISCUSSION

CHAPTER FIVE

RESULTS AND DISCUSSION

5.1 Introduction

Improving combustion processes requires a thorough understanding of flame properties, such as temperature, velocity, and tulip flame generation. These features are shaped, in large part, by critical variables including time, pipe length, and fuel-to-air ratio. Time affects the rate at which the combustion process and the flame front evolve, which, in turn, affects the general behavior of the flame. The stability, form, and heat transmission of the flame are all impacted by the length of the pipe. An important mixture composition parameter, the fuel-to-air ratio, has a major impact on combustion dynamics, affecting flame temperature, speed, and the formation of structures such as tulip flames. Comprehending these interplays is essential to maximize combustion efficiency, reduce emissions, and guarantee system security.

Despite much investigation, the phenomenon of tulip flame formation in LPG-air premixed tubes is still not entirely understood due to its complicated structure. Numerous possible explanations are suggested by experiments, analyses, and computational studies. These include the effects of burning gases, viscosity, cooling, and vortex motion on pressure wave interactions and flame instability. The objective of this study is to determine the physical mechanisms behind the development of tulip flames by investigating the effects of tube length and equivalent ratio on flame front propagation, as well as the variables influencing the appearance of the tulip phenomenon. Thoroughly contrasting experimental and numerical data will shed light on these systems and advance our knowledge of and ability to

regulate combustion processes.

5.2 Present Work Verification

Present work validation contours, visualization validation, and charts are components of data analysis and quality assurance. They contribute to the accuracy, dependability, and effectiveness of data analysis procedures as well as data visualization, allowing for better decision-making and understanding of complicated information.

5.2.1 Model validation

Validation of experimental work involves comparing the collected data with results obtained from different models and previous investigations. The ILPG-air deflagration process in a pipe was simulated using various turbulence models, namely the Realizable k - ϵ model, k - ϵ model, SST k - ω model, and Launder Sharma k - ϵ model. The simulation results were compared with experimental data for flame speed with distance represented in Figure 5.1. Among the turbulence models used, the k - ϵ model demonstrated the closest agreement with the experimental results. In the numerical simulation, the combustion reaction occurred promptly upon ignition, while the experimental setup experienced a time delay due to electric spark ignition. Despite observing faster flame propagation during initial ignition in the simulation, the flame speed along the pipe axis remained in line with the experimental data. The simulation employed an adiabatic wall boundary condition, retaining all combustion heat within the products. Although the experimental flame acceleration was relatively delayed and the flame speed increased gradually, the maximum flame propagation speed error was less than 10%. Thus, it is concluded that the boundary condition had minimal impact on the overall flame propagation

trend, and the k- ϵ model proved to be an appropriate choice for simulating this LPG-air deflagration process in the pipe.

Figure 5.2 presents the comparison between experimental peak pressures and calculated pressures at each measuring point along the pipe. Notably, the maximum peak pressure was observed at the measuring point located at the end of the pipe. The simulation using the k- ϵ model resulted in slightly lower calculated pressures compared to the experimental data this difference can be attributed to the absence of energy loss in the simulated pipe. However, both the k- ϵ model and the Launder Sharma k- ϵ model significantly underestimated the peak pressures compared to the experimental results. Given these findings, the study aims to validate the suitability and accuracy of the Realizable k- ϵ model for this particular propane-air deflagration simulation in the pipe. Further investigations are warranted to understand and improve the predictive capabilities of the turbulence models and their application in similar scenarios.

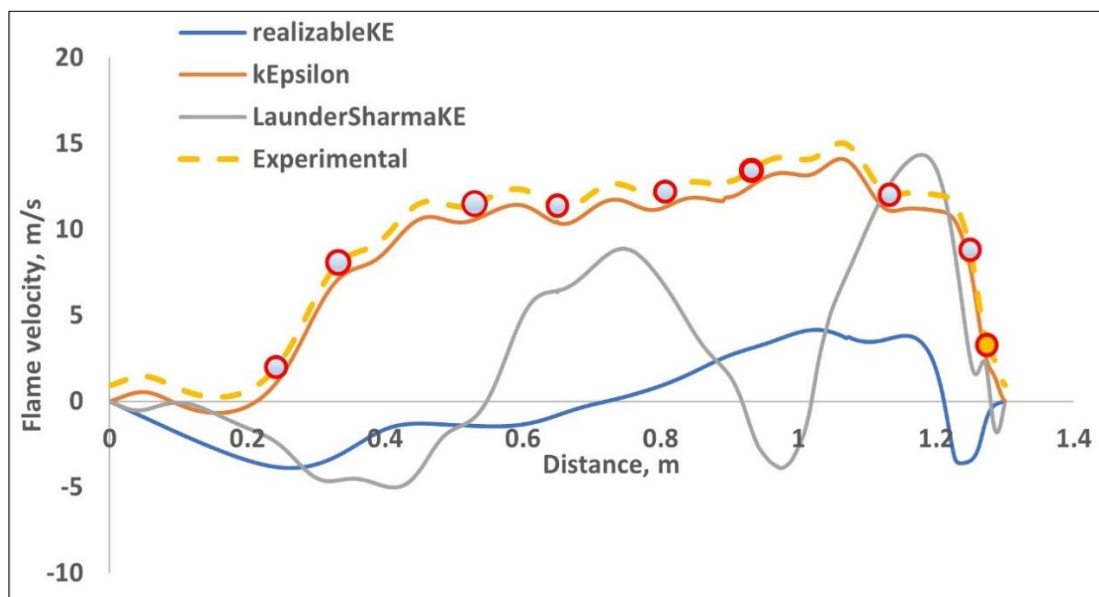


Figure 5.1: Flame speed distribution along the pipe axis of various models and compared with experiential results

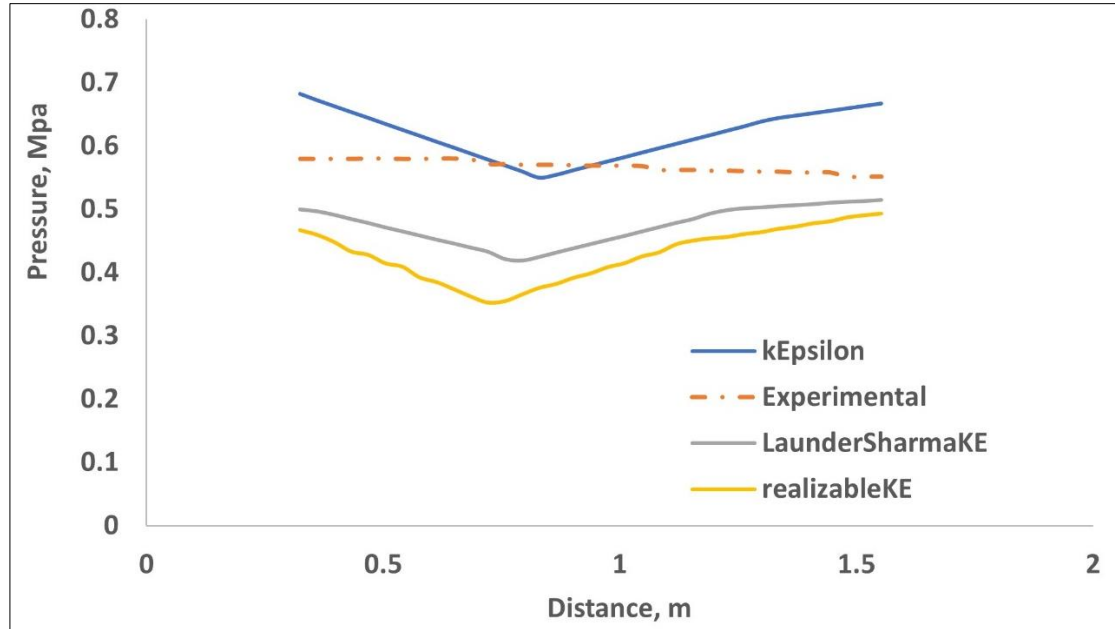


Figure 5.2: Flame pressure distribution along the pipe axis of various models and compared with experiential results

5.2.2 Contours and visualization validation

The present work demonstrates a high level of agreement with the findings reported by Zakaria Movahedi (Movahedi, 2017), both in terms of experimental and numerical results shown in Figure 5.3. The comparison of the two publications reveals similar patterns and occurrences in several aspects of the inquiry, including the location, velocity, and dynamics of flame generation. The experimental results of this research demonstrate comparable patterns and characteristics to those reported by Zakaria Movahedi, indicating a strong level of consistency and dependability in the experimental setups and data collection methods used. The observed congruence in the experimental outcomes enhances the degree of assurance about the accuracy of the present investigation. Furthermore, the quantitative results obtained in the present study demonstrate a noteworthy agreement with the numerical simulations carried out by Zakaria Movahedi. Although there are some differences due to the absence of a wrinkle

component in the laminar combustion model, both studies effectively capture essential qualitative elements related to the development of the tulip flame and the subsequent collapse of its edges. The consistent findings found indicate that the numerical model used in this work is very suitable for modeling and understanding the dynamics of the flame during these specific phases. The alignment between the observed and calculated results of the present inquiry and the study done by Zakaria Movahedi strengthens the accuracy of the findings and reinforces the reliability of the used methods and frameworks. The consistent findings in the data from both investigations provide strong confirmation, confirming the quality and dependability of the acquired information. This confirmation, in turn, enhances the overall understanding of the propane-air explosion mechanism and the tulip flame phenomena that take place within the pipe.

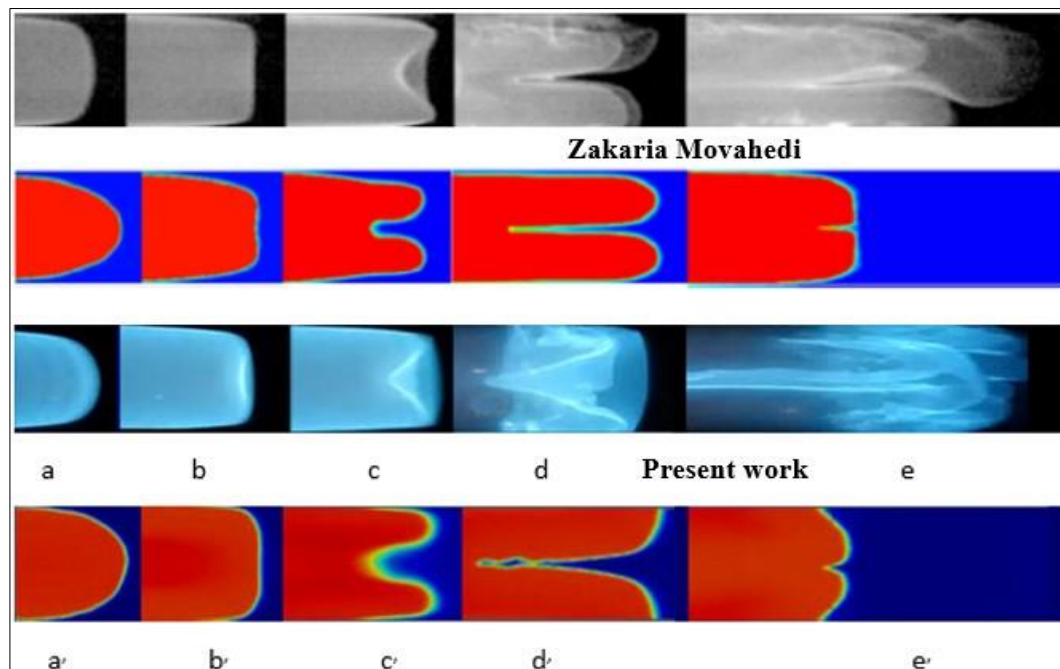


Figure 5.3: The validation between experimental work and numerical simulation of present and previous investigations

Figure 5.4 provides a depiction that clarifies the complex dynamics involved in the combustion process, particularly related to the processes that control the spread of flames. An extraordinary occurrence in the described scenario is the sudden appearance of a flame shaped like a tulip exactly at the time of 0.04 seconds. The tulip flame has a distinct morphology that is evocative of the floral structure of a tulip.

A precise and comprehensive illustration of the intricate mechanisms involved in flame spread may be found in Figure 5.4. This sheds interesting light on the dynamic processes that take place during the tulip flame's development, particularly during the 0.0350 *ms* timeframe. And it complies with the theoretical approach of Ashwin Hariharan (Hariharan & Wichman, 2014).

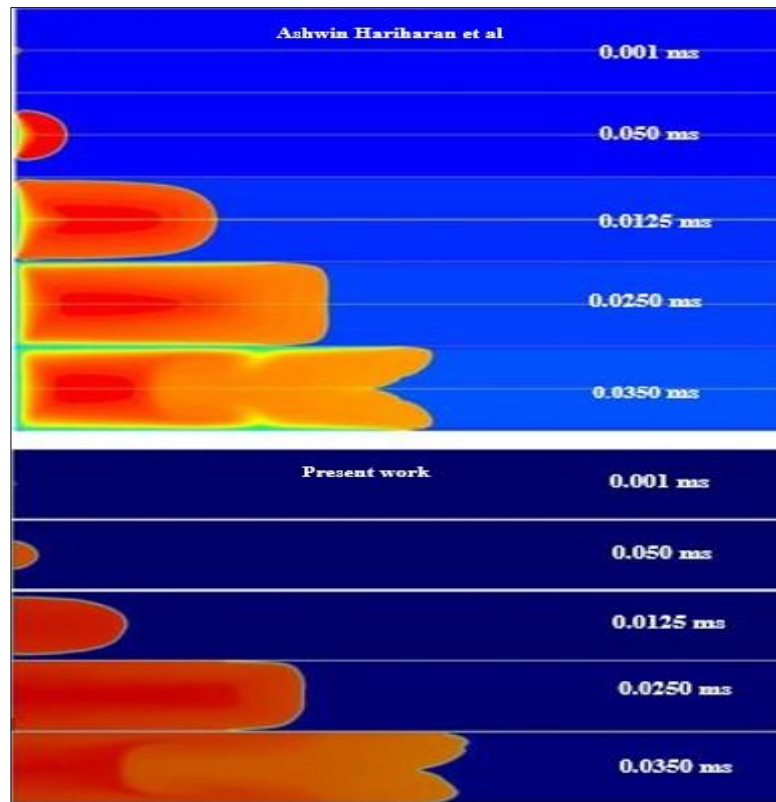


Figure 5.4: The validation between numerical present work and numerical simulation of Ashwin Hariharan

Figure 5.5 displays the contour of the adiabatic flame temperature inside the combustion chamber. The observed phenomenon offers empirical support for the propagation of the flame over the whole length of the combustion chamber. Approximately 10 *ms* into the combustion process, it has been observed that the flame will transform into a spherical shape. Following the progress in the central canal (CC), it undergoes a transformation into a digit-like structure after a duration of 15 *ms*. The flame progresses through the combustion chamber (CC) and develops a tulip-like shape at 45 *ms*. Subsequently, it undergoes a transformation from a non-planar form to a flat configuration at 30 *ms*. The tulip configuration undergoes progressive disintegration starting at 65 *ms* and persists until the conclusion of the current cycle (CC) at 80 *ms*, at which point it completely occupies the CC. The decline of the tulip configuration begins at 65 *ms*, the trend obtained in the present work agrees with the flow-distraining gained by (Kadem, 2021; Tecplot, 2013).

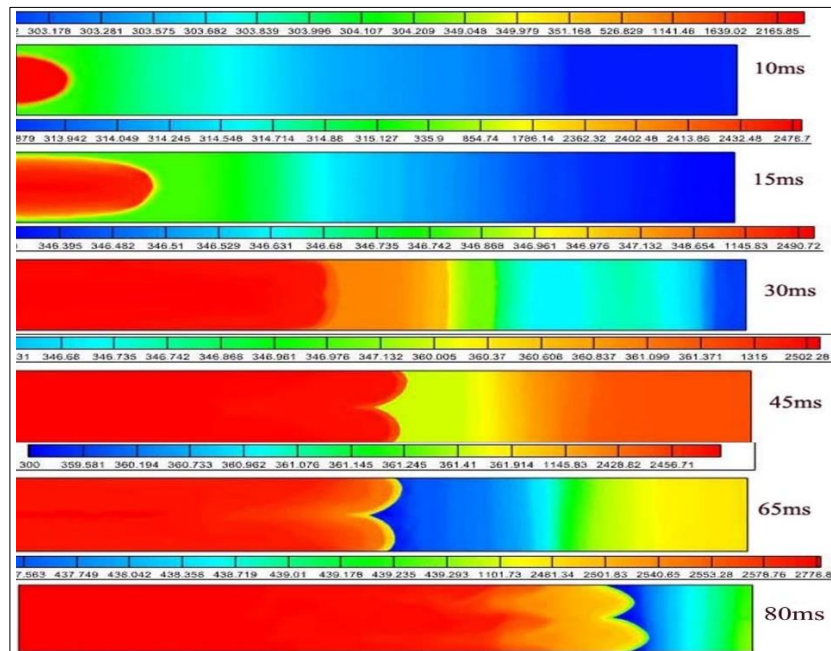


Figure 5.5: Flame shape and progress

5.2.3 Behavior validations

A graphic comparison of the flame front's distance from the spark over time is shown in Figure 5.6. It compares the simulated results from the current research with the findings of Zakaria. The graph illustrates the relationship between time (measured in *ms*) on the x-axis and the distance of the flame front from the spark (measured in *m*) on the y-axis. It demonstrates the advancement of the flame front in a stoichiometric Fuel-air combination inside a tube. Upon examination of the graph, it is evident that two distinguishable lines depict the datasets from the current investigation and the findings obtained by Zakaria. Both lines demonstrate an initial, progressive expansion of the distance between the flame front and the spark, showing the phase of flame propagation. Over time, the pace at which the flame front distance increases become more unpredictable, exhibiting peaks and troughs that indicate fluctuations in the velocity of the flame front.

The initial stage demonstrates a strong concurrence between both sets of findings, as the flame front advances at a comparable pace. Over time, several inconsistencies between the two databases became apparent. These disparities might be ascribed to discrepancies in experimental settings, the accuracy of measurements, or the faithfulness of the numerical simulations.

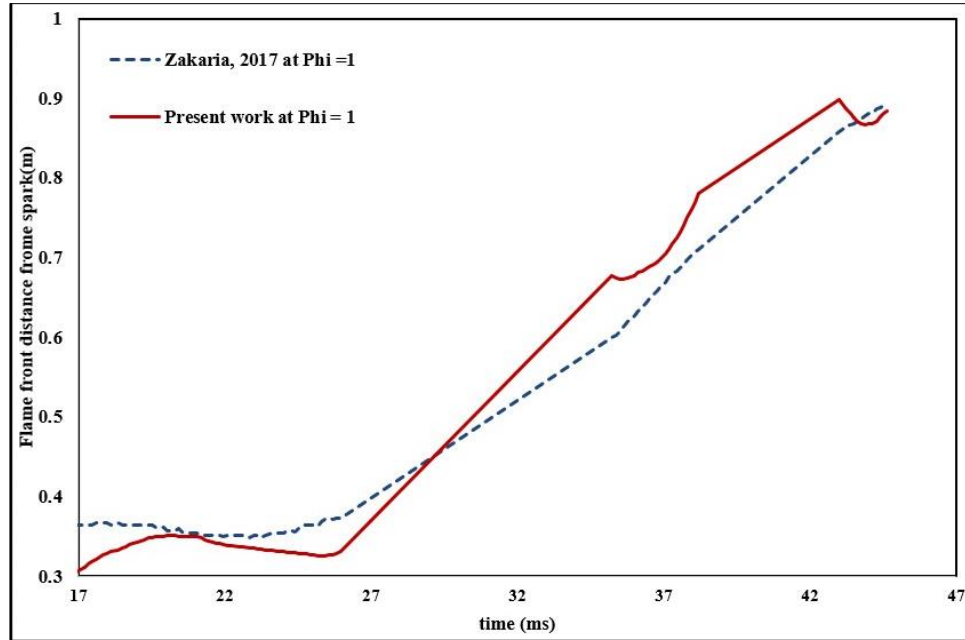


Figure 5.6: Flame front distance from spark for different time comparison

A thorough quantitative analysis that attempts to show a connection between the numerical results and the empirical data is shown in Figure 5.7. The collected data shows a correlation between the flame's location and velocity during the first 32 *ms*, before the tulip flame is formed. This indicates that the model accurately depicts the development of the tulip flame. However, from the time the tulip flame zone occurred until $t = 54$ *ms*, the numerical results consistently underestimated the actual findings. The discrepancies seen between the computational and experimental results may be attributed to the turbulence produced in the unburned mixture as a result of the flame expansion. Turbulence significantly impacts the dynamics of flame propagation, leading to significant changes in both the velocity and behavior of the flame. In this situation, it is possible that the turbulent flow caused by the flame's growth might affect the spread of the flame beyond the area marked by the tulip flame. Hence, this phenomenon may explain the discrepancies reported

between the numerical predictions and actual findings. To improve the accuracy of the numerical model and better represent the movement of flames, it is essential to conduct more investigations and make necessary adjustments to the model. By include a more detailed analysis of turbulence in the simulation, it is possible to reduce these differences and improve the model's ability to forecast the whole process of flame propagation. The research done by Zakaria Movahedi (Movahedi, 2017) showed that the geographical distribution and velocity of the flame during the first 30 *ms*, before the tulip-shaped flame forms, had a high degree of agreement. This implies that the model used in the experiment accurately depicts the development of the tulip flame. However, after the tulip flame zone event and continuing until $t = 50$ *ms*, a noticeable inconsistency in the timing references about the observed differences between the numerical and experimental results becomes evident.

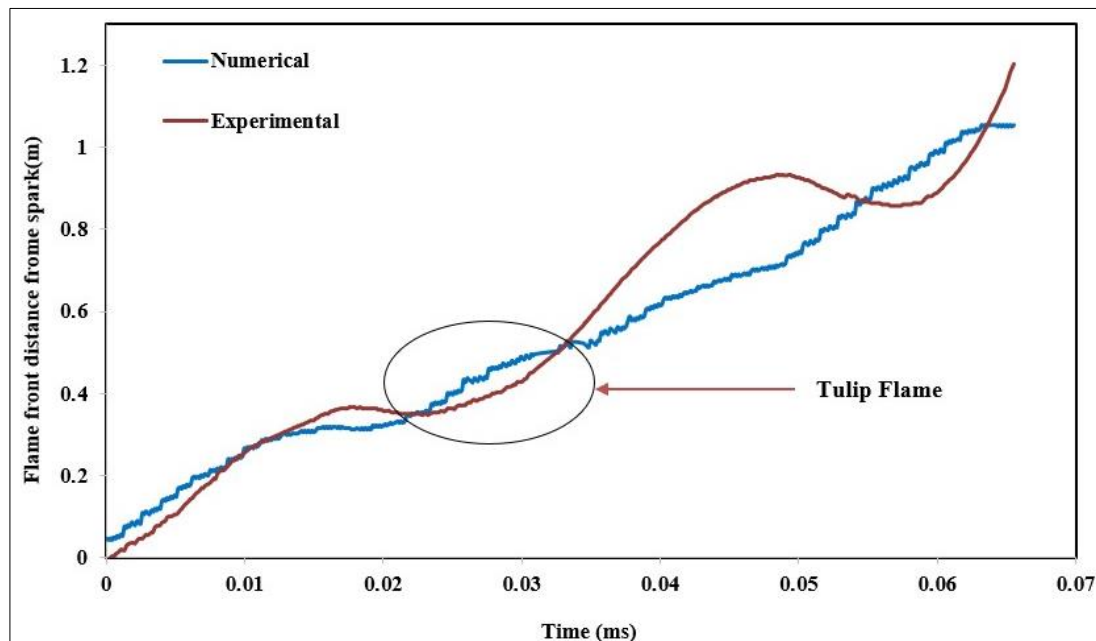


Figure 5.7: Flame front distance from spark of numerical and experimental work and compare with previous investigation

5.3 Factors Effect on Flame Properties

Flame propagation can be influenced by two specific factors: tube length and equivalency ratio (Xiao, 2016).

Tube Length: Flame propagation may be affected by the length of a combustion tube or chamber. Before reaching the tube outlet, the flame must travel a greater distance through longer tubes. This greater separation may result in longer heat loss and dissipation times to the tube walls, which could impede the spread of the flame. In contrast, shorter tube lengths may facilitate the spread of flames faster because there is less space for heat dissipation and less distance to go.

The equivalency ratio is a measurement of the ratio between the composition of the actual fuel-to-air mixture and the stoichiometric ratio needed for full combustion. It shows if the combination contains a lot of fuel or not (Xiao et al., 2018).

5.3.1 The effect of equivalent ratio on flame front position and velocity for 1.5 m length

The location and speed of the flame front in a 1.5 m long chamber of combustion is influenced by the equivalency ratio, as shown graphically in Figure 5.8. The graph illustrates the variation in flame tip distance from the ignition point over time for three distinct equivalency ratios: lean ($\phi = 0.8$), stoichiometric ($\phi = 1$), and rich ($\phi = 1.2$) LPG-air mixtures. By examining the graph, we may see three separate lines, each indicating a different equivalency ratio

Initial Phase: The three lines all have a comparable slope, indicating that at the beginning, the equivalency ratio has little influence on the speed of the flame front. The flame fronts in all mixes spread uniformly away

from the igniting source. Temporal evolution of the flame fronts reveals discernible discrepancies in their actions, indicating a mid-phase variation. The convergence of the red line (representing a rich mixture) and the black line (representing a stoichiometric mixture) indicates that mixes with higher richness ($\phi = 1$ and $\phi = 1.2$) lead to a more consistent flame front location as time progresses. The convergence may be attributed to the enhanced accessibility of fuel, which facilitates continuous burning and has the potential to result in more uniform flame propagation velocities.

- 1) The lean mixture diverges from the other two lines, as shown by the blue line. The observed discrepancy suggests that leaner mixes ($\phi = 0.8$) exhibit distinct flame front propagation characteristics, perhaps attributed to reduced fuel availability, resulting in slower flame speeds and lower total energy release rates.
- 2) **Late phase** oscillations are seen in the later portion of the graph, when all lines exhibit oscillatory activity. The magnitude of these oscillations is particularly noticeable in the rich combination, shown by the red line. The oscillations seen correspond to the physical occurrence of the development and collapse of the tulip flame, with the magnitude potentially being affected by the richness of the mixture. Distance Disparities: Across the graph, the red line constantly exhibits the greatest flame tip distances, followed by the black line, and then the blue line. This trend indicates that the use of more concentrated mixes leads to a more energetic spread of the flame front.

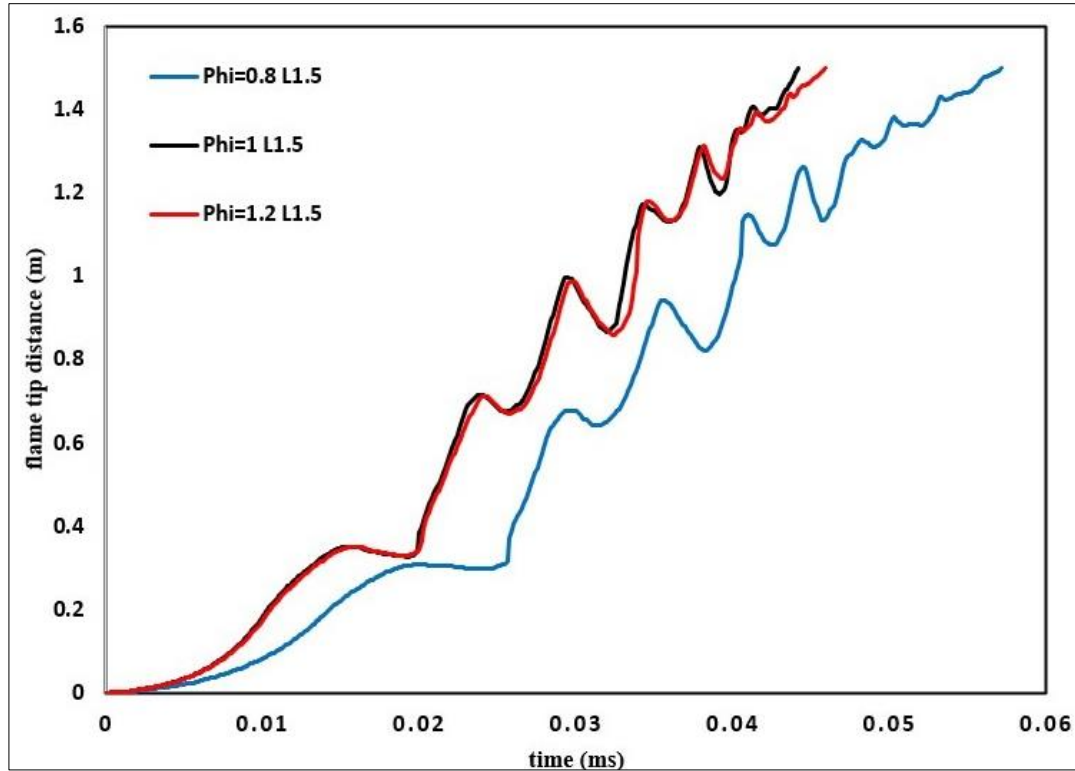


Figure 5.8: Flame tip distance with time for different equivalence ratio at L1.5 m

Presents Figure 5.9, a graphical representation of the flame tip velocity as a function of time for various equivalence ratios (ϕ) for a tube length of 1.5 m. Three lines are graphed, each representing a different equivalence ratio: lean ($\phi = 0.8$), stoichiometric ($\phi = 1$), and rich ($\phi = 1.2$). The salient findings derived from Figure 5.9 are as follows: Stoichiometric Mixture Behavior (a stoichiometric ratio $\phi = 1$) The flame tip velocity for the stoichiometric combination has a concentrated distribution along the time axis, suggesting a reasonably steady velocity with fewer and less severe changes. When the fuel-to-air ratio reaches the stoichiometric point, the flame demonstrates a more predictable and regulated spread. The behavior of a lean mixture (stoichiometric ratio of $\phi = 0.8$) At first, the speed at which the flame point moves in the lean mixture is lower than in the other mixes, as predicted because of the

reduced amount of fuel present. After 0.04 *ms*, the variation in velocity decreases, indicating that the lean mixture has a damping effect on the velocity oscillations.

The decrease in variation after 4.4 *ms* suggests a more consistent flame front velocity as the flame develops. The behavior of a fuel-air mixture with a high concentration of fuel (known as a rich mixture) is shown in a graph when the air-fuel ratio is 1.2. The velocity of the rich combination exhibits the most pronounced oscillations, characterized by elevated peaks and reduced troughs. The magnitude of these oscillations suggests the dynamic character of the flame front in fuel-rich mixtures, perhaps resulting from the increased energy content and consequently more intense combustion processes. The velocity oscillations seen in all three lines indicate the periodic nature of the tulip flame production and its influence on the velocity of the flame tip. The fluctuations in both the intensity and rate of these vibrations at various equivalency ratios demonstrate the intricate nature of combustion dynamics and the responsiveness of flame characteristics to variations in the fuel-air combination.

Comparative Analysis: When comparing the three lines, the stoichiometric mixture ($\phi = 1$) maintains a relatively stable and moderate flame tip velocity, while the lean mixture ($\phi = 0.8$) demonstrates a tendency towards lower velocities, and the rich mixture ($\phi = 1.2$) displays higher velocities with notable fluctuations. The observations obtained from Figure 5.9 are crucial for understanding the mechanics of flame propagation, specifically how the equivalency ratio affects the speed and steadiness of the flame front. This information is essential for enhancing combustion processes, guaranteeing safety in industrial environments, and

enhancing the efficiency of engines and other combustion equipment. The picture emphasizes the intricate relationship between the concentration of fuel and the kinetics of combustion, emphasizing the need for accurate control over mixture ratios in real-world scenarios.

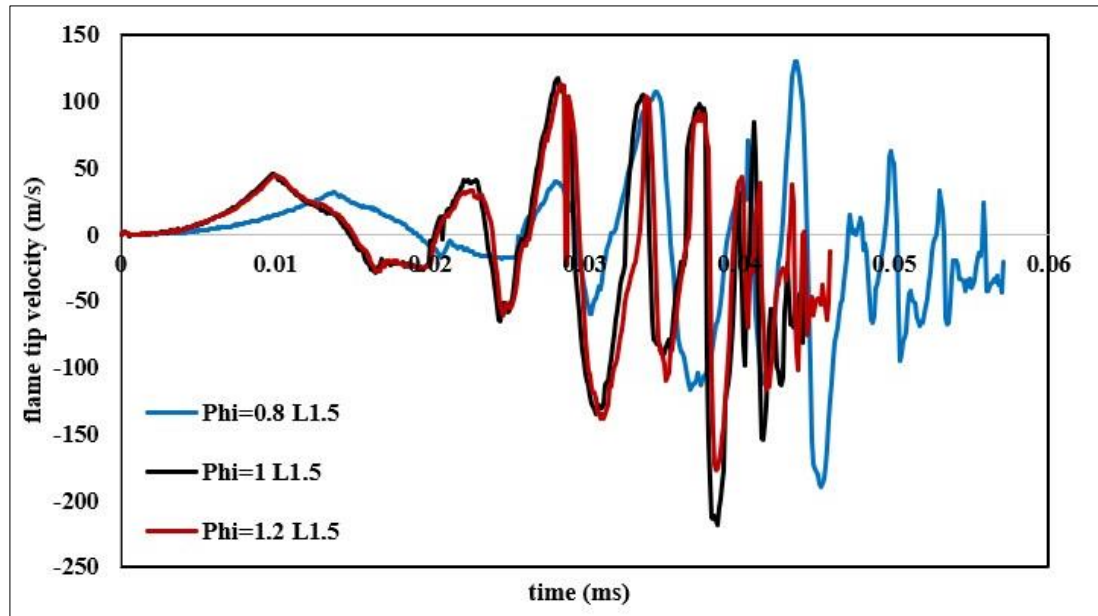


Figure 5.9: Flame tip velocity with time for different equivalence ratio at L1.5 m

5.3.2 The effect of equivalent ratio on flame front position and velocity for L2 m length

provide insight into how different equivalence ratios affect flame front position and velocity, respectively, in a 2m-long combustion chamber, as shown in Figures 5.10 and 5.11. For the fuel-lean mixture ($\phi = 0.8$), this represents the lean mixture scenario. Here, the flame tip distance increases at a slower rate than in the other mixtures. This suggests that the lack of fuel relative to air slows down the combustion process, resulting in less aggressive flame front propagation. While the stoichiometric mixture ($\phi = 1$) shows the behavior of the stoichiometric mixture, The distance of the flame tip increases steadily and at a moderate rate, indicative of an optimal

balance between fuel and air, leading to consistent combustion.

The fuel-rich mixture ($\phi = 1.2$) is illustrated in the rich mixture case, where the flame tip distance increases most rapidly. The excess fuel results in a more robust combustion process, causing the flame to travel faster and further along the tube, as shown in Figure 5.10.

Flame Tip Velocity, Figure 5.11: In the lean mixture, the flame tip velocity is generally lower and less variable compared to the other mixtures. After a certain time, there's a notable decrease in velocity, reflecting the struggle of the flame to maintain its propagation due to limited fuel availability. The stoichiometric mixture, where the velocity initially rises to a peak and then fluctuates around a central value, this behavior indicates a balanced combustion dynamic, with neither excess fuel nor excess air. The rich mixture shows high velocity with significant fluctuations. The peaks and valleys in the velocity profile suggest an intense and somewhat unstable combustion process, likely due to the ample fuel availability causing rapid but uneven combustion.

It is found that the rich mixture has the highest flame front velocity, followed by the stoichiometric mixture, and then the lean mixture, consistent across both figures. This progression is aligned with the expectation that more fuel leads to more vigorous combustion. The stoichiometric mixture provides a balance between speed and control, as indicated by the moderate and stable flame tip distance and velocity. In contrast, the rich mixture, while fast, shows greater volatility, and the lean mixture, though slower, demonstrates steadiness in propagation speed. Figures 5.10 and 5.11 together illustrate the nuanced interplay between mixture composition and combustion dynamics. The rich mixture's rapid flame front progression and high velocity indicate a strong and potentially

more aggressive combustion process, while the lean mixture shows constraints on combustion due to limited fuel.

These figures underline the importance of the equivalence ratio in determining the behavior of flames within a combustion chamber. Understanding these dynamics is crucial for the design and operation of combustion systems, ensuring optimal performance, efficiency, and safety. The rich mixture's rapid progression might be beneficial in scenarios where high energy release is desired, while the lean mixture's slower and more controlled propagation might be advantageous situations where safety and fuel efficiency are paramount.

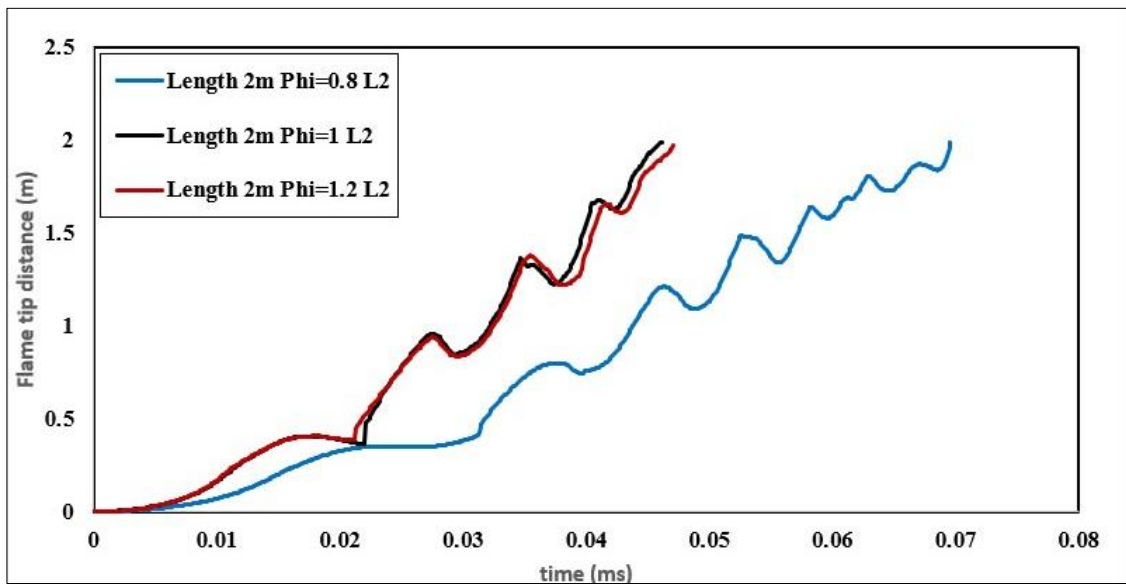


Figure 5.10: Flame tip distance with time for different equivalence ratio at L2 m

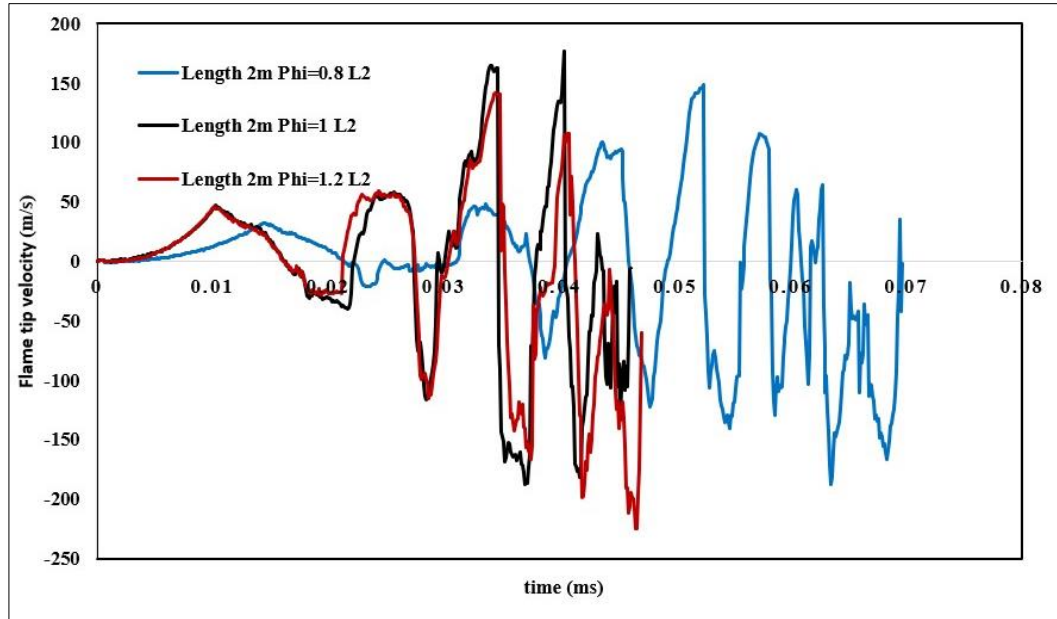


Figure 5.11: Flame tip velocity with time for different equivalence ratio at L2 *m*

5.3.3 The comparison of various lengths for different equivalent ratio

depicts the progression of flame tip distance over time for stoichiometric mixtures ($\phi = 1$) within combustion chambers of two different lengths. Figure 5.12 provides a comparative analysis of how chamber length influences flame propagation. The graph presents two lines: the flame tip distance for a combustion chamber of length L2 *m* corresponds to a chamber with a length of L1.5 *m*. Both lines track the distance of the flame front from the ignition source over time, which reflects the flame's propagation speed and pattern within the chamber.

Initial Flame Propagation (0 to ~ 0.02 *ms*): Both lengths start with a similar trajectory, suggesting that the initial combustion behavior is relatively unaffected by the chamber length. This could indicate that the initial flame propagation is primarily driven by the stoichiometric mixture's energy release, which is consistent regardless of chamber size. Mid-Phase

Flame Propagation (~ 0.02 to ~ 0.035 ms): As time progresses, the behavior begins to diverge. In the tube line (L2 m), the trend climbs at a slightly steeper angle than in the L1.5 m lengths. This divergence suggests that the flame in the longer chamber (L2 m) may be experiencing different conditions that allow for a faster propagation rate during this phase. Late-Phase Flame Propagation (~ 0.035 ms onwards): The blue line (L2) continues to show a greater distance traveled compared to the yellow line (L1.5) as time increases. The increased distance in the longer chamber could be due to less heat loss to the walls, as the flame has more space to develop and potentially a more sustained combustion process before wall effects become significant.

Finally, Flame Behavior: Throughout the graph, the flame in the longer chamber consistently maintains a lead-in tip distance over time, suggesting a sustained advantage in propagation speed. This could be the result of a combination of factors such as heat dissipation, flame structure stability, and interaction with chamber walls, which are affected by chamber length. Implications The graph illustrates that chamber length does have a discernible impact on flame propagation in a stoichiometric mixture. For applications where flame speed and control are important, such as in engines or safety systems, the results from this graph could inform design decisions regarding the optimal chamber length for desired combustion characteristics.

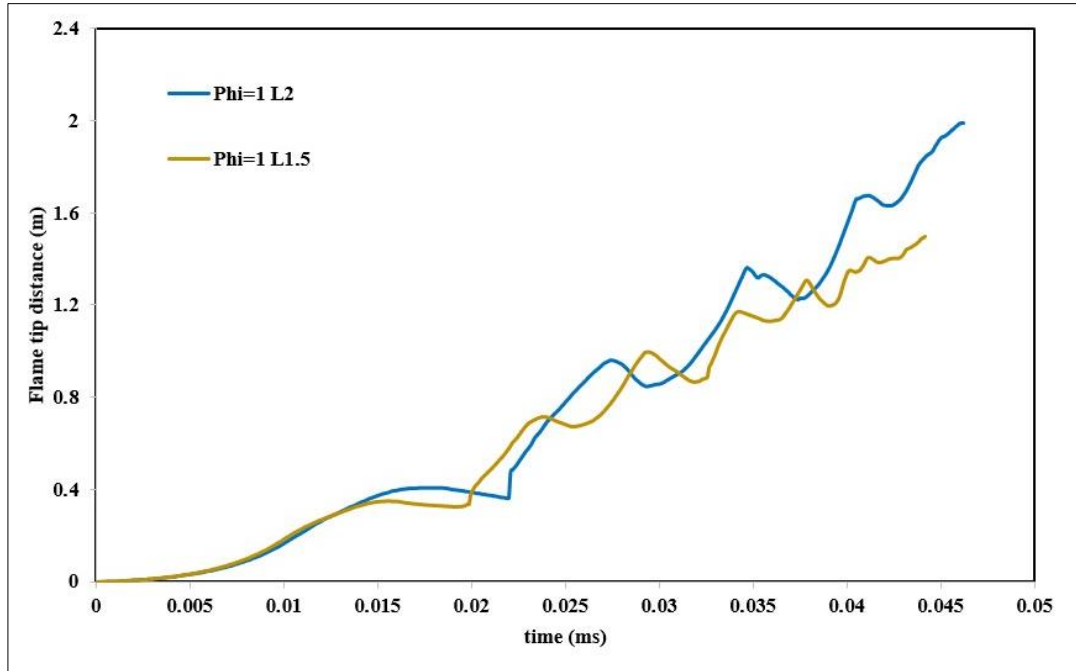


Figure 5.12: Flame tip distance with time at different length comparison for $\Phi = 1$

Compares the flame tip distance over time for two combustion chamber lengths (1.5 m and 2 m) using a fuel-rich equivalence ratio (Φ) of 1.2. This ratio indicates a greater amount of fuel relative to the oxidizer than what is needed for complete combustion, as shown in Figure 5.13.

The key observations from Figure 5.13 are: Initially, both length (2 m chamber) and length (1.5 m chamber) start with nearly overlapping trajectories, suggesting that the initial influence of chamber length on the flame propagation of a fuel-rich mixture is minimal. Mid-Phase Divergence: As the flame progresses, the lines start to diverge slightly, with the 2m chamber rising above the 1.5 m chamber. This divergence indicates that a longer chamber allows for a slightly increased flame tip distance over time. Concerning late-phase propagation, as we move toward the end of the curve, this means that the flame in the longer chamber has a prolonged advantage in tip distance, most likely due to the additional space allowing for continued acceleration or less influence from wall cooling.

As for the tulip flame appearance, the oscillatory nature of both lines suggests the development of tulip flame structures at certain intervals, as indicated by the periodic dips. The fact that these patterns appear in both chamber lengths but with slight variations emphasizes the effect of chamber length on the dynamics of tulip flame formation. The overall higher flame tip distance in the 2 *m* chamber throughout the graph shows that the chamber length plays a role in facilitating flame propagation. The longer chamber provides a larger area for the combustion process, which can support the stability and distinct shape of the tulip flame due to lessened wall interference and prolonged energy release the comparison in Figure 5.13 reveals that while the initial flame front propagation is not significantly affected by chamber length, as time goes on, the benefits of a longer chamber become apparent, with a greater flame tip distance observed. The behavior of the flame tip distance over time indicates that a fuel-rich mixture in a longer chamber can sustain flame front propagation more effectively than in a shorter one.

This finding is important for practical applications where the design of combustion chambers needs to optimize flame propagation speed and stability. The results suggest that a longer chamber could be beneficial in systems where more sustained combustion is desired, such as in power generation or propulsion systems where the complete combustion of a fuel-rich mixture is critical for performance. Figure 5.13 contributes to the understanding of how combustion chamber length influences flame propagation, especially for fuel-rich mixtures. The longer chamber length allows for a more pronounced flame tip distance over time, highlighting the importance of chamber design in optimizing combustion processes.

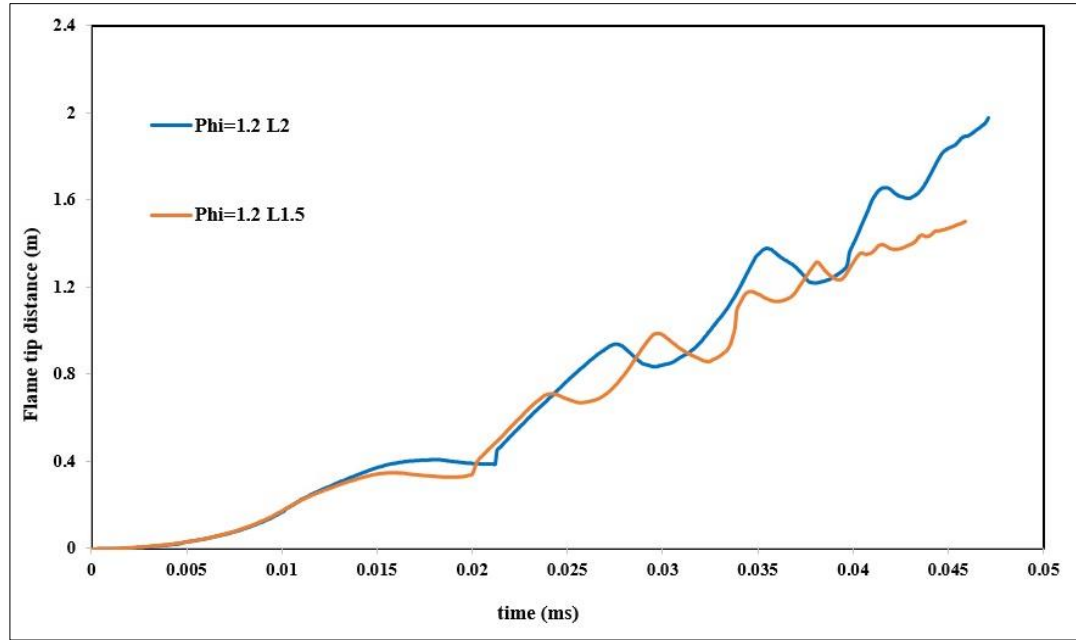


Figure 5.13: Flame tip distance with time at deferent length comparison for $\Phi = 1.2$

Figure 5.14 presents a comparative analysis of the flame tip distance over time within two different lengths of combustion chambers, 1.5 m, and 2 m, with a lean equivalence ratio of 0.8. This lean condition indicates that there is less fuel relative to the air than is needed for complete combustion. Initial Flame Behavior (0 to ~ 0.02 ms): The graph starts with the two lines, for the 2 m chamber and the 1.5 m chamber, closely aligned. This indicates that during the early phase of flame propagation, the length of the combustion chamber does not have a significant impact on the distance the flame tip travels.

Mid-phase flame propagation (~ 0.02 to ~ 0.04 ms): As the flame develops, the line, representing the longer chamber length, starts to show a greater flame tip distance. This suggests that the flame in the longer chamber has more space to accelerate and propagate, even under lean conditions. Late-Phase Flame Propagation (~ 0.04 ms onwards): The distinction between the chamber lengths becomes more pronounced, with

the 2 m chamber consistently exhibiting a larger flame tip distance. This could be due to reduced heat losses in the longer chamber, allowing the flame to maintain its speed over a greater distance. The periodic dips in both lines could indicate the presence of tulip flame phenomena, which are characterized by a temporary reduction in flame tip speed followed by acceleration. The dips appear to be less pronounced in the longer chamber, potentially due to the larger space dampening the effects of flame instabilities.

The lean condition of $\Phi=0.8$ typically results in slower flame propagation due to less available fuel. However, the data shows that even under lean conditions, the flame in the longer chamber can maintain a higher propagation speed over time compared to the shorter chamber. Figure 5.14 demonstrates that in a lean combustion environment, the length of the combustion chamber has a notable influence on flame tip distance, with longer chambers facilitating greater flame propagation. This understanding is critical for optimizing combustion chamber design in applications where space constraints and fuel conditions vary. It also underscores the adaptability of flame behavior to chamber dimensions, even when the fuel-to-air ratio is less than stoichiometric, which is important for the efficient design of combustion systems, particularly in lean-burn engines.

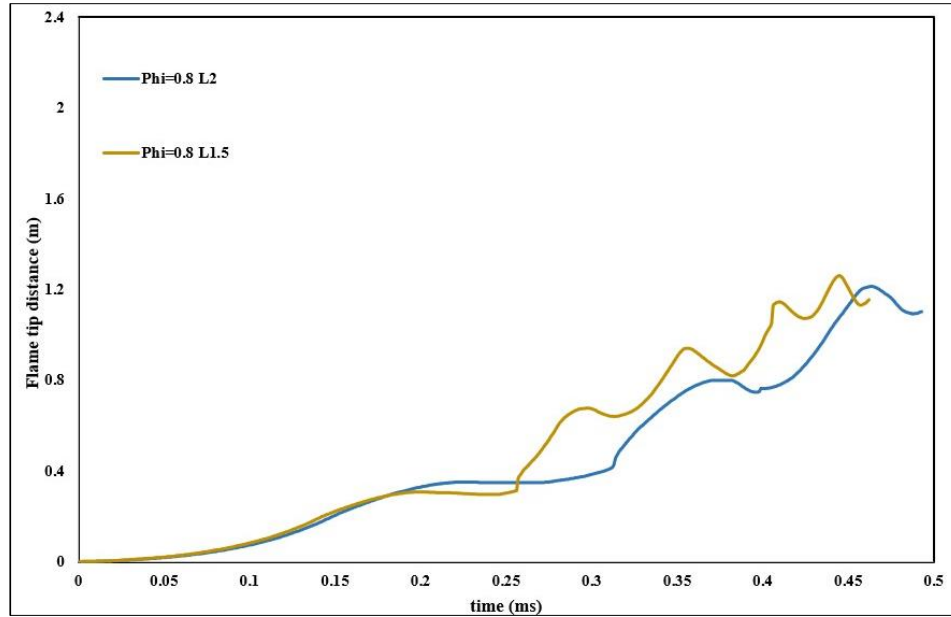


Figure 5.14: Flame tip distance with time at deferent length comparison for $\Phi = 0.8$

5.4 Tulip Formation Behavior

Tulip flame formation behavior is a phenomenon that occurs when a flame propagates in a tube, forming a tulip-like structure. This can happen due to the interaction of the flame with the flow field and the rarefaction waves in the tube. The mechanism of tulip flame formation depends on the type of ignition source, the tube geometry, and the fuel mixture (Aghaabbasi, 2021; Akkerman & Law, 2013; Bychkov & Liberman, 2000; Dunn-Rankin & Sawyer, 1998).

5.4.1 Tulip flame formation of 1.5 m for various Φ

Comparing the flame tip distance (in m) and flame tip velocity (in m per second) over time (in ms) for a stoichiometric mixture ($\phi = 1$) in a 1.5- m -long combustion chamber presents a dual-axis plot as shown in Figure 5.15. Initial Flame Propagation (0 to t_1): The flame tip distance, shown, increases steadily over time, reflecting a consistent flame front advancement. The corresponding velocity indicated remains positive,

suggesting a steady increase in speed. This period is marked by a smooth acceleration as the flame establishes itself.

Acceleration and Deceleration Phases (t_1 to t_2): At time t_1 , there is a noticeable change in the flame tip velocity. shows an initial peak and subsequent drop, which corresponds to a rapid acceleration followed by a deceleration of the flame tip. The distance continues to increase, but the rate of change varies, indicating the dynamic behavior of the flame front.

Oscillatory Behavior (t_2 to t_4): post- t_2 , the velocity line exhibits oscillatory behavior with significant peaks and troughs. These fluctuations in velocity correspond with the complex dynamics of flame propagation and are potentially indicative of the tulip flame phenomenon, where periodic accelerations and decelerations occur due to changes in combustion chamber pressure and flame shape. As for Tulip Flame Formation Intervals The dashed vertical lines (t_1 , t_2 , t_3 , and t_4) likely represent key moments in the flame's life cycle, possibly aligning with the formation and collapse of tulip flames. Each interval between these lines represents a cycle of the tulip flame's development, where the flame front's velocity increases and then decreases, only to increase again in the next cycle.

Notably, the flame tip velocity drops below zero multiple times, indicating that the flame tip is momentarily moving backward relative to the combustion chamber, a characteristic feature of tulip flame behavior where the flame front retreats before advancing again. Figure 5.15 effectively illustrates the complex and dynamic relationship between flame tip distance and velocity in a combustion process with a stoichiometric mixture. The oscillatory nature of the flame tip velocity highlights the non-linear behavior of flame propagation, especially in the presence of phenomena such as tulip flames. This information is essential for understanding

combustion dynamics and for designing combustion chambers that can accommodate such complex behaviors for improved safety and efficiency in practical applications.

Provides a Figure 5.16 chronological sequence of images depicting the propagation of a flame within a 1.5-meter-long combustion chamber with a stoichiometric fuel-to-air ratio ($\Phi = 1$). Each frame represents a snapshot at a specific point in time, measured in ms, showing the evolution of the flame shape as it advances through the chamber. **Early Flame Development (0.0162 ms – 0.0253 ms):** The initial frames exhibit the flame front as it begins to propagate from the ignition source. The flame is characterized by a smooth front that progressively elongates within the chamber. **Mid-Phase Development (0.0296 ms – 0.0358 ms):** As the flame travels further, we see the development of instabilities leading to the formation of a curved front. This is indicative of the flame experiencing variations in speed and pressure as it interacts with the chamber walls and the surrounding gases.

Tulip Flame Formation (0.0381 ms – 0.0405 ms): A distinct tulip flame shape emerges in the subsequent frames. This pattern is recognized by the indentation in the flame front, which resembles the shape of a tulip. This phase is critical as it demonstrates the complex behavior of flame dynamics in confined spaces. **Flame Propagation and Oscillation (0.0425 ms – 0.0441 ms):** The final frames show the flame as it continues to propagate while the tulip shape becomes more pronounced and then begins to oscillate. The oscillation of the tulip flame is a result of the complex interplay between combustion kinetics, fluid dynamics, and the geometry of the combustion chamber. Figure 5.16 captures the dynamic and transient nature of flame propagation under stoichiometric conditions within a 1.5-m

combustion chamber. The visual progression provides valuable insights into the stages of flame development and the characteristic formation of the tulip flame, which is a significant phenomenon in combustion science. This understanding is crucial for improving combustion efficiency, reducing emissions, and ensuring safety in industrial applications.

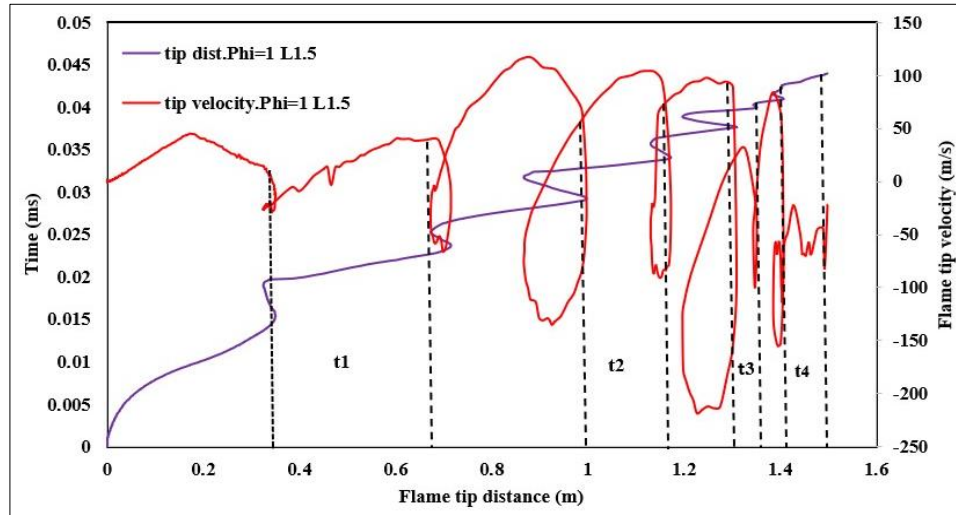


Figure 5.15: Correlation of flame tip distance and velocity over time in a 1.5 m CC with a stoichiometric mixture ($\Phi = 1$)

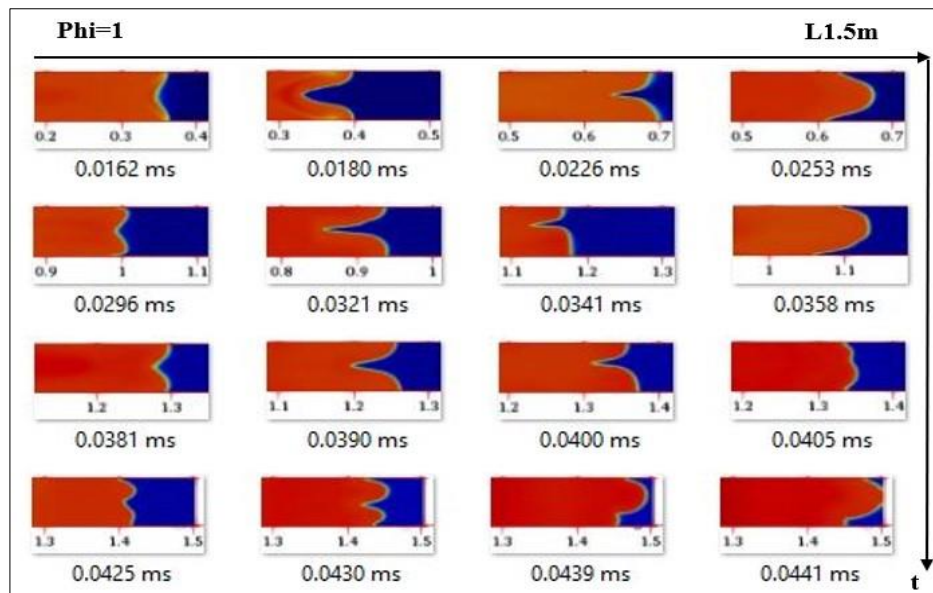


Figure 5.16: Sequential visualization of flame propagation in a 1.5 m combustion chamber at stoichiometric conditions ($\phi = 1$)

Juxtaposes Figure 5.17 shows the flame tip distance and velocity over time for a fuel-rich mixture ($\Phi = 1.2$) in a 1.5-meter combustion chamber. The plot illustrates the non-linear behavior of the flame front as it propagates through the chamber, captured by two distinct yet interrelated variables: the distance of the flame tip from the ignition source and its velocity. As for InitialPhase: (up to t_1), The flame tip distance increases steadily as the flame accelerates after ignition, while the velocity shows a gradual increase followed by a sharp peak, indicating rapid acceleration. Flame Tip Velocity Fluctuations (t_1 to t_4): Post t_1 , the velocity experiences significant fluctuations, marked by sharp increases and decreases, reflecting the complex interplay between combustion kinetics and chamber dynamics, particularly in a fuel-rich environment.

The vertical dashed lines (t_1 to t_4) potentially correspond to the characteristic stages of tulip flame formation, where the flame tip velocity reverses as the flame front momentarily retreats before advancing again. Notably, the flame tip velocity drops below zero several times, indicative of the tulip flame phenomenon where the flame briefly moves backward due to pressure waves and vortex formation within the chamber.

Provides a series of snapshots showing the evolution of the flame shape in a 1.5-meter-long combustion chamber with a fuel-rich mixture. Each image captures the flame at different times, illustrating how the flame front changes throughout propagation. As shown in Figure 5.18, Early Flame Tulip Shape (0.0165 ms – 0.0255 ms): Initially, the flame appears as a smooth curve extending from the ignition point, indicative of the initial propagation phase. Development of Instabilities (0.0300 ms – 0.0359 ms): As time progresses, the flame front begins to exhibit instabilities, developing into more complex shapes, which are likely precursors to the

tulip flame phenomenon.

Formation of the Tulip Flame (0.0384 *ms* – 0.0409 *ms*): The characteristic indentation of the tulip flame becomes visible, with the flame front taking on a shape reminiscent of a tulip flower. Oscillation and Flame Front Advance (0.0431 *ms* – 0.0457 *ms*): In the final frames, the tulip flame shape oscillates and advances, suggesting the dynamic nature of the combustion process within the chamber. Figures 5.17 and 5.18 together offer a comprehensive view of the flame dynamics within a fuel-rich environment in a 1.5-*m* combustion chamber. Figure 5.17 highlights the quantitative aspects of flame tip behavior over time, while Figure 5.18 provides qualitative visual evidence of the corresponding flame shapes. The figures underscore the complexity of flame propagation in fuel-rich conditions, where the interplay between fuel concentration, chamber geometry, and combustion dynamics leads to the formation and oscillation of tulip flames. These insights are valuable for the design and optimization of combustion systems in industrial applications.

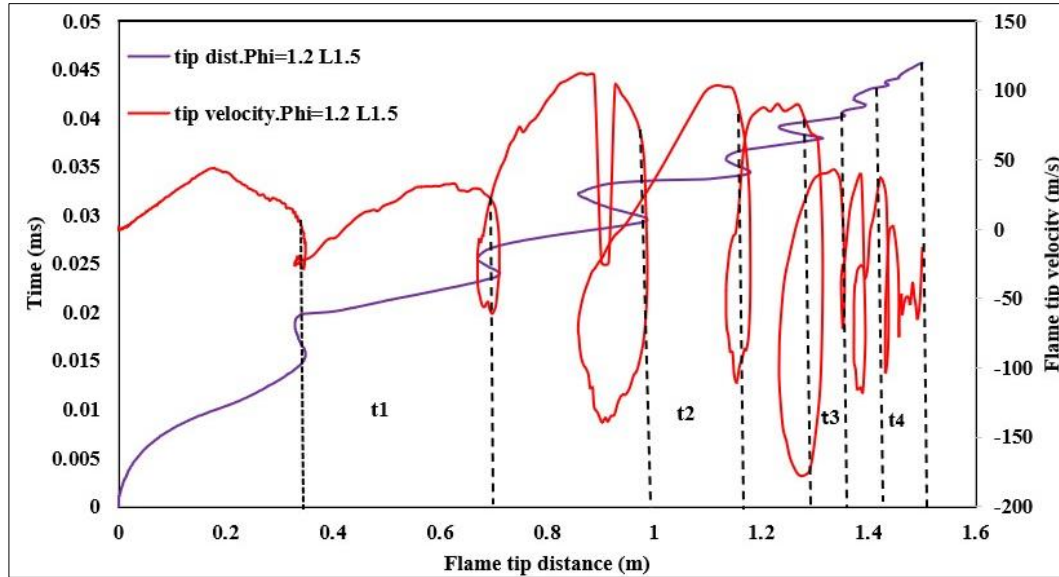


Figure 5.17: Dynamics of flame tip velocity and distance in a 1.5 m combustion chamber with fuel-rich mixture ($\Phi = 1.2$)

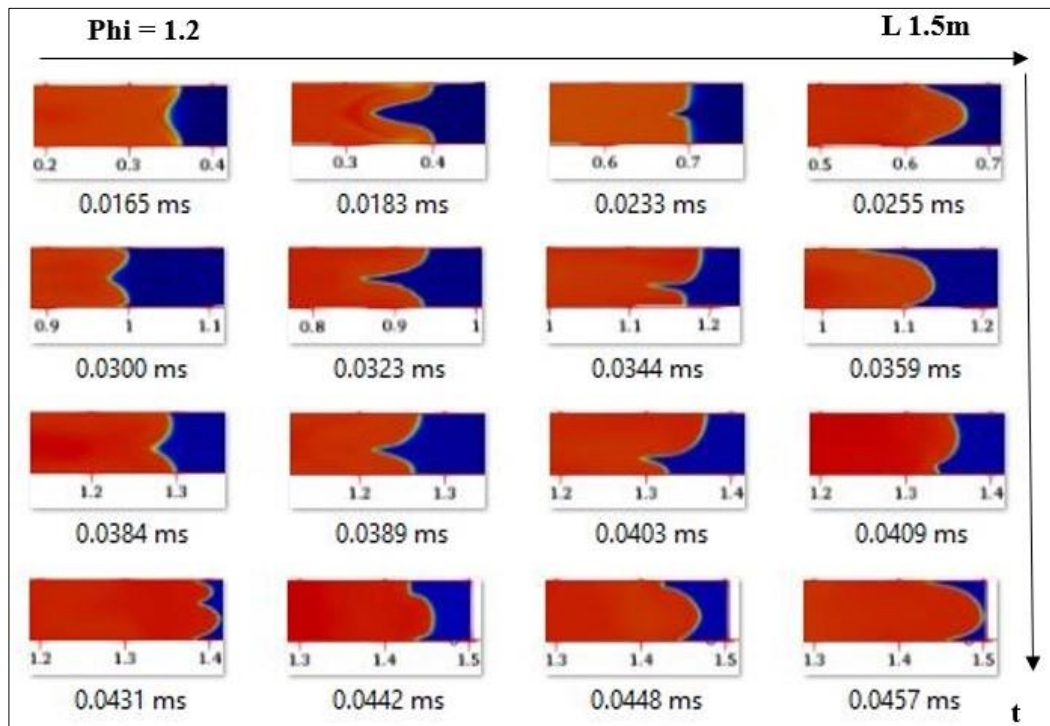


Figure 5.18: Temporal evolution of flame shapes in a 1.5 m combustion chamber at fuel-rich conditions ($\Phi = 1.2$)

The relationship between flame tip distance and velocity over time in a lean combustion environment ($\Phi = 0.8$) within a 1.5-meter-long chamber. The graph reveals the intricate dynamics of the flame as it progresses through the combustion chamber, as illustrated in Figure 5.19

Initial flame front Propagation (up to t_1): Both the flame tip distance (in blue) and velocity (in red) increase initially, indicating a typical acceleration phase after ignition. The flame velocity then experiences a drop, which corresponds to a point of inflection in the distance curve. Periodic Fluctuations (t_1 to t_4): After the initial phase, the flame tip velocity undergoes periodic fluctuations, showing a complex pattern of acceleration and deceleration. These fluctuations are characteristic of the flame's interaction with the chamber's geometry and the flow dynamics within a lean mixture.

The oscillatory velocity pattern suggests the possible formation of tulip flames, where the flame front inverts and then progresses forward again. The vertical dashed lines (t_1 to t_4) may indicate the key moments in the tulip flame life cycle. Velocity Reversals: The negative velocities indicate instances where the flame front actually moves backward, a behavior typical of the tulip flame oscillation phenomenon within confined spaces. Figure 5.20 offers a sequence of visual snapshots capturing the evolution of the flame front within a 1.5-m combustion chamber under lean conditions ($\Phi = 0.8$).

Early Flame Tulip Shape (0.0200 ms – 0.0336 ms): The images show the flame front's initial smooth progression as it begins to elongate and interact with the chamber walls. Development of Instabilities (0.0360 ms – 0.0423 ms): As the flame develops, instabilities become apparent, leading to the formation of a curved flame front that suggests the onset of

tulip flame formation Tulip Flame Formation (0.0447 *ms* – 0.0500 *ms*): The characteristic 'tulip' shape becomes evident, with an indentation forming at the flame front, indicating the complex dynamics of a lean combustion process within a confined space.

Advanced Flame Front Propagation (0.0510 *ms* – 0.0567 *ms*): In the later stages, the flame continues to propagate while exhibiting the tulip shape, oscillating as it interacts with the chamber's geometry and the lean mixture. Figures 5.19 and 5.20 together provide a comprehensive picture of the flame behavior in a lean mixture within a 1.5-*m* chamber. The quantitative analysis of flame tip distance and velocity in Figure 5.19 is visually corroborated by the qualitative representation of flame shapes in Figure 5.20. These figures contribute valuable information for understanding the challenges of optimizing combustion efficiency and stability in lean-burn engines and other industrial applications.

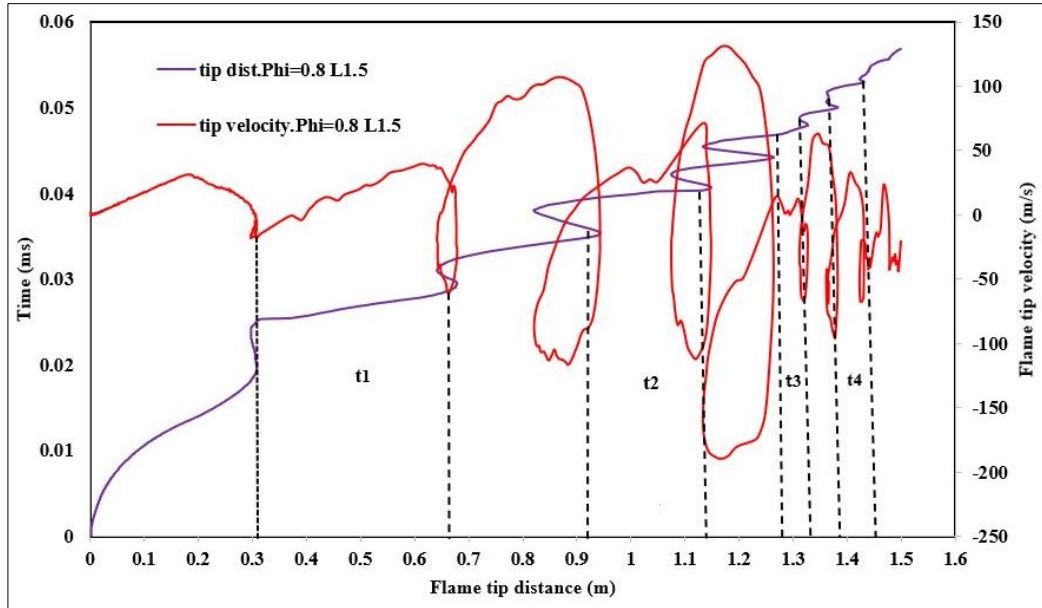


Figure 5.19: Flame tip distance and velocity trends in a lean combustion environment ($\Phi = 0.8$) in a 1.5 m chamber

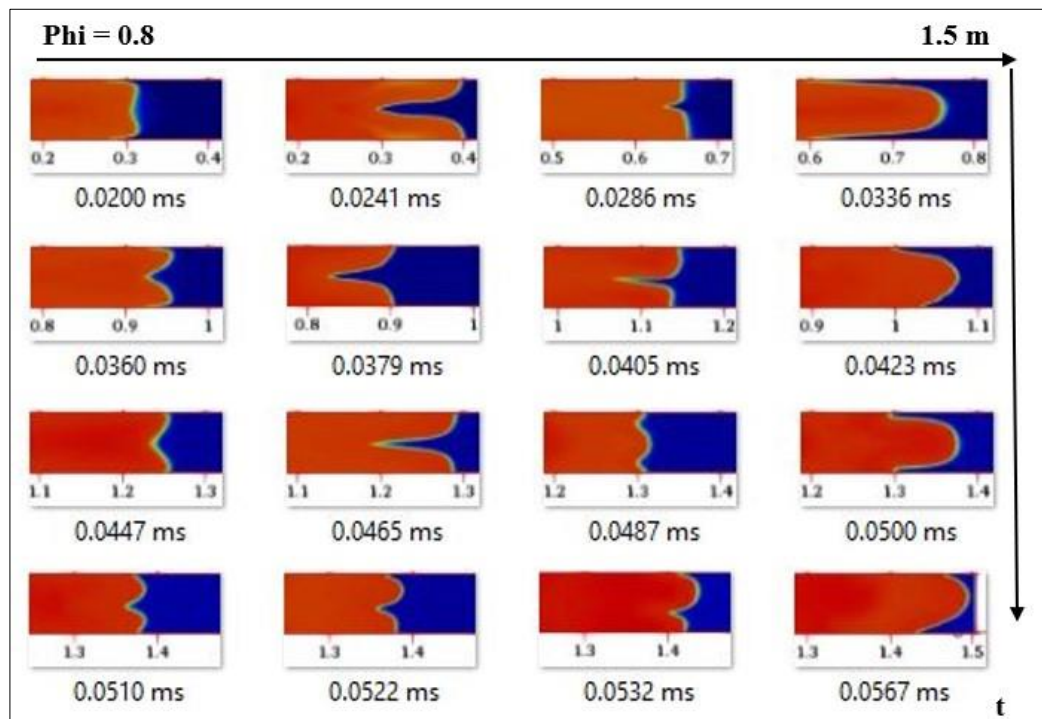


Figure 5.20: Chronological flame shape evolution at lean conditions ($\Phi = 0.8$) in a 1.5 m chamber

5.4.2 Tulip formation behavior of 2 *m* for various *Phi*

A thorough analysis of the influence of equivalence ratio (*phi*) on flame dynamics in a 2 m combustion chamber is presented in Figures 5.21-5.26.

Flame Dynamics in Stoichiometric Conditions (*Phi* = 1) The stoichiometric mixture, with an equivalence ratio of 1, exhibits a balanced fuel-to-air ratio, providing optimal conditions for flame propagation. In a 2 *m* chamber, the flame tip distance increases steadily, indicating a consistent flame front advancement. The velocity profile at stoichiometric conditions shows periodic accelerations and decelerations, which are likely associated with the formation of tulip flames or other flame instabilities due to the interactions between the flame front, combustion products, and fresh mixture. A visual chronology of the flame front (not shown here) would depict a smooth initial progression followed by the formation of instabilities as the flame interacts with the chamber geometry, leading to complex behaviors such as vortex shedding and pressure wave interactions.

Flame Behavior in Fuel-Rich Conditions (*Phi* = 1.2): A fuel-rich mixture (*Phi* = 1.2) in the same 2 *m* chamber length typically results in more pronounced fluctuations in flame tip velocity. This is due to the excess fuel present in the mixture, which can cause more intense combustion events and potentially lead to a more volatile flame front. The distance traveled by the flame tip in a rich mixture is greater, reflecting the increased energy release from the excess fuel. This can result in higher peak velocities and more significant velocity dips as the flame front accelerates and decelerates rapidly. The visual sequence of the flame front under rich conditions would show more dramatic changes in shape and size due to the

more dynamic and energetic combustion process.

Flame Characteristics in Lean Conditions ($\Phi = 0.8$) In contrast, a lean mixture ($\Phi = 0.8$) tends to demonstrate less aggressive flame behavior. The flame tip distance increases more gradually, and the velocity profile is less extreme compared to richer mixtures. Lean mixtures in a 2 m chamber might lead to more stable but slower flame propagation as there is less fuel available to sustain high combustion rates. This can result in a flame that is less prone to the formation of large-scale instabilities and tulip flames. The visual progression of the flame would likely show a more restrained development, with fewer and less intense morphological changes over time, as the limited fuel availability dampens the combustion intensity.

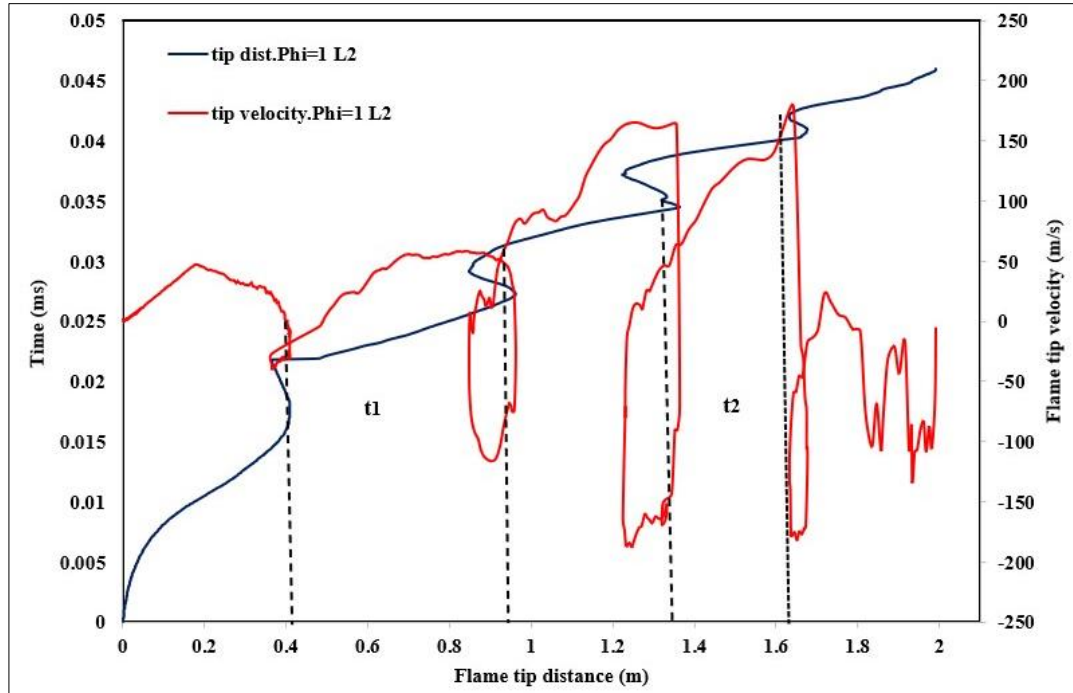


Figure 5.21: Flame tip distance and velocity fluctuations in a stoichiometric mixture in a 2 m chamber, $\phi = 1$

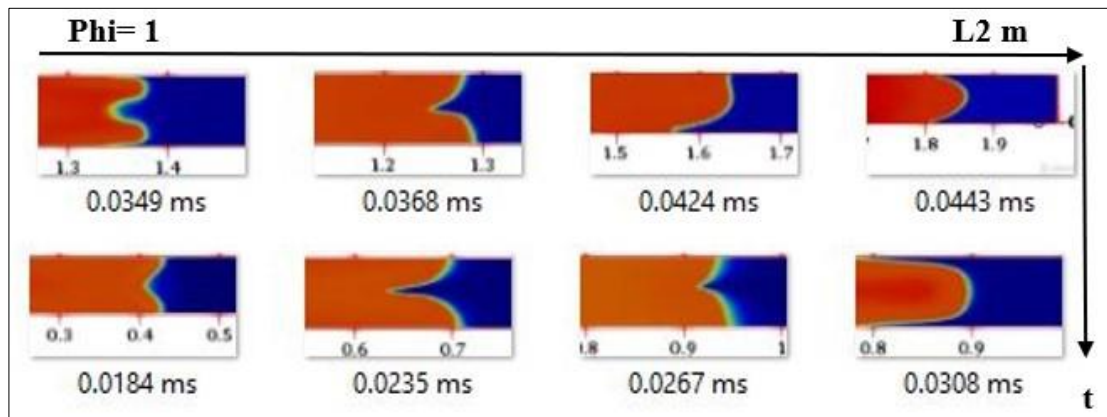


Figure 5.22: Visual chronology of flame front evolution in a stoichiometric mixture in a 2 m chamber, $\phi = 1$

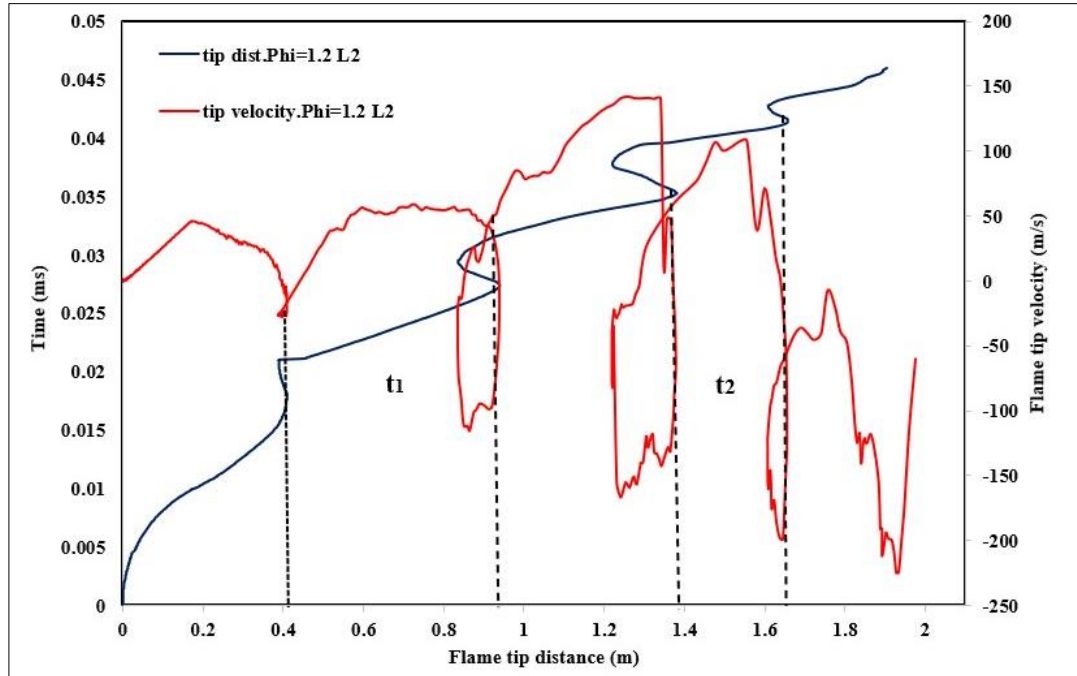


Figure 5.23: Flame tip distance and velocity in a fuel-rich mixture in a 2 m chamber, $\phi = 1.2$

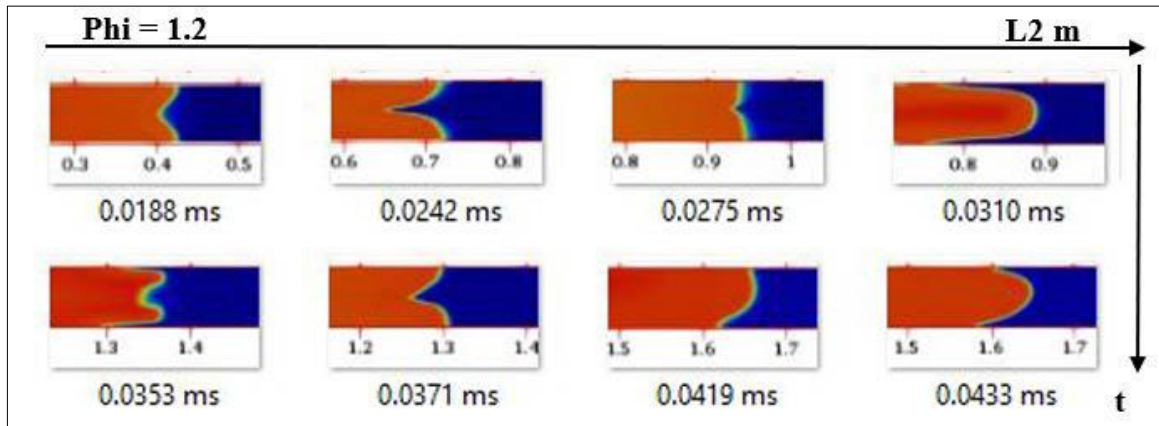


Figure 5.24: Flame shape progression in a fuel-rich mixture in a 2 m chamber, $\phi = 1.2$

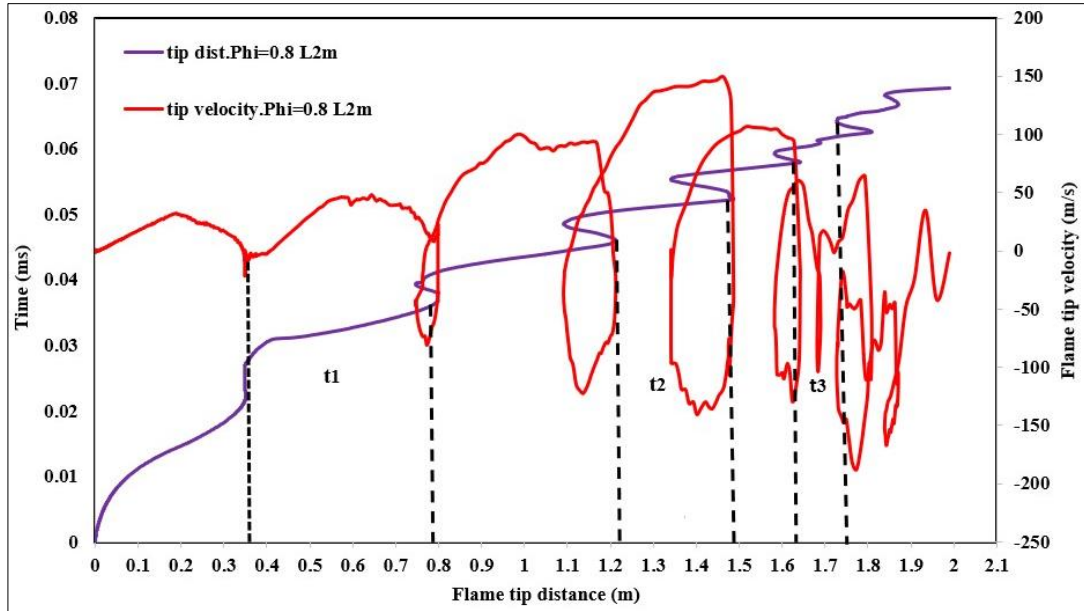


Figure 5.25: Flame tip kinetics in a lean mixture in a 2 m chamber, $\phi = 0.8$

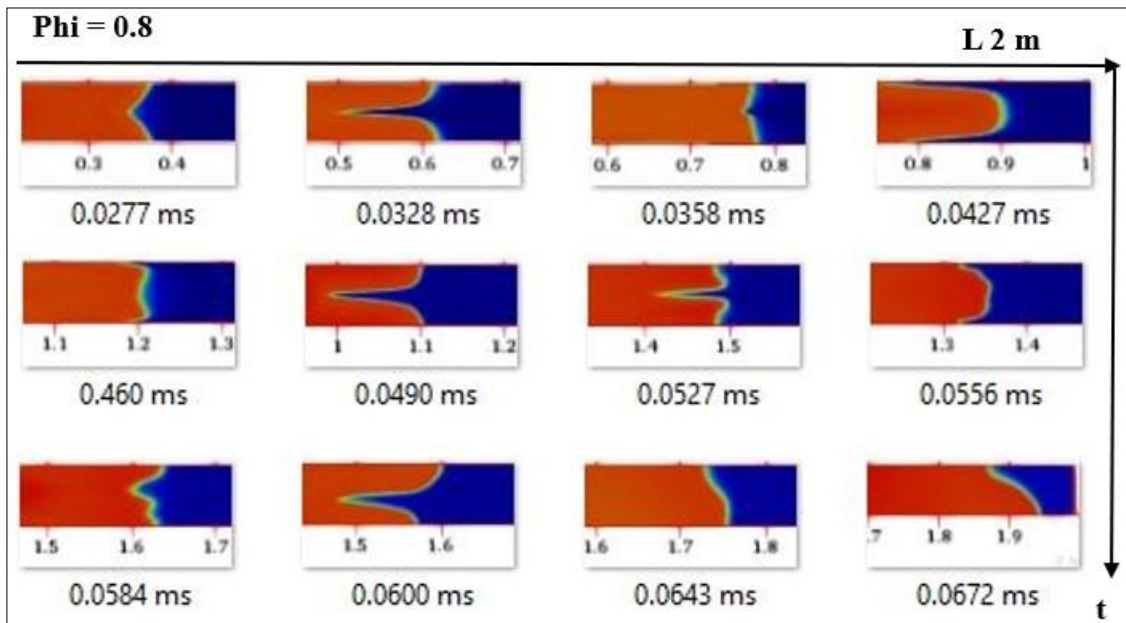


Figure 5.26: Temporal evolution of flame forms in a lean mixture in a 2 m chamber, $\phi = 0.8$

5.4.3 Tulip formation behavior of 1.3 m for various Φ

This sequence of images (Figure 5.27) illustrates the progression of a flame front in a 1.3-meter combustion chamber with a stoichiometric mixture ($\Phi = 1$). The series shows how the flame front evolves, starting

with a smooth curve and progressively transitioning into a more complex shape. This change in shape may signify the initial stages of a tulip flame formation, a common phenomenon in combustion chambers of this size.

The images in Figure 5.28 display the evolution of the flame in a 1.3-*m* chamber with a fuel-rich mixture ($\Phi = 1.2$). Compared to the stoichiometric mixture, the flame in a rich mixture tends to show more pronounced development stages due to the excess fuel, which can lead to different combustion characteristics. The visual progression would reveal how the additional fuel influences flame shape, potentially leading to larger tulip formations and more dynamic behavior.

In Figure 5.29, the progression of a flame front in a lean mixture ($\Phi = 0.8$) within a 1.3-meter chamber is likely captured. In lean conditions, the flame front tends to propagate more slowly due to less available fuel, which could result in less dramatic changes in the flame shape over time. The images would show a gradual and steady flame front advancement, which may not exhibit the pronounced tulip flame shapes seen in stoichiometric or rich mixtures.

Figures (5.27 to 5.29) provide a visual understanding of how different equivalence ratios affect the flame front progression and shape in a 1.3-meter combustion chamber. In stoichiometric conditions, the flame progression is smooth and transitions into moderate complexity. For fuel-rich mixtures, the flame front exhibits more significant changes, reflecting the higher energy released from the excess fuel. In lean conditions, the flame advances more steadily, with less dramatic morphological evolution. These observations are key for designing combustion systems, as they highlight the necessity of tailoring chamber dimensions and operating conditions to the fuel-air mixture to optimize performance and stability.

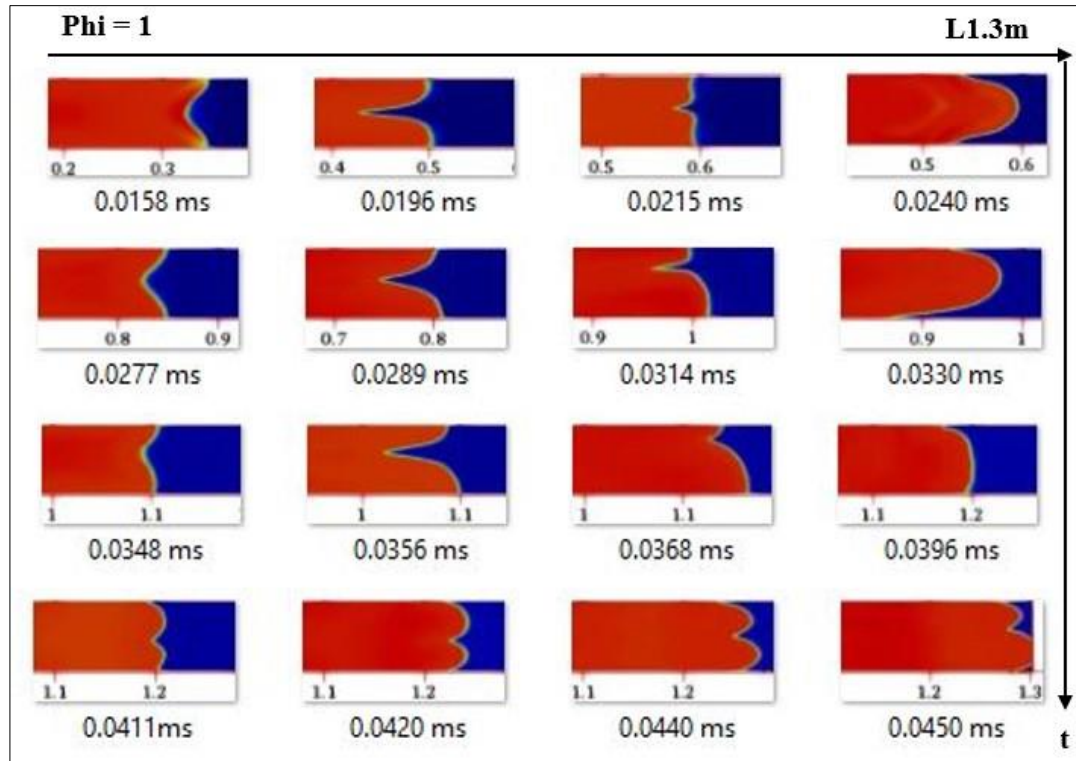


Figure 5.27: Flame front progression in a stoichiometric mixture ($\Phi = 1$) in a 1.3 m combustion chamber

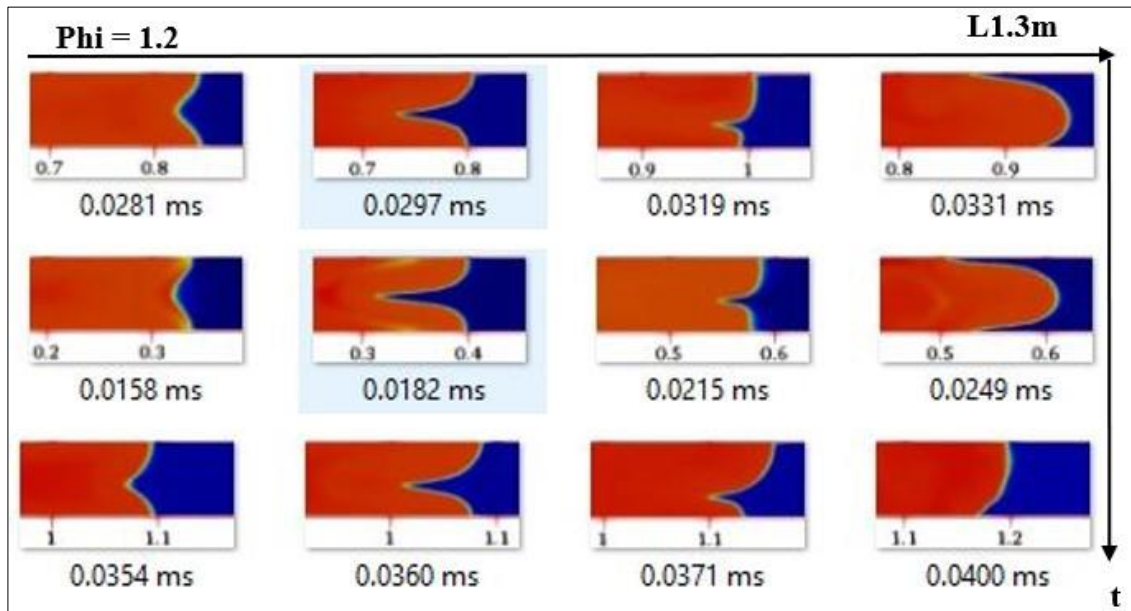


Figure 5.28: Flame development in a fuel-rich mixture ($\Phi = 1.2$) in a 1.3 m chamber

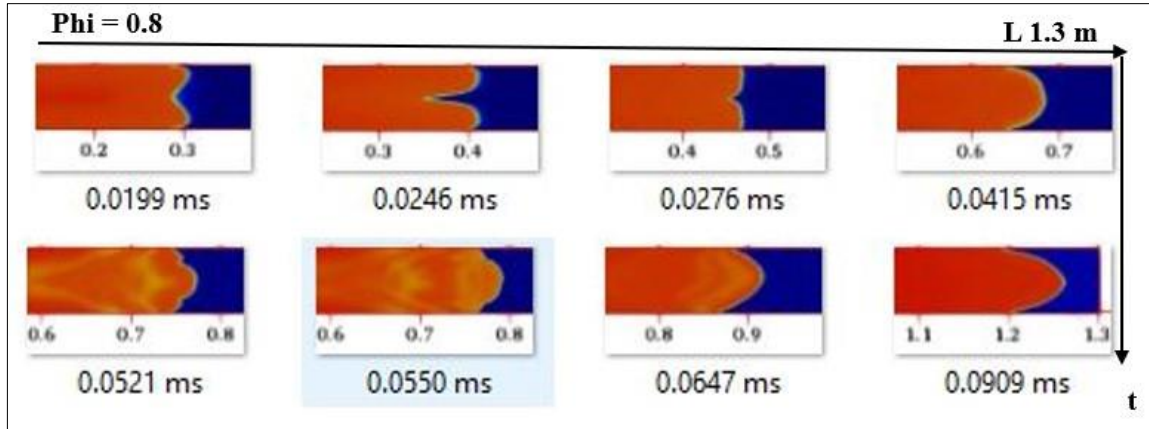


Figure 5.29: Lean combustion flame behavior ($\Phi = 0.8$) in a 1.3 m chamber

5.5 Tulip Formation Contours of Various Lengths for Equivalence Ratio 1.4 (Extra Results)

The frames illustrate the rapid progression and morphological changes of the flame, highlighting the intense and vigorous nature of combustion under these conditions. The flame appears to transition quickly through the stages of growth, likely due to the abundant fuel supply that facilitates an accelerated combustion process. As it appears in Figure 5.30.

In a longer 2-meter chamber, the flame behavior at $\Phi = 1.4$ is visualized through sequential snapshots. The additional space allows the flame to unfold and exhibit pronounced characteristics of rich combustion, such as increased size and potentially more complex behaviors. The elongated chamber might also contribute to visible differences in flame structure compared to the 1.5-m chamber due to variations in flow dynamics and flame-wall interactions. As it appears in Figure 5.31.

The images for a 1.3-meter chamber at $\Phi = 1.4$ likely show a more constrained flame development due to the shorter distance for flame travel. The early frames may show similar initiation and growth phases as the larger chambers, but subsequent frames could reveal how the limited space

affects the flame's ability to develop fully and the possible early onset of stabilizing effects due to the chamber walls. as shown in Figure 5.32.

Across different chamber lengths (1.3 m, 1.5 m, and 2 m), a highly fuel-rich mixture ($\Phi = 1.4$) induces robust flame front propagation, as evidenced by the visual data. The variation in chamber length alters the flame's characteristics, with the longer chamber potentially allowing for more extensive flame development and the shorter chamber leading to a more rapid stabilization of the flame front. These distinctions are crucial for the design and safety considerations of combustion systems, especially when operating in fuel-rich conditions that can influence flame stability, efficiency, and the risk of unwanted combustion phenomena like backdrafts or flash backs.

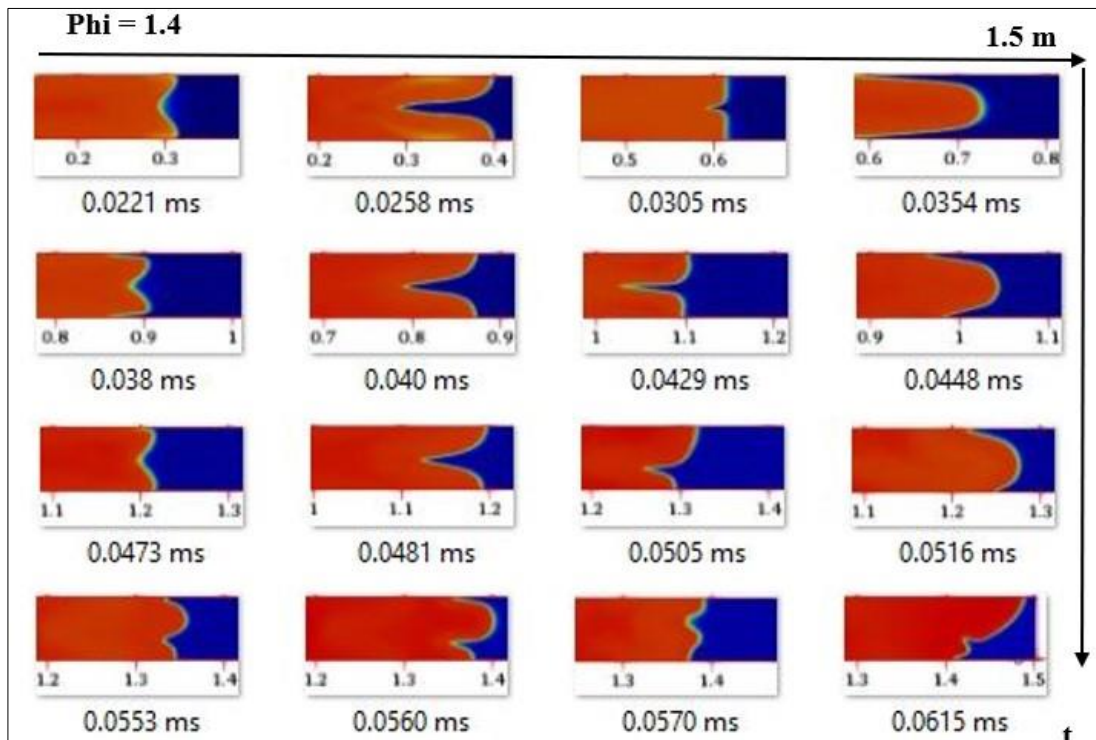


Figure 5.30: Flame propagation in a highly fuel-rich environment ($\Phi = 1.4$) in a 1.5 m combustion chamber

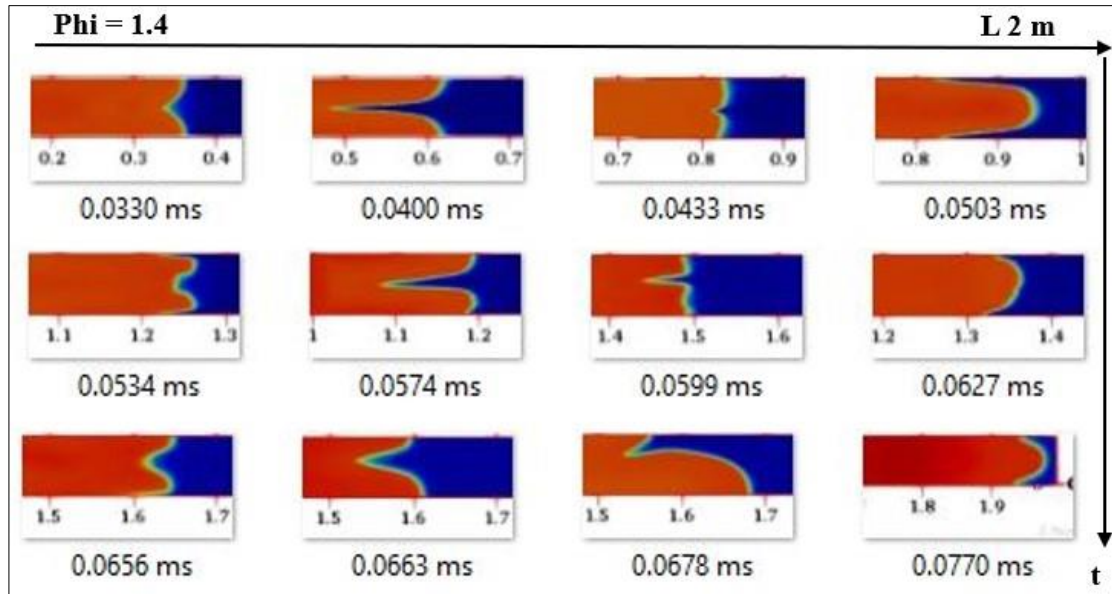


Figure 5.31: Flame dynamics at excessively rich conditions ($\Phi = 1.4$) in a 2 m chamber

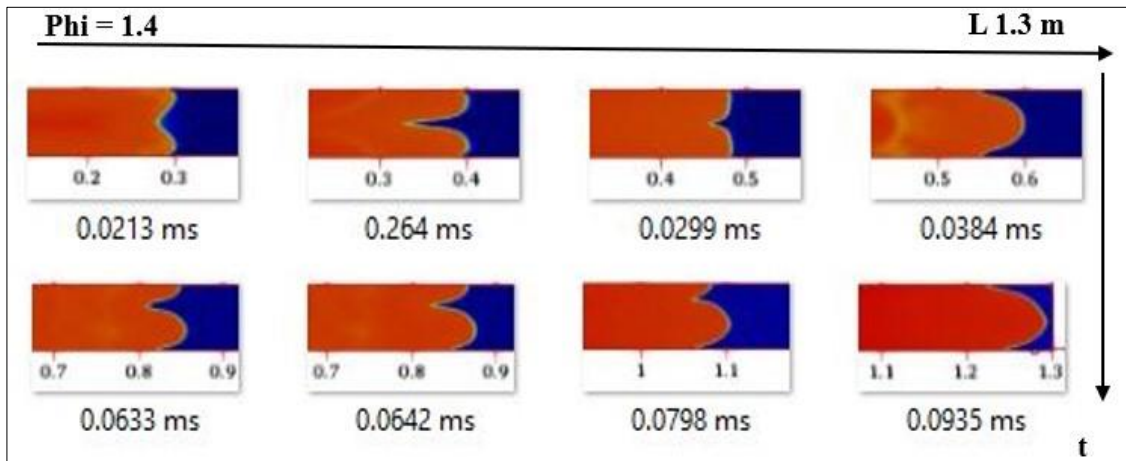


Figure 5.32: Combustion phenomena with excessive fuel ($\Phi = 1.4$) in a 1.3 m chamber

5.6 Experimental Work Visualization

Experimental research is essential for expanding our knowledge of the variety of research and for laying the groundwork for problem-solving and decision-making based on outcomes.

Repetition for enhanced reliability: To ensure the reliability and accuracy of the experimental data, each setup underwent a minimum of five

repeats for each reading. This repetition allowed for the verification of consistency across all experimental runs. Such rigorous testing protocols were crucial in establishing the reliability of the findings and ensuring that the results were representative and reproducible.

An observational overview of experimental results: The experiments yielded intriguing preliminary results. Distinct patterns in flame speed and structure were observed, which varied with changes in the equivalence ratio and pressure settings. These variations offered insights into the combustion efficiency of different fuel-air mixtures. Notably, under certain conditions, there was a transition observed from laminar to turbulent flame propagation. Additionally, significant pressure fluctuations were recorded within the combustion chamber, underscoring the dynamic nature of the combustion process. These observations are invaluable in enhancing the understanding of combustion behavior, particularly in the context of partially premixed LPG and air mixtures, and hold significant implications for optimizing combustion processes in industrial applications.

5.6.1 The effect of equivalent ratio on flame propagation

The effect of an equivalent ratio on flame propagation is an important topic in combustion science and engineering. The equivalent ratio is the ratio of the actual fuel-air ratio to the stoichiometric fuel-air ratio for a given fuel mixture. It indicates how rich or lean the mixture is and affects the ignition, stability, speed, and structure of the flame (Amaludin et al., 2022; Yao et al., 2020).

likely presents Figure 5.33, a side-by-side comparison of numerical simulation and experimental visualization of flame propagation at the early stages in a stoichiometric mixture. The top row might show experimental captures, while the bottom row probably represents numerical simulations.

The visual similarity between the two rows suggests that the numerical model captures key aspects of the flame behavior observed experimentally, such as flame shape and propagation rate.

The comparison might focus on a fuel-rich mixture. The top images, presumably from experiments, and the bottom images from numerical simulations demonstrate the changes in flame morphology due to excess fuel. The correspondence between the numerical results and the experimental data would indicate the effectiveness of the simulation in capturing the richer flame dynamics, which typically involve more complex and vigorous burning, as shown in Figure 5.34.

Figure 5.35 contrasts the flame behavior in a lean mixture, with the potential top row displaying experimental results and the bottom row showing numerical simulations. The lean mixture's slower propagation and less pronounced flame development compared to richer mixtures would be evident in both sets of images. A close match between the two would validate the numerical model's accuracy in representing the subtler characteristics of lean flame propagation.

Across Figures 5.33 to 5.35, there is a comparison between numerical simulations and experimental visualizations of flame propagation for different equivalence ratios. The consistent agreement between the simulated and experimental images across various mixture conditions underscores the robustness of the numerical model. This level of correlation is significant for validating computational fluid dynamics (CFD) models used in predicting and optimizing combustion processes in practical applications, ranging from internal combustion engines to industrial furnaces.

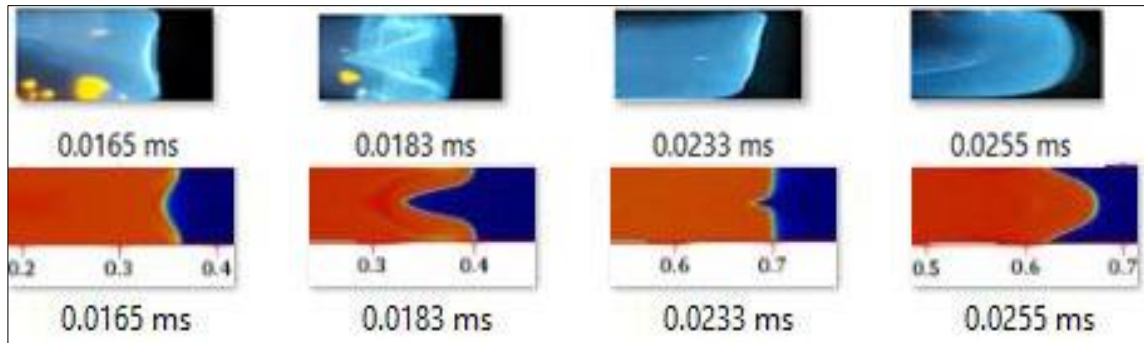


Figure 5.33: Comparative analysis of early flame propagation in a stoichiometric mixture ($\Phi = 1$)

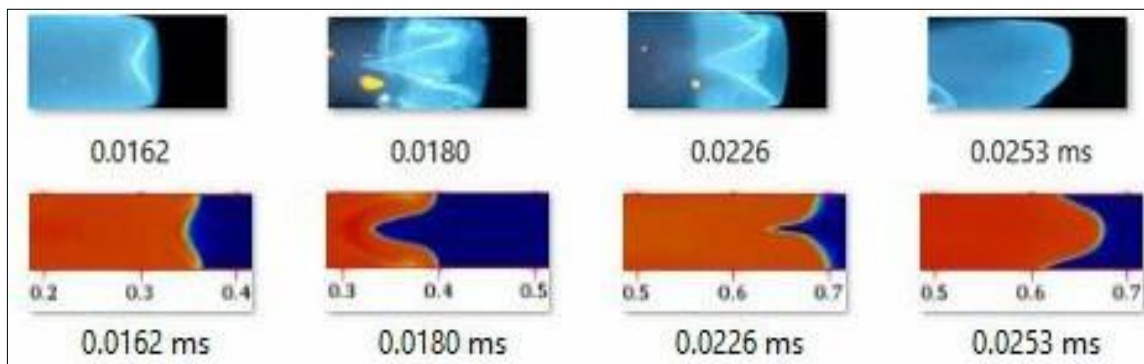


Figure 5.34: Numerical and experimental visualization correlation for fuel-rich flame propagation ($\Phi = 1.2$)

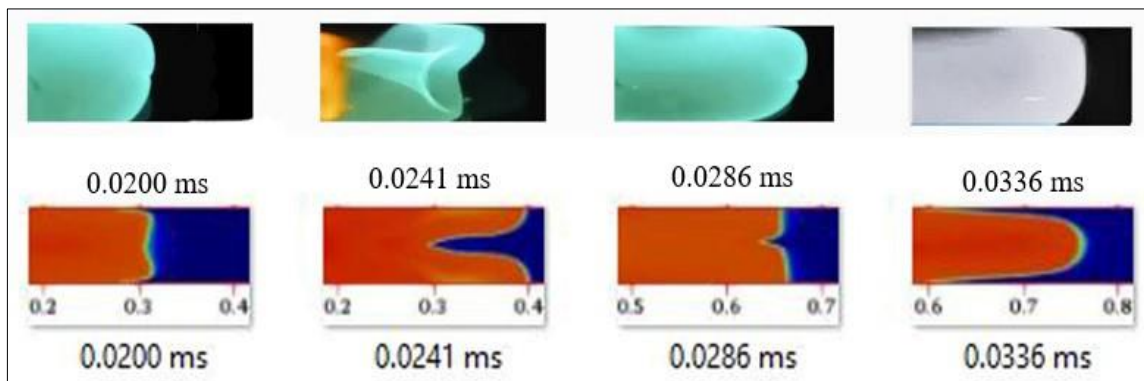


Figure 5.35: Lean combustion flame dynamics ($\Phi = 0.8$) between simulations and experiments

5.6.2 The dynamic visualization of flame propagation

The dynamic visualization of flame propagation is a technique that allows us to observe and analyze the shape, speed, and structure of flames as they propagate in different environments. It can help us understand the factors that affect flame behavior, such as the fuel type, the mixture ratio, the ignition source, and the turbulence (Chengeng & Mikhail, 2023; Clanet & Searby, 1996; Issayev et al., 2022; Liberman et al., 2022).

The comparison between the numerical findings and the experimental data, as shown in. The data demonstrates a strong correlation between the position and velocity of the flame in the first 32 *ms*, prior to the creation of the tulip flame. This suggests that the model accurately represents the progression of the tulip flame. Nevertheless, from the tulip flame zone onwards until $t = 54$ *ms*, the computational findings show a significant underestimation of the actual data. The observed disparities between the numerical and experimental outcomes may be ascribed to turbulence generated in the unburned mixture by the increasing flame. Turbulence has a substantial impact on the dynamics of flame propagation, causing fluctuations in both the speed and behavior of the flame. The turbulence caused by the spreading flame might affect the flame's movement beyond the tulip flame area, resulting in the discrepancies reported between the computer forecasts and experimental observations. Additional research and revisions of the numerical model are required in order to enhance its accuracy and effectively represent the features of flame propagation. To improve the accuracy of the model in predicting the complete flame propagation process, it would be beneficial to include a more extensive analysis of turbulence in the simulation as shown in Figure 5.36.

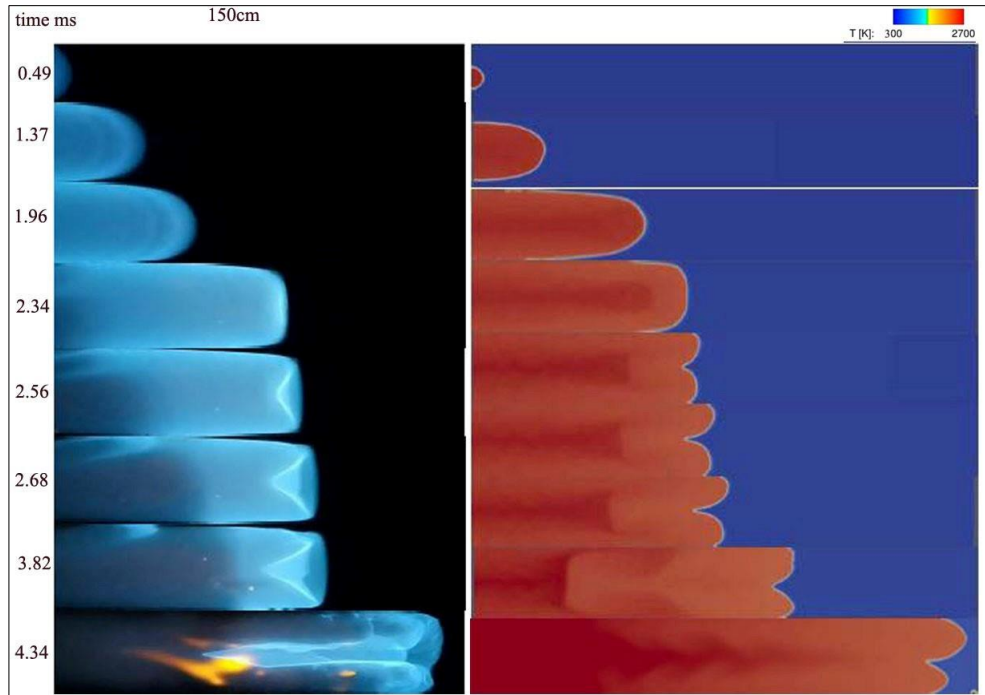


Figure 5.36: High-speed camera images in the present study for flame propagation

5.6.3 Tulip formation of experimental visualization

Figure 5.37 clearly depicts the observed variations in the flame dynamics when exposed to a somewhat fuel-rich mixture. The flame's velocity exhibits non-uniformity and periodic variations, like a "leap frog" motion. The film shows that after the start, the combustion reaction produces a flame that initially takes on a spherical shape. This flame then goes through various stages that involve the development and movement of the flame, as explained earlier. The complex characteristics of this process underscore the need of studying the spread of flames in enclosed spaces, such as tubes. The statement emphasizes the need to perform extensive study in order to fully understand the intricacies of flame dynamics in these specific conditions (Illacanchi et al., 2023; Movahedi, 2017).

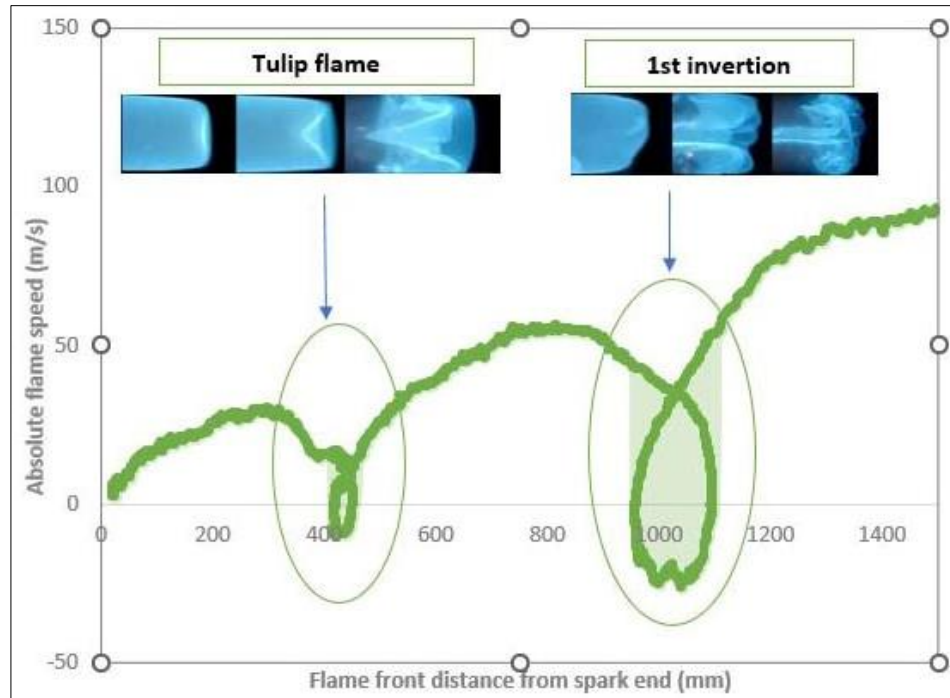


Figure 5.37: Changes of absolute flame speed along the tube center-line versus flame front distance from spark

CHAPTER SIX
CONCLUSIONS AND
RECOMMENDATIONS

CHAPTER SIX

CONCLUSIONS AND RECOMMENDATIONS

6.1 Conclusions

The $k-\varepsilon$ model accurately predicted the flame speed with less than a 10% maximum inaccuracy. Other turbulence models, such as the Launder Sharma $k - \varepsilon$ model, underestimate flame speed. The $k-\varepsilon$ model beat the other models for peak pressures, with an average inaccuracy of 11.9%, due to the absence of energy loss in the simulated pipe. The qualitative comparison of tulip flame creation revealed acceptable agreement between experimental and numerical results, supporting the usefulness of the turbulent flame model in capturing the main elements of the tulip flame phenomenon.

- 1) The study concluded that the $k - \varepsilon$ model is suitable and accurate for simulating the combustion process of Iraqi liquefied petroleum gas in pipes, especially in capturing the flame speed and the dynamics of tulip flame formation. However, further investigations and model refinements are warranted to address the discrepancies in tulip flame predictions and better understand the impact of turbulence on flame propagation dynamics.
- 2) Longer pipes occasionally exhibit higher velocity values than shorter ones, suggesting localized acceleration of the gas flow due to cumulative energy dissipation.
- 3) Although vertical velocity components have low or no variation for shortened periods of time, vertical velocity has more significant variations, indicating the presence of turbulent flow phenomena like vortices within the pipe.

- 4) Temperature variations occur with different pipe lengths, indicating the influence of pipe geometry and heat transfer on flame behavior. The temperature distribution reveals different phases of combustion, including the ignition and combustion initiation phases and flame propagation.
- 5) Longer pipe lengths generally result in higher burning velocities due to increased residence time and more complete combustion. a progressive combustion process with a more vigorous combustion reaction as time progresses, the burning velocity is non-linear, with a more pronounced rise observed at later time intervals.
- 6) At earlier time intervals, the reaction amount is consistently high, indicating sustained combustion efficiency. However, at later time intervals, it starts to decrease, suggesting less efficient combustion.

6.2 Recommendations

- 1) Confined Combustion Systems: Investigate flame propagation behavior in confined spaces, like ducts, tubes, or channel rooms closed from both sides, which are commonly encountered in industrial applications. Understand the impact of confinement on flame structure, propagation speed, and tulip generation to optimize combustion efficiency and safety.
- 2) Influence of Varying Parameters: Investigate the influence of varying parameters, such as the effect of initial conditions (temperature, pressure), on flame propagation and tulip generation. Understand how these factors affect flame behavior in real-world scenarios and under different operating conditions.
- 3) Combustion Instabilities: Study the role of flame propagation

mechanisms in the occurrence of combustion instabilities, such as flame flashback and flame lift-off. Investigate how these phenomena influence tulip flame formation and development.

- 4) Investigate the flame propagation and tulip flame formation behaviors of alternative fuels. This research is crucial as the world transitions towards cleaner energy sources, and understanding the combustion characteristics of these fuels is essential for their practical application.
- 5) Focus on practical applications, such as internal combustion engines, gas turbines, and industrial furnaces. Investigate how flame propagation mechanisms and tulip generation affect the performance and efficiency of these systems, aiming to optimize their operation.
- 6) Flame Stability: Study flame stability in different fuel-to-air ratio regimes and investigate the impact of flow conditions, turbulence, flame interactions, and tulip flame formation on the stability of combustion processes

REFERENCES

REFERENCES

AD Number, S. (1980). *AD234626, NEW LIMITATION CHANGE*. chrome-extension://efaidnbmnnnibpcajpcglclefindmkaj/https://www.acgsc.org/history/BU%20AER%20Series/Methods%20of%20Design%20and%20Evaluation%20of%20Interceptor%20Fire%20Control%20System.pdf

Aghaabbasi, O. (2021). *CFD-Simulations of inhomogeneous air explosions* University of South-Eastern Norway, Faculty of Technology, Natural sciences and Maritime Sciences].

Akkerman, V. y., & Law, C. K. (2013). Flame dynamics and consideration of deflagration-to-detonation transition in central gravitational field. *Proceedings of the Combustion Institute*, 34(2), 1921-1927.

Al-Dulaimi, Z. (2017). *Non-aqueous shale gas recovery system* Cardiff University].

Al-Malki, F. (2013). Numerical simulation of the influence of partial premixing on the propagation of partially premixed flames. *Computers & Mathematics with Applications*, 66(3), 279-288.

Amaludin, N., Morrow, M., Woolley, R., & Amaludin, A. (2022). Methane hydrogen laminar burning velocity blending laws in horizontal open-ended flame tube rig. *IOP Conference Series: Materials Science and Engineering*,

Arpaia, F. (2019). *Laminar flame speed prediction for Natural Gas/Hydrogen blends and application to the combustion modeling in IC Engines* Politecnico di Torino].

Avhad, S. V. (2020). Study on dependence of Cavitation number on Supercavitation phenomenon using Transient Multiphase Analysis. *International Journal of Scientific Development and Research (IJS DR)*, 5(7), 709-715.

Ax, H., & Meier, W. (2016). Experimental investigation of the response of

laminar premixed flames to equivalence ratio oscillations. *Combustion and Flame*, 167, 172-183.

Ballester, J., & García-Armingol, T. (2010). Diagnostic techniques for the monitoring and control of practical flames. *Progress in Energy and Combustion Science*, 36(4), 375-411.

Balusamy, S., Cessou, A., & Lecordier, B. (2009). Measurement of laminar burning velocity—A new PIV approach. Proceedings of the European Combustion Meeting, Saint Etienne du Rouvray cedex, France

Beretta, G. P., Rashidi, M., & Keck, J. C. (1983). Turbulent Flame Propagation and Combustion in Spark Ignition Engines *Combustion and Flame*, 52, 217-245

bin Amaludin, N. A., Woolley, R., Ebieta, C., Amaludin, A. E., & bin Amaludin, H. Z. (2022). Thermoacoustic analysis of premixed methane–hydrogen flames in open-ended tubes. *Fuel*, 325, 124892.

Bussing, T., & Pappas, G. (1994). An introduction to pulse detonation engines. 32nd Aerospace Sciences Meeting and Exhibit, Reno, NV, U.S.A.

Bychkov, V., Akkerman, V. y., Fru, G., Petchenko, A., & Eriksson, L.-E. (2007). Flame acceleration in the early stages of burning in tubes. *Combustion and Flame*, 150(4), 263-276.

Bychkov, V., & Liberman, M. A. (2000). Dynamics and stability of premixed flames. *Physics reports*, 325(4-5), 115-237.

Chen, P., Sun, R., Li, L., & Wang, Y. (2023). Experimental observation of premixed methane/air flame propagation in an obstructed tube with increasing blockage ratios. *Journal of Energy Resources Technology*, 145(2), 022303.

Chengeng, Q., & Mikhail, A. L. (2023). On the mechanism of "tulip flame" formation: the effect of ignition sources. *Tulip flame formation*, 1-37.

Chigier, N. (1991). *Combustion measurements*. CRC Press.

- Cho, J. H., & Lieuwen, T. (2005). Laminar premixed flame response to equivalence ratio oscillations. *Combustion and Flame*, 140(1-2), 116-129.
- Clanet, C., & Searby, G. (1996). On the “tulip flame” phenomenon. *Combustion and Flame*, 105(1-2), 225-238.
- Cloney, C. T., Ripley, R. C., Pegg, M. J., & Amyotte, P. R. (2018). Laminar burning velocity and structure of coal dust flames using a unity Lewis number CFD model. *Combustion and Flame*, 190, 87-102.
- Desmond, E., & Turan, A. (2015). *Advanced Thermodynamics for Engineers* (Second ed.). Elsevier Ltd.
- Dold, J., & Joulin, G. (1995). An evolution equation modeling inversion of tulip flames. *Combustion and Flame*, 100(3), 450-456.
- Dunn-Rankin, D., & Sawyer, R. F. (1998). Tulip flames: changes in shape of premixed flames propagating in closed tubes. *Experiments in fluids*, 24, 130-140.
- Ehsan, Y. (2010). *Tutorial XiFoam: Version: OpenFOAM-1.7.x*. chrome-extension://efaidnbnmnnibpcajpcgiclfndmkaj/https://www.tfd.chalmers.se/~hani/kurser/OS_CFD_2010/ehsanYasari/ehsanYasariReport.pdf
- Ellis, O. d. C. (1928). Flame movement in gaseous explosive mixtures. *J. Fuel Sci.*, 7, 502-508.
- Foss, J. F. (2004). Surface selections and topological constraint evaluations for flow field analyses. *Experiments in fluids*, 37, 883-898.
- Gamil, A. A., Nikolaidis, T., Lelaj, I., & Laskaridis, P. (2020). Assessment of numerical radiation models on the heat transfer of an aero-engine combustion chamber. *Case Studies in Thermal Engineering*, 22, 100772.
- Gonzalez, M., Borghi, R., & Saouab, A. (1992). Interaction of a flame front with its self-generated flow in an enclosure: The “tulip flame” phenomenon. *Combustion and Flame*, 88(2), 201-220.

- Greenshields, C. (2021). *OpenFOAM v9 User Guide*. <https://doc.cfd.direct/openfoam/user-guide-v9>
- Greenshields, C. J. (2020). *OpenFoam Users Guide, Version 7.1*. <https://www.scirp.org/reference/referencespapers?referenceid=3200086>
- Guénoche, H. (1964). Flame propagation in tubes and in closed vessels. In *AGARDograph* (Vol. 75, pp. 107-181). Elsevier.
- Han, Z., & Reitz, R. D. (1995). Turbulence modeling of internal combustion engines using RNG κ - ϵ models. *Combustion science and technology*, 106(4-6), 267-295.
- Hanford, J. W., Koomey, J. G., Stewart, L. E., Lecar, M. E., Brown, R. E., Johnson, F. X., Hwang, R. J., & Price, L. K. (1994). *BASELINE DATA FOR THE RESIDENTIAL SECTOR AND DEVELOPMENT OF A RESIDENTIAL FORECASTING DATABASE* Lawrence Berkeley Laboratory, University of California
- Hariharan, A. (2016). *Development and propagation of premixed and diffusion flames in confined channels* [Michigan State University].
- Hariharan, A., & Wichman, I. S. (2014). Premixed flame propagation and morphology in a constant volume combustion chamber. *Combustion science and technology*, 186(8), 1025-1040.
- Huth, M., & Heilos, A. (2013). Fuel flexibility in gas turbine systems: impact on burner design and performance. In *Modern Gas Turbine Systems* (pp. 635-684). Elsevier.
- Ibrahim, A. S., Abdalwahab, M. A., Abulaban, O. S., & Ahmed, S. F. (2015). Investigation of Laminar Flame Speeds of Methane-LPG Air Mixtures. Proceedings of the 4th International Gas Processing Symposium, Qatar.
- Ilbas, M. (2005). The effect of thermal radiation and radiation models on hydrogen–hydrocarbon combustion modelling. *International journal of*

hydrogen energy, 30, 1113-1126.

Illacanchi, F., Valencia, S., Celis, C., Mendiburu, A., Bravo, L., & Khare, P. (2023). Numerical Study of Distorted Tulip Flame Propagation in Confined Systems. *arXiv:2309.05893*, 1-13.

Insidoro, M. (1992). COMBUSTION THERMODYNAMICS. In *Thermodynamic Basics and Applications* (pp. 1-16).

Issayev, G., Giri, B. R., Elbaz, A. M., Shrestha, K. P., Mauss, F., Roberts, W. L., & Farooq, A. (2022). Ignition delay time and laminar flame speed measurements of ammonia blended with dimethyl ether: a promising low carbon fuel blend. *Renewable Energy*, 181, 1353-1370.

Jang, H. J., Jang, G. M., & Kim, N. I. (2019). Unsteady propagation of premixed methane/propane flames in a mesoscale disk burner of variable-gaps. *Proceedings of the Combustion Institute*, 37(2), 1861-1868.

Kadem, H. M. M. (2021). *Experimental and Numerical Study of the effect of Iraqi Liquefied Petroleum Gas (ILPG) on flame propagation speed* College of Engineering, University of Babylon, Mechanical Engineering, Power Mechanics].

Kaltayev, A., Riedel, U., & Warnatz, J. (2000). The hydrodynamic structure of a methane-air tulip flame. *Combustion science and technology*, 158(1), 53-69.

KERAMPRAN, S., DESBORDES, D., & VEYSSIÈRE, B. (2000). Study of the Mechanisms of Flame Acceleration in a Tube of Constant Cross Section. *Combustion Science and Technology*, 158(1), 71-91.

Kerampran, S., Desbordes, D., & Veyssièrè, B. (2001). Propagation of a flame from the closed end of a smooth horizontal tube of variable length. *Proceedings of the 18th ICDERS*,

Kerampran, S., Desbordes, D., & Veyssièrè, B. (2001). Propagation of a

Flame from the Closed End of a Smooth Horizontal Tube of Variable Length
Proceedings of the 18th ICDERS.,

Kerampran, S., Desbordes, D., Veyssi re, B., & Bauwens, L. (2001). Flame propagation in a tube from closed to open end. 39th Aerospace Sciences Meeting and Exhibit, Reno, NV, U.S.A.

Krastev, V. K., Silvestri, L., & Falcucci, G. (2017). A modified version of the RNG k - ϵ turbulence model for the scale-resolving simulation of internal combustion engines. *Energies*, *10*, 2116.

Kumar, S. (2011). Numerical studies on flame stabilization behavior of premixed methane-air mixtures in diverging mesoscale channels. *Combustion science and technology*, *183*(8), 779-801.

Kutkan, H., & Guerrero, J. (2021). Turbulent premixed flame modeling using the algebraic flame surface wrinkling model: A comparative study between OpenFOAM and ansys fluent. *Fluids*, *6*(12), 462.

la Cruz- vila, D., Le n-Ruiz, D., Carvajal-Mariscal, I., Polupan, G., & Sigalotti, L. D. G. (2020). Luminous Flame Height Correlation Based on Fuel Mass Flow for a Laminar to Transition-to-Turbulent Regime Diffusion Flame. *arXiv:2008.12209*, 22.

Li, Y. Z., Huang, C., Anderson, J., Svensson, R., Ingason, H., Husted, B., Runefors, M., & Wahlqvist, J. (2017). *Verification, validation and evaluation of FireFOAM as a tool for performance design*.
<https://urn.kb.se/resolve?urn=urn:nbn:se:ri:diva-32870>

Liberman, M., Kuznetsov, M., Ivanov, A., & Matsukov, I. (2009). Formation of the preheated zone ahead of a propagating flame and the mechanism underlying the deflagration-to-detonation transition. *Physics Letters A*, *373*(5), 501-510.

Liberman, M. A., Qian, C., & Wang, C. (2022). On the formation of a tulip

flame in closed and semi-open tubes. *arXiv:2209.00709*, 1-44.

Londoño, L. F., López, C. E., Cadavid, F., & Burbano, H. (2013). Determination of laminar flame speed of methane-air flames at subatmospheric conditions using the cone method and ch^* emission. *Dyna*, 80(180), 130-135.

Magnussen, B. F., & Hjertager, B. H. (1977). On mathematical modeling of turbulent combustion with special emphasis on soot formation and combustion. *Symposium (international) on Combustion*, 16(1), 719-729.

Mallard, E., & Le Chatelier, H. (1883). Sur les lampes de surete a propos des recentes experiences de. *Annales des Mines, Mallard, Le-Chatelier, France*, 3, 35-68.

Markstein, G. H. (2014). *Nonsteady flame propagation: AGARDograph*. Elsevier.

Marra, F. S., & Continillo, G. (1996). Numerical study of premixed laminar flame propagation in a closed tube with a full Navier-Stokes approach. *Symposium (International) on Combustion*, 26(1), 907-913.

Matalon, M., & Metzener, P. (1997). The propagation of premixed flames in closed tubes. *Journal of Fluid Mechanics*, 336, 331-350.

McAllister, S., Chen, J.-Y., & Fernandez-Pello, A. C. (2011). *Fundamentals of combustion processes*. Springer New York, NY.

Metzener, P., & Matalon, M. (2001). Premixed flames in closed cylindrical tubes. *Combustion Theory and Modelling*, 5(3), 463.

Mjbel, H. M., Abdulhaleem, S. M., & Shahad, H. A. (2021). A Numerical And Experimental Analysis Of Laminar Flame Speed For Pre-Mixed Iraqi Lpg/Air Mixture In A Horizontal Cylindrical Combustion Chamber. *Journal of Mechanical Engineering Research and Developments*, 44(1), 176-189.

Movahedi, Z. (2017). *An Investigation of Premixed Flame Propagation in a Straight Rectangular Duct* University of Windsor (Canada)].

N'konga, B., Fernandez, G., Guillard, H., & CERMICS, B. L. (1993). Numerical investigations of the tulip flame instability—comparisons with experimental results. *Combustion science and technology*, 87(1-6), 69-89.

Park, O., Veloo, P. S., Liu, N., & Egolfopoulos, F. N. (2011). Combustion characteristics of alternative gaseous fuels. *Proceedings of the Combustion Institute*, 33(1), 887-894.

Paulasalo, J. (2019). *CFD modelling of industrial scale gas flame with OpenFOAM software* LAPPEENRANTA UNIVERSITY OF TECHNOLOGY, LUT School of Energy Systems, Degree Programme in Energy Technology].

Perry, A. E., & Chong, M. S. (1987). A description of eddying motions and flow patterns using critical-point concepts. *Annual Review of Fluid Mechanics*, 19, 125-155.

Pizza, G., Frouzakis, C. E., Mantzaras, J., Tomboulides, A. G., & Boulouchos, K. (2010). Three-dimensional simulations of premixed hydrogen/air flames in microtubes. *Journal of Fluid Mechanics*, 658, 463-491.

Povilaitis, M., & Jaseliūnaitė, J. (2021). Simulation of hydrogen-air-diluent mixture combustion in an acceleration tube with FlameFoam solver. *Energies*, 14(17), 5504.

Rahim, F., Kian, F., Parsinejad, F., ANDREWS, R., & Metghalchi, H. (2008). A thermodynamic model to calculate burning speed of methane-air-diluent mixtures. *International Journal of Thermodynamics*, 11(4), 151-160.

Rajput, E. R. K. (2008). *A Textbook of International Combustion Engines* (Third ed.). LAXMI PUBLICATIONS (P) LTD.

Rashwan, S. S., Ibrahim, A. H., Abou-Arab, T. W., Nemitallah, M. A., & Habib, M. A. (2017). Experimental study of atmospheric partially premixed oxy-combustion flames anchored over a perforated plate burner. *Energy*, 122, 159-167.

Richardson, E. S., & Chen, J. H. (2017). Analysis of turbulent flame propagation in equivalence ratio-stratified flow. *Proceedings of the Combustion Institute*, 36(2), 1729-1736.

Rusdin, A. (2017). Computation of turbulent flow around a square block with standard and modified k- ϵ turbulence models. *International Journal of Automotive and Mechanical Engineering*, 14(1), 3938-3953.

Said, Z., Assad, M. E. H., Hachicha, A. A., Bellos, E., Abdelkareem, M. A., Alazaizeh, D. Z., & Yousef, B. A. (2019). Enhancing the performance of automotive radiators using nanofluids. *Renewable and Sustainable Energy Reviews*, 112, 183-194.

Salamandra, G., Bazhenova, T., & Naboko, I. (1958). Formation of detonation wave during combustion of gas in combustion tube. *Symposium (International) on Combustion*, 7(1), 851-855.

Samantaray, B. B., & Mohanta, C. K. (2015). Analysis of industrial flame characteristics and constancy study using image processing technique. *Journal of Mechanical Engineering and Sciences*, 9, 1604-1613.

Siba, P. C., & Ratan, J. (2018). EXPERIMENTAL STUDY ON PREMIXED LPG-AIR FLAME PROPAGATION IN A RECTANGULAR CHANNEL. Proceedings of the 2nd National Aero Propulsion Conference NAPC, IIT Kharagpur, West Bengal.

Spalding, D. (1971). Mixing and chemical reaction in steady confined turbulent flames. *Symposium (International) on combustion*, 13(1), 649-657.

Starke, R., & Roth, P. (1989). An experimental investigation of flame behavior during explosions in cylindrical enclosures with obstacles. *Combustion and Flame*, 75(2), 111-121.

Strasser, W., & Chamoun, G. (2014). Wall temperature considerations in a two-stage swirl non-premixed furnace. *Progress in Computational Fluid*

Dynamics, an International Journal, 14(6), 386-397.

Taniyama, Y., & Fujita, O. (2014). Initiation and formation of the corrugated structure leading to the self-turbulization of downward propagating flames in a combustion tube with external laser absorption. *Combustion and Flame*, 161(6), 1558-1565.

Tecplot. (2013). *Tecplot.360 User Manual*. Tecplot Inc.

Tewarson, A., & Khan, M. M. (1988). FLAME PROPAGATION FOR POLYMERS IN CYLINDRICAL

CONFIGURATION AND VERTICAL ORIENTATION. *Twenty-Second Symposium (International) on Combustion/The Combustion Institute*,, 1231-1240

Viskanta, R., & Mengüç, M. (1987). Radiation heat transfer in combustion systems. *Progress in Energy and Combustion Science*, 13, 97-160.

Wang, B., Qiu, R., & Jiang, Y. (2008). Effect of adding hydrogen on LPG/air premixed flame structure *Chinese Science and Technology Journal Database*(7), 1137-1142.

Wierzba, I., & Wang, Q. (2006). The flammability limits of H₂-CO-CH₄ mixtures in air at elevated temperatures. *International journal of hydrogen energy*, 31(4), 485-489.

Williams, F. A. (2018). *Combustion Theory: The Fundamental Theory of Chemically Reacting Flow Systems* CRC Press.

Xiao, H. (2016). Numerical Simulations of Dynamics of Premixed Hydrogen-Air Flames Propagating in Ducts. In *Experimental and Numerical Study of Dynamics of Premixed Hydrogen-Air Flames Propagating in Ducts* (pp. 71-105). Springer-Verlag Berlin Heidelberg.

Xiao, H., An, W., Duan, Q., & Sun, J. (2013). Dynamics of premixed hydrogen/air flame in a closed combustion vessel. *International journal of*

hydrogen energy, 38(29), 12856-12864.

Xiao, H., Duan, Q., & Sun, J. (2018). Premixed flame propagation in hydrogen explosions. *Renewable and Sustainable Energy Reviews*, 81, 1988-2001.

Xiao, H., Houim, R. W., & Oran, E. S. (2015). Formation and evolution of distorted tulip flames. *Combustion and Flame*, 162(11), 4084-4101.

Xue, L., Ning, Z., Xuanya, L., Weiqiu, H., Bing, C., & Vamegh, R. (2000). Numerical simulation of the influence of pipe length on explosion flame propagation in open-ended and close-ended pipes. *SCIENCE PROGRESS*, 103(4), 1-24.

Yao, Z., Deng, H., Dong, J., Wen, X., Zhao, W., Wang, F., Chen, G., Zhang, X., & Zhang, Q. (2020). Effect of the inclination angle on premixed flame dynamics in half-open ducts. *ACS omega*, 5(38), 24906-24915.

Zhou, L., Song, Y., Hua, J., Liu, F., Liu, Z., & Wei, H. (2022). Effects of different hole structures of pre-chamber with turbulent jet ignition on the flame propagation and lean combustion performance of a single-cylinder engine. *Fuel*, 308, 121902.

APPENCICES

APPENDICES

Appendix A

• **Calculation of LPG Average Chemical Formula**

Liquefied petroleum gas (LPG) is a composite of several hydrocarbons, including Ethane, Propane, Butane, and Pentane. The LPG utilized in this study is obtained from the Al-Qadisiya gas industry in Iraq. The volumetric chemical analysis of the LPG is provided in Appendix B and is summarized in Table A.1.

Table A.1

Items	C_2H_6	C_3H_8	C_4H_{10}	C_5H_{12}
Analysis by Quantity	0.50	55.45	41.18	2.87

Since the LPG is a mixture of many hydrocarbons an average chemical formula is needed for the chemical reaction equation. This formula is obtained as follows:

$$C_n = \sum X_i C_i \tag{A.1}$$

Where i is Component number, X_i is Mole fraction for component i , C_i is Number of carbon atoms for component i and C_n is Average number of carbon atoms in LPG.

$$X = n + \frac{m}{4} \tag{A.2}$$

$$H_m = \sum X_i H_i \tag{A.3}$$

Where H_m is Average number of hydrogen atoms in LPG, H_i is Number of hydrogen atoms for component i , C_nH_m is the average chemical formula of LPG.

Therefore, the average chemical formula of LPG is found to be $C_{3.358}H_{8.68}$ with an average molecular weight of ($MWLPG = 48.976$) which is used in this research.



Figure A.1



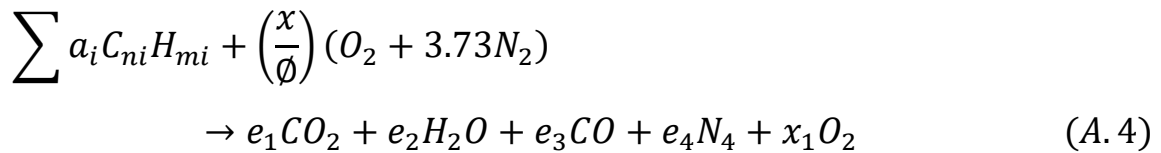
Figure A.2

- **Mixture Preparation and Combustion Equations**

Inside the combustion chamber, certain quantities of air and fuel are injected, following the appropriate equivalency ratio. This is the location where the chemical reaction takes place, and the ensuing combustion byproducts are then expelled into the exhaust system. The total number of atoms in each element remains constant throughout the combustion process; however, the atoms undergo reorganization, resulting in the formation of groups with unique chemical properties. The chemical reaction equation serves as a concise depiction of the combustion process, including the

reactants and products involved, along with their respective amounts. Both sides of the equation must demonstrate coherence, with an equivalent number of atoms for each element involved.

The oxygen necessary for combustion is usually obtained from the surrounding air, which highlights the need of accurate and consistent volumetric air measurement. When doing combustion calculations, it is conventional to assume that air is composed of 21% oxygen (O_2) and 79% nitrogen (N_2) in terms of volume. The present research includes the following combustion equations of importance:



Where ϕ is Equivalence ratio, e_1 No. of moles. of CO_2 in products, e_2 is No. of moles of H_2O in products, e_3 is No. of moles of CO in products, e_4 is No. of moles of N_2 in products, $\frac{x}{\phi}$ is No. of moles of O_2 in reactants and x_1 is No. of moles of O_2 in products.

The overall equivalence ratio for the dual fuel is calculated using the equation **Sher and Hacoen** (Sher and Hacoen, 1989):

$$\phi = \frac{(F/air)_{ac}}{(F/air)_{st}} \quad (A.5)$$

- **Stoichiometric combustion**

The ideal combustion process where fuel is burned completely is known as stoichiometric combustion where all the carbon (C) is burnt to (CO_2) and all the hydrogen (H) is burnt to (H_2O). The stoichiometric combustion for LPG gives:

$$e_1 = \sum a_i n_i \quad (A.5a)$$

$$e_2 = \frac{\sum a_i m_i}{2} \quad (A.5b)$$

$$e_3 = 0 \quad (A.5c)$$

$$e_4 = 3.76 \frac{x}{\phi} \quad (A.5d)$$

$$x = e_1 + 0.5e_2 \quad (A.5e)$$

$$x_1 = 0 \quad (A.5f)$$

- **Rich combustion**

In a situation with a rich mixture, the amount of air present is insufficient to achieve full combustion of the fuel, since it falls short of the stoichiometric requirement. This scenario indicates a deficiency of oxygen to completely oxidize the available fuel. Generally, it is often believed that the hydrogen (H_2) in the fuel undergoes a complete reaction with the oxygen that is present. Nevertheless, the residual oxygen is inadequate to fully oxidize all the carbon (C) present in the fuel into carbon dioxide (CO_2). Consequently, only a fraction of the carbon undergoes oxidation, resulting in the production of carbon monoxide (CO), in addition to carbon

dioxide.

$$e_1 = 2 \frac{x}{\phi} - \sum a_i \left(n_i + \frac{m_i}{2} \right) \quad (A.6a)$$

$$e_2 = \frac{\sum a_i m_i}{2} \quad (A.6b)$$

$$e_3 = 2 \frac{x}{\phi} - e_2 - 2e_1 \quad (A.6c)$$

$$e_4 = 3.76 \frac{x}{\phi} \quad (A.6d)$$

$$x = e_1 + 0.5e_2 \quad (A.6e)$$

$$x_1 = 0 \quad (A.6f)$$

- **Lean combustion**

A lean mixture means there is an excess of available air. This excess air passes the process without participating in combustion. However, although it does not react chemically, it affects the combustion process because it lowers temperatures due to its ability to absorb energy. **Desmond** (Desmond & Turan, 2015). The equation for the combustion of a weak mixture is:

$$e_1 = \sum a_i n_i \quad (A.7a)$$

$$e_2 = \frac{\sum a_i m_i}{2} \quad (A.7b)$$

$$e_3 = 0 \quad (A.7c)$$

$$e_4 = 3.76 \frac{x}{\phi} \quad (A.7d)$$

$$x = e_1 + 0.5e_2 \quad (A.7e)$$

$$x_1 = x \left(\frac{1}{\phi} - 1 \right) \quad (A.7f)$$

For each case of the equivalence ratio, it is needed to estimate the mole and mass analyses for both reactants and products, where the mole fraction (X) and mass fraction (Y) are as follows:

$$X = \frac{\text{No. of moles of species } (i)}{\text{Total No. of moles of mixture}} \quad (A.8)$$

$$Y = \frac{\text{No. of moles of species } (i) \times \text{molecular weight of species } (i)}{\text{total Mass of mixture}} \quad (A.9)$$

By setting the equivalent ratio, Equation A.10 is used to calculate the total number of moles of air required, as shown in Table A.2.

Table A.2

Mole of fuel	Equivalent Ratio $\phi = \frac{(F/air)_{ac}}{(F/air)_{st}}$	Stoichiometric (air/fuel) ratio	Actual (air/fuel) ratio	Total moles for reactants nT
1	0.6	15.486	9.2916	10.2916
1	0.8	15.486	12.3886	13.3886
1	1	15.486	15.486	16.486

Mole of fuel	Equivalent Ratio $\phi = \frac{(F/air)_{ac}}{(F/air)_{st}}$	Stoichiometric (air/fuel) ratio	Actual (air/fuel) ratio	Total moles for reactants nT
1	1.2	15.486	18.5832	19.5832
1	1.4	15.486	21.6804	22.6804

Knowing the mixer volume (6 L) and required total pressure and initial temperature, the actual total number of moles of reactants in the mixer is calculated using the equation of state:

$$pv = nRoT \quad (A.10)$$

Therefore, from Equation A.10, we get:

$$n = \frac{6 \times 10^5 \times 6 \times 10^{-3}}{8314.3 \times 298} \rightarrow \therefore n = 0.001453 \text{ mole}$$

The actual mole of each reactant in the mixture is calculated using the Equation A.11 and the results are shown in Table A.3.

$$(n_i)_{mixer} = \left(\frac{n_i}{n_t}\right)_{1 \text{ mole fuel}} \times n_{actual \text{ mole mixer}} \quad (A.11)$$

In the present work, the equivalent ratio is varied through the range (0.6-1.4) with an increment (0.2) for LPG fuel with air. Dalton's law of partial pressures indicates that the ratio of the partial pressures of the fuel and air is equal to their molar ratio:

$$P_i = x_i \times P_T \quad (A.12)$$

$$x_i = \frac{n_i}{n_T} \quad (A.13)$$

Where P_i is partial pressure of component, P_T is total pressure of mixer (6 bar), x_i is Mole fraction for component, n_T is total mole in the mixer (0.01453 moles) and n_i is Number of moles for component (air and LPG).

The partial pressures of LPG and air for all tests of blends with (6 bar) total mixture pressure in the mixer is shown in Table A.4.

Table A.4: The actual mole reactants of each type of fuel in the mixer

Mole of fuel	Equivalent Ratio $\phi = \frac{(F/air)_{ac}}{(F/air)_{st}}$	Actual Mole of air	n_T (1) mole of reactant	No. of total moles for mixture in mixer	No. of moles for air	No. of moles for LPG
1	0.6	9.2916	10.2916	0.000969	0.000591512	0.000013487
1	0.8	12.3886	13.3886	0.000969	0.00058714	0.00001785
1	1	15.486	16.486	0.000969	0.000582849	0.000022150
1	1.2	18.5832	19.5832	0.000969	0.000578612	0.000026387
1	1.4	21.6804	22.6804	0.000969	0.00057443	0.00003056

Table A.5: The partial pressure of reactants of each mixture in the mixer

Moles of fuel LPG 1 – K	ϕ	P_{mix} (mbar)	P_{LPG} (mbar)	P_{air} (mbar)
1	0.6	6000	130.44	5869.6
1	0.8	6000	172.67	5827.3

Moles of fuel LPG $1 - K$	ϕ	$P_{mix} (mbar)$	$P_{LPG} (mbar)$	$P_{air} (mbar)$
1	1	6000	214.3	5785.7
1	1.2	6000	255.33	5744.7
1	1.4	6000	295.79	5704.2

Appendix B

Calibration

Calibration is the process of comparing a device with unknown accuracy to a device with a known, accurate standard to eliminate any variation in the device being checked. Calibration is important to ensure the reliability and accuracy of measurements and to reduce errors.

- **Pressure gauge calibration**

The calibration operation for this device is made in performed in the University of Babylon Laboratory using a U-tube manometer for calibrating the pressure gauge in the mixing chamber, as seen in Figure B.1.

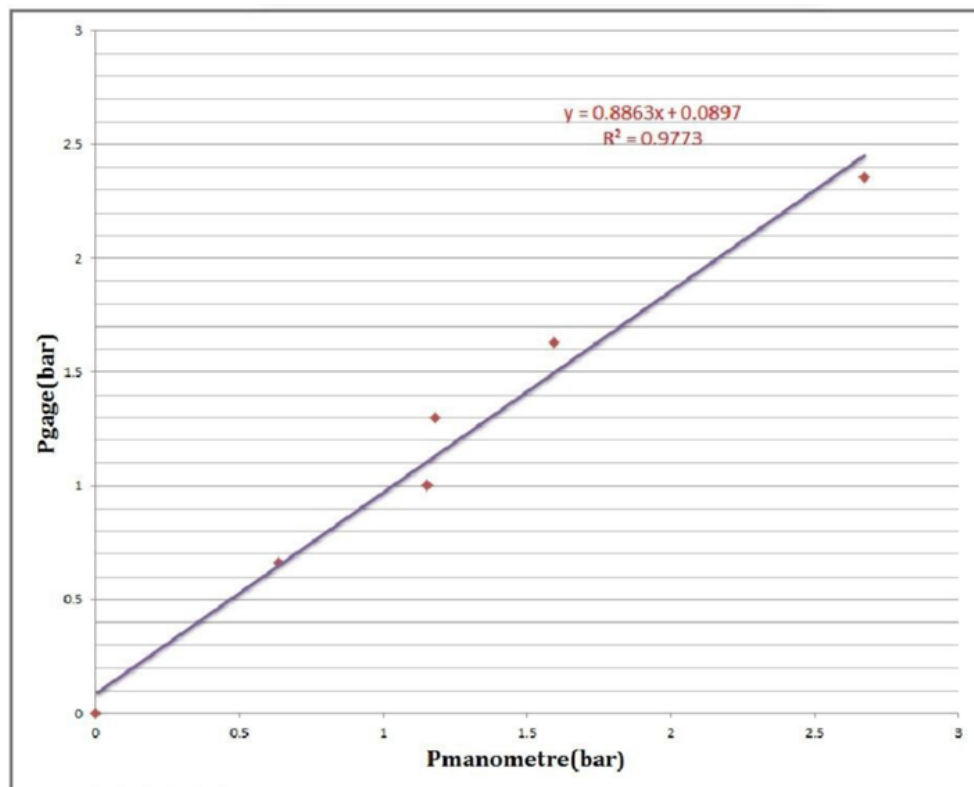




Figure B.1

• Solenoid valve



2/2 way, normally closed direct control solenoid valve

The shokouh solenoid valve are produced in 2 basic models
 1- Line solenoid valve: a normally closed one-way, directing valve. It is suitable for use as shut-off or as interrupter valve.
 2- On pump solenoid valve: this type is suitable for mounting on the oil burner pumps and can shut-off oil flow through the pumps.



Model Nc & Dc Sv

General specifications

Port size: 1/4", 1/8"
 Orifice size: 1.5 ...2.5 mm
 Pressure range: 0 to 26 bar
 Fluids: pressurized air, water, liquid fuels and steam

Technical specifications

Materials & Ratings

Body material	Brass
Seal material	vitton
Maximum fluid temp	100°C
Maximum ambient temp	55°C
Burst pressure	90 bar

Fluid type

Air & water	S
Gasoline & light fuels	F
Nutral gases	N
Steam	V

Coil materials & electrical specifications

Coil cover	polyamide
Energizing duty (ED)	100%
Enameled wire insulation class	E (120°C)
Insulation protection	IP 65

Valve code	Port size	Orifics size (mm)	Pressure range (bar)	L (min)	Appr. Weight (kg)
OL2	1/8"	1.5	0-26	1.2	0.225
OM1	1/8"	2.0	0-20	1.7	0.225
OM2	1/8"	2.5	0-16	2.6	0.225
ON1	1/4"	2.0	0-20	1.7	0.210
ON2	1/4"	2.5	0-16	2.6	0.210

22
Model NC & DC Sv **shokouh** electronic co.

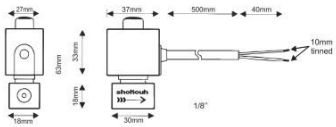
Figure B.4

Coil code	Nominal voltage (v)	Nominal power (w)	Volt-ampere (va)	Voltage tolerance
A1M	220V ac	10	14	15%
A2M	110V ac	10	13	15%
D1M	24V dc	8	8	10%
D2M	12V dc	8	8	10%

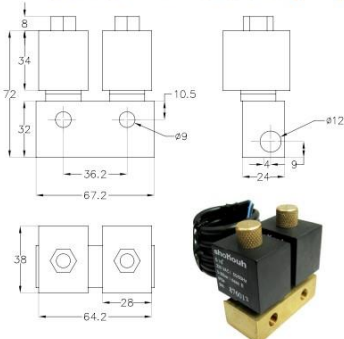
Ordering information:

Ordering code= valve code+fluid code+ coil code

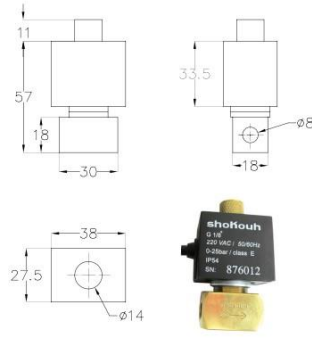
Description



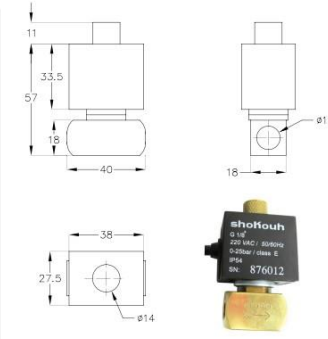
Nc & Dc Sv Dimensions (mm)



Dimension double stag Sv



Dimension Sv 1/8



Dimension solenoid valve 1/4

shokouh electronic co. Model NC & DC Sv
23

Figure B.5

- **Manuals ProAnalyst program (Version 1.5.7.0)**

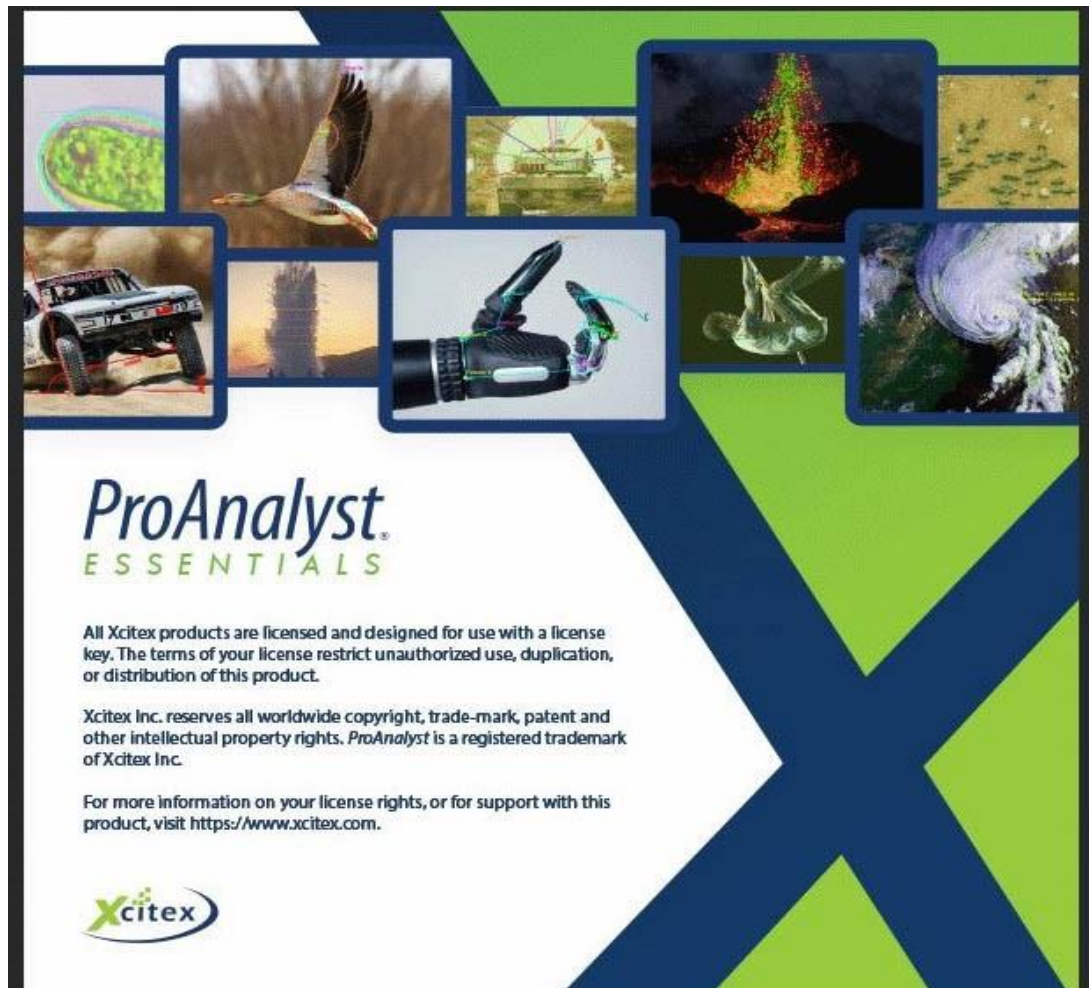


Figure B.6

Appendix C

Publications

- **Manuscript: Published**



IIETA International Information and
Engineering Technology Association
Advancing the World of Information and Engineering

International Journal of Heat and Technology
Vol. 41, No. 6, December, 2023, pp. 1521-1532
Journal homepage: <http://iieta.org/journals/ijht>

Dynamic Behaviors of Flame Propagation in Premixed Iraqi LPG-Air in a Horizontal Cylindrical Combustion Chamber

Hussein M. Almyali^{1*}, Zaid M.H. Al Dulaimi²

¹Department of Power Mechanics, Technical College Najaf, Al-Furat Al-Awsat Technical University, Najaf 31001, Iraq
²Technical Institute Al-Diwaniyah, Al-Furat Al-Awsat Technical University, Najaf 31001, Iraq

Corresponding Author Email: hussein.m.ms.etcn9@student.atu.edu.iq

Copyright: ©2023 IIETA. This article is published by IIETA and is licensed under the CC BY 4.0 license (<http://creativecommons.org/licenses/by/4.0/>).

<https://doi.org/10.18280/ijht.410614>



Received: 5 October 2023
Revised: 13 November 2023
Accepted: 5 December 2023
Available online: 31 December 2023

Keywords:
combustion behavior, flame propagation, ILPG-air, tulip flame, turbulence models

ABSTRACT

The present study focuses on the examination of the combustion behavior of Iraqi LPG-air mixtures, flame propagation, and the tulip flame phenomenon in tubes. A new experimental facility was designed and constructed, featuring a complete setup comprising a combustion chamber unit, ignition unit, fuel injection and control unit, mixture preparation unit, and flame imaging unit. The combustion process was initiated through ignition by an electric spark, and both experimental measurements and numerical simulations were conducted using various turbulence models, including the realizable k-ε model, the k-ε model, and the Launder Sharma k-ε model. The study aimed to compare and validate the numerical results with empirical observations, specifically focusing on flame propagation velocity, peak pressures, and tulip flame formation. The investigation revealed that the k-ε model exhibited the closest agreement with experimental findings, accurately capturing flame propagation dynamics and tulip flame formation. However, discrepancies were noted in the numerical simulations attributed to the absence of a

Figure C.1

- Manuscript: Accepted



Figure C.2

- **Manuscript: Accepted**

AIP Conferenc Proceedings

RESEARCH ARTICLE | MARCH 08 2024

A review: Flame front propagation in a horizontal tube of variable length

Hussein M. Adbulhusein , Zaid M. H. Al Dulaimi

[Check for updates](#)

AIP Conf. Proc. 3062, 050019 (2024)
<https://doi.org/10.1063/1.5199640>

[View Online](#) [Export Citation](#) [CrossMark](#)

08 March 2024 18:20:00

Boost Your Optics and Photonics Measurements

Lock-in Amplifier  Zurich Instruments [Find out more](#)  Boxcar Averager

AIP Publishing

Figure C.3

الخلاصة

تعتبر ديناميكيات اللهب الممزوجة مسبقًا معقدة بشكل خاص في الأشكال الهندسية المحصورة وتلعب دورًا حاسمًا في تحسين تطبيقات الاحتراق وأنظمة السلامة. الدراسة لها هدفين رئيسيين. الهدف الأول هو محاكاة نموذج التدفق المتفاعل كيميائيًا ثنائي الأبعاد (2D) المطبق في محلل XiFoam، وهو جزء من صندوق أدوات OpenFOAM CFD بطول 1.5 متر وقطر 0.72 متر. الهدف الثاني هو دراسة نفس السيناريو لتأثيرات طول الأنبوب ونسبة التكافؤ على سرعة وشكل لهب غاز البترول المسال والهواء المختلط في أنابيب أفقية مغلقة من أحد طرفي الإشعال ومفتوحة من الطرف الآخر باستخدام التصوير عالي السرعة. ومن النتائج الملحوظة أن واجهة اللهب، التي تتشكل عندما تكون نسبة التكافؤ بين 0.8-1.4 وطول الأنبوب 1.3 م، 1.5 م، و2 م، تتعرض لتشوهات كبيرة. يؤثر تكوين الخليط على تكوين وديناميكية لهب التوليب، والذي يمكن أن ينهار بشكل مختلف عند نسب التكافؤ المنخفضة والعالية. يتأثر شكل اللهب، وخاصة لهب التوليب، بطول الأنبوب ونسبة التكافؤ مع مرور الوقت. لطول 1.5 متر ونسبة تكافؤ 1، يظهر لهب التوليب عند 0.365 متر و0.0162 مللي ثانية وينهار عند 0.7 متر و0.0226 مللي ثانية. وعند نسبة تكافؤ 1.2، يتشكل لهب التوليب عند 0.372 م و0.0165 ms ويتلاشى عند 0.709 m و0.0233 ms. وبحصول نسبة تكافؤ 0.8، يتغير لهب التوليب عند 0.315 م و0.0200 ms وينهار عند 0.665 م و0.0286 ms. وبحصول على نسبة تكافؤ أعلى تبلغ 1.4، يصبح اللهب حلزونيًا عند 0.318 م و0.0221 مللي ثانية وينهار عند 0.615 م و0.0305 مللي ثانية. تُظهر كل من التجارب وعمليات المحاكاة ثنائية الأبعاد التفاعلات والتباطؤ في جبهة اللهب، والتدفق العكسي، والدوامات في الغاز المحترق مما يغير شكل اللهب ويجعل واجهة اللهب تتطور إلى شكل الخزامى. تظهر نتائج هذه المعلمات أنه مع زيادة تركيز الوقود، من خلال زيادة نسبة التكافؤ والانتقال من حالة استهلاك الوقود إلى حالة غنية بالوقود، فإن جبهة اللهب تصبح أسرع مع سرعة وضغط أعلى.



جمهورية العراق
وزارة التعليم العالي والبحث العلمي
جامعة الفرات الاوسط التقنية
كلية الهندسة

نمو جبهة الذهب في أنبوب أفقي بأطوال متغيرة

رسالة

مقدمة الى قسم هندسة تقنيات ميكانيك القوى
كجزء من متطلبات نيل درجة الماجستير في
تقنيات ميكانيك القوى – الحرارية

من قبل:

حسين محسن عبد الحسين

بإشراف:

ا.م.د. زيد معن حسن الدليمي

٢٠٢٤